University of Cagliari
Physics Department

PhD in Physics

Ab initio investigation of layered and low-symmetry oxides and interfaces: multiferroic junctions, TCO's, and a ferroelectric metal.

FIS/03

Tutor:
Prof. Vincenzo Fiorentini
Coordinator:
Prof. Paolo Ruggerone

PhD Candidate:
Francesco Ricci

XXVII Cycle - Academic year 2013/2014

Contents

Introduction

This essay is intended to be a review of the entire research work developed during my PhD school, highly based on published papers and enriched by background introductions of the debated topics. My research focused on several distinct topics sharing the use of ab-initio density functional theory calculations for studying different types of materials aimed to technological applications. In particular, it has regarded the study of the phenomena into multiferroic junctions using standard DFT approaches; the study of the correlated material $CaCu_2Ti_4O_{12}$ and the wide-gap semiconductor Ga_2O_3, by means of some beyond-DFT approaches such as the famous GW method and the pSIC method, a self-interaction correction method developed within our research group. Moreover, I have contributed to enhance the development of the pSIC code, providing it with two new tools, namely two routines for calculating the dielectric function and the X-ray absorption cross section, which aims to obtain a more direct comparison between theoretical band structure and experimental measure of optical properties.

For clarity, I will separate this report into two main and distinct parts: Part I concerns the investigation into multiferroic junctions, while Part II contains the investigations into $CaCu_2Ti_4O_{12}$ and Ga_2O_3, with particular attention on the results found by our in-house self-interaction correction approach, and its developing by means supplementary tools. In the following, I will spend some words to introduce every single topic, but I refer the reader to each introductions for more details.

The topic of multiferroic materials, discovered in the 60s years, has obtained many renewed attentions in this recent period for their possible practical application in many types of electronic devices. The key property of these materials is the coexistence of both ferromagnetic and ferroelectric phase and their mutual coupling. The first studies reveal this property in single phase materials, but the predicted and measured coupling is quite weak. With modern techniques of crystal growth, junctions between different materials become accessible, opening the way to combine ferroelectric and ferromagnetic materials into a multiferroic two-phases heterostructure. Theoretical and experimental studies have assessed phenomena such as tunnelling electro-resistance and tunnelling magneto-resistance inside these junctions, showing in particular that the tunneling of electrons is greatly affected by the orientation of both magnetic e ferroelectric phases.

In Chapter 2, we report our paper about the $SrRuO_3$/$PbTiO_3$/$SrRuO_3$ multiferroic tunnel junction (MFTJ) with asymmetric interfaces, showing first the significant presence of a residual depolarizing field; second, the dependence of tunneling through an asymmetric potential barrier by the polarization orientation and finally an assessment of the magneto-electric effect at the junction interfaces. In Chapter 3, we report a conference paper about V doping of $PbTiO_3$, an interesting way to create a single phase multiferroic material. This was part of an initial survey about doping the interfaces of $SrRuO_3$/$PbTiO_3$/$SrRuO_3$ junction with vanadium in order to enhance its properties. Then, in Chapter 4, we report a recent work on a “ferroelectric metal”, which will be published soon. The layered perovskite $Bi_5Ti_5O_{17}$ is predicted to be a ferroelectric metal because it has nonzero density of states (DOS) at the Fermi energy and a metal-like conductivity which coexist with spontaneous polarization in zero field. An investigation about the survival of the switchable depolarizing field in a finite system has been performed as well.

The second part of this report concerns the investigation into $CaCu_2Ti_4O_{12}$ (Chapter 6), with the purpose of unravelling the issue of the correct interpretation of experimental optical properties by using different theoretical approaches beyond standard DFT, such as VPSIC, GW, LDA+U and Hybrids methods. These approaches have also been used to give a theoretical support to an experimental gap characterization, developed by the research group of Prof. Fornari at the University of Parma, of a compelling TCO material, the Ga_2O_3 (Chapter 7.1). In both works, the pSIC method gives a further proof of its reliability in correct description of the band structure of correlated materials and wide-gap semiconductors. These success have been further improved by the inclusion in the pSIC code of a routine that calculate the dielectric function, making possible a direct comparison of the theoretical assessment of this property with the experimental one. In the same area of research, the two work presented in the Sections 7.2 and 7.3 are. In particular they regard with the study of In doping of Ga_2O_3 and β-$Ga_2O_3/(Ga_{1-x}In_x)_2O_3$ interfaces, exploiting only standard GGA/DFT schemes. They represent, as far as we know, the first theoretical investigations into this topic.

Finally, in Chapter 8 is presented the project of enhancing the pSIC code with a routine for computing of X-ray absorption spectra (XAS). Our intention has been that to include within the pSIC code a tool that calculate accurate XAS spectra directly comparable with the experimental ones, opening the way to an enormous research field where pSIC approach could give its own contribute to unravel the phenomena being behind the experimental XAS spectra. Though the coding of this tool is still in progress, the preliminary spectra calculated for different materials are well promising. I point out that all the spectra shown should be intended as validating proofs of the correct working of the implementation more than a new interpretation based on pSIC approach, though it could be the future target of this tool porting, especially in the case of correlated materials.

Part I.

Multiferroic junctions

1. Background

The modern technology is strongly based on magnetic and ferroelectric materials. Consumer data-storage devices, for example, already now exploit both ferromagnetic materials, where their spontaneous magnetization M is switched by an external magnetic field, and giant magneto-resistance effect. In the last decade, in order to increase the density of information, to reduce dimensions and the high writing energy, magnetic random-access memory (MRAMs) and related devices have been pursuited intensively. Also ferroelectric materials, that are featured by a spontaneous electrical polarization P reversible with an applied electric field E, are the main constituents of presently sensor and actuation devices. Another continuous effort is made towards the use of ferroelectric random-access memory (FeRAMs) as non volatile and high speed memory media with promising features and hopefully superior to semiconductor flash memories. Therefore, materials combining the properties of ferroelectrics and magnets are highly desirable. These materials are called multiferroics: electric polarization P and magnetization M coexist in the same material, also in absence of external electric or magnetic fields, and are coupled giving the possibility to change P applying a magnetic field or to change M using an electrical field. The existence of these class of materials is known already in 60s years, but only recently the study of multiferroics have a renascence. Mainly because of the great improvement in experimental techniques to grow new materials with specific properties and in thin film layers, and of the new theoretical approaches to the study of the coexistence of magnetism and ferroelectricity. The coexistence of several order parameters and their coupling show new physical phenomena, as the magneto-electric effect, and open the way to completely new devices. Applications include the ability to address magnetic memories electrically, without using currents; the creation of new types of 4-state logic devices, exploiting both up and down polarization and magnetization; and magneto-electric sensors. However, attempts to design multiferroics that combine ferromagnetism and ferroelectricity in the same phase have been proved unexpectedly difficult. Indeed, many multiferroics materials have been studied but until now none of them is really attractive for applications because they do not combine large and robust electric and magnetic polarization at room temperature and usually their coupling is not strong enough. Two-phase multilayer heterostructures of ferromagnetic and ferroelectric perovskites seems to be able to overcome the difficulties shown by the single-phase multiferroics. The most fascinating configuration is called multiferroic tunnel junction (MFTJ), coming from other two largely investigated junctions: magnetic tunnel junction (MTJ) and ferroelectric tunnel junction (FTJ). In MFTJ two ferromagnetic electrodes are separated by a ferroelectric insulating barrier. It is shown that the resistance of tunneling current passing through the junction depends on the relative orientation of magnetization of the two electrodes (tunnel magneto-resistance effect) and the direction of ferroelectric polarization of the insulating layer (tunnel electroresistance effect). This allows to have 4 level of resistance switchable by applying an external electric and an magnetic fields.

1.1. Ferroelectric materials

1.1.1. Landau theory

Ferroelectricity was discovered by Valasek in 1921, in the Rochelle salt [1].

The term ferroelectric (FE) is used in analogy to ferromagnetism: as ferromagnetic materials exhibits a permanent magnetic moment, ferroelectric materials have a spontaneous electric polarization. Further, as for ferromagnetism, it is possible to employ the Landau's symmetry-based treatment of phase transitions to describe ferroelectrics, as Devonshire first made [2].

Considering a bulk system with spatially uniform polarization, the thermodynamic of a ferroelectric system in equilibrium can be described by the temperature (T), the polarization (P), the electric field (E), the strain (η), and the stress (σ). In particular, in the vicinity of a phase transition we can expand approximately the free energy in powers of the dependent variables with coefficients that came from experiment or from microscopic calculations. To be more specific, we can put in zero the origin of energy for the free unpolarized, unstrained uni-axial ferroelectric crystal, and write:

$$\mathcal{F}_P = \frac{1}{2}a_0(T - T_0)P^2 + \frac{1}{4}bP^4 + \frac{1}{6}cP^6 - EP$$

where T_0 is the Curie temperature, b and c are other coefficients independent from temperature, and a_0 and c are both positive in all known ferroelectrics [3, 4].

As shown in Figure 1.1 (top (a)), from the free energy as a function of polarization we recognize two phase depending on the temperature: paraelectric for $T \gg T_0$ and ferroelectric for $T \ll T_0$. The behavior of the free energy between these two configurations is determined by the sign of the coefficient b. Indeed its sign will regulates the nature of the parelectric-ferroelectric transition, and whether the polarization at $T < T_0$ develops continuously or discontinuously.

For $b > 0$, at $T = T_0$ a second-order transition occurs, and the free energy will transform continuously from a parabolic to a double-well shape, from having only one minimum at $P = 0$ to two minima $P = \pm P_0$. Setting a null external field $E = 0$, we can estimate the spontaneous polarization P_0 as :

$$P_0 = \left\{ \frac{a_0}{b}(T_0 - T) \right\}^{\frac{1}{2}}$$

that decreases continuously with an increasing temperature, until critical point T_0.

For $b < 0$, when $T < T_0$ the free energy will have two minima in $P \neq 0$. As the temperature is increased over T_0, a new minimum in $P = 0$ appears. At any temperature between T_c and T_0 the unpolarized state exists as a local minimum of the free energy. At $T = T_c$ the three minima become energetically degenerate. Increasing the temperature over T_c, the minimum at $P = 0$ is thermodynamically favoured respect to the other two at $P \neq 0$ even if they remain. The most important feature of this phase transition is that the order parameter jumps discontinuously to zero at T_c. This type of phase transition is usually called a first-order or discontinuous transition, typical in solid-liquid transitions. We note that the presence of three minima for $T = T_c$ implies that that actual state of the system depends on whether it is approaching T_c from lower or higher temperatures. In particular, it will be that only for $T_0 < T_c$ that the ferroelectric minima are thermodynamically favorable.

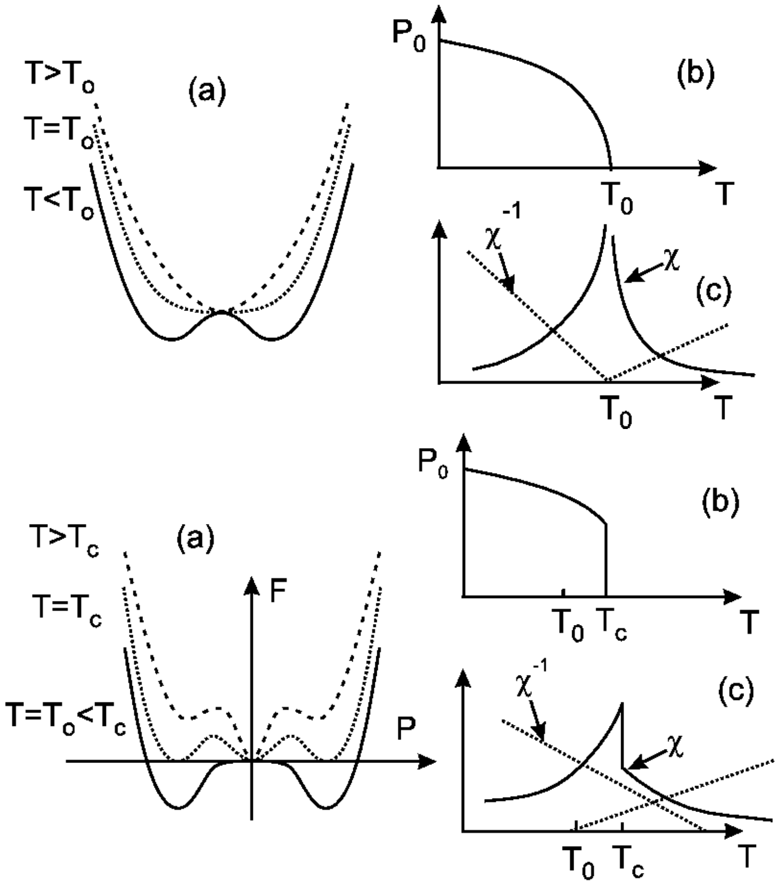

Figure 1.1.: At the top is shown the case $b > 0$. (a) Free energy as function of polarization for different temperatures; (b) polarization as function of temperature, note that it is a contious function, so we have a second-order transition; (c) permittivity, namely the first derivative of polarization respect with the temperature, as function of the latter. At the bottom same functions are shown but for the case $b < 0$, where a first-order transition occurs. Pictures from Ref. [5].

In a ferroelectric below T_0 there are (at least) two minima of the free energy, corresponding to spontaneous polarizations with different spatial orientations. Since there is a barrier between these minima, the application of a small external electric field will not immediately switch the polarization. Indeed Landau-Devonshire theory described here predicts hysteresis, shown schematically in Figure 1.2. The

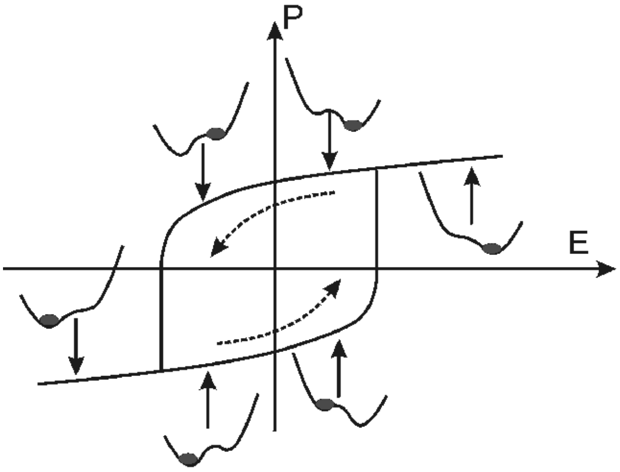

Figure 1.2.: Sketch of hysteresis loop for a ferroelectric material with additional pictures of free energy behavior in different point (P, E) of the cycle. Picture from Ref.[5].

hysteresis loop represents the polarization P as function of external electric field E. We observe that for $E = 0$, the polarization is not zero and can assume two values $P = \pm P_0$. Starting for example from a positive polarization, we need to apply an increasing electrical field to overcome the potential barrier and push the system from it current polarized state to the reversal one with a negative value of P. When this finally occurs, decreasing external field we will observe that the polarization could decrease a bit, but for $E = 0$ it will be non zero. The system lives in the other polarized state. Now, starting from this position and applying an electric field in the opposite direction respect to the previous, we manage to push the system back to the previous polarized state.

1.1.2. Atomic origin

Now, we try to understand the microscopical origin of polarization in ferroelectric materials, considering the most relevant ones: perovskites oxides with ABO_3 chemical structure. The most common and studied of them are $KNbO_3$, $BaTiO_3$, $PbTiO_3$ (and others). Above the Curie temperature they have a cubic structure like that shown in Fig. 1.3 (a), where A cations occupy the four corners of a cube, the B cations is typically a transition metal (TM) occupying the center of this

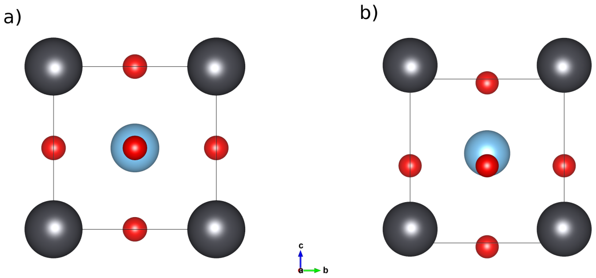

Figure 1.3.: a) Cubic and b) tetragonal phase of perovskites oxides with ABO_3 structure, corrisponding to paraelectric and ferroelectric phase respectively. Cations A are in gray, cation B is in cyan and oxigens are in red.

cube and of the octahedral cage of oxygen ions. When the temperature is lowered they leave their high symmetry paraelectric structure, where roughly behaves as ordinary dielectrics, and display a series of structural transitions to low-symmetry ferroelectric phases. Typically, the first transition is to a tetragonal phase (Fig. 1.3 (b)), characterized by microscopic displacements of the ions from the high-symmetry sites. The distortion determines a preferred polarity of the tetragonal axis and is responsible for the occurrence of spontaneous polarization.

We will follow the [6] to explain the origin of the ferroelectric phase at low temperature.

In fact, ionic-bond perovskite oxides are always centrosymmetric (therefore, not ferroelectric-favoured). This is because, for centrosymmetric structures, the short-range Coulomb repulsions between electron clouds on adjacent ions are minimized. The ferroelectric stability is therefore determined by a balance between these short-range repulsions favouring the non-ferroelectric centrosymmetric structure, and additional bonding considerations which stabilize the ferroelectric phase. Currently, two distinctly different chemical mechanisms for stabilizing the distorted structures in ferroelectric oxides have been proposed in the literature, both described as a second-order Jahn–Teller effect. Here, we mention the ligand-field hybridization of a TM cation with its surrounding anions. Considering $BaTiO_3$ as an example, the empty d-states of TM ions, such as Ti^{4+} in $BaTiO_3$, can be used to establish strong covalency with the surrounding oxygen anions which soften the Ti–O repulsion [7, 8]. It is favourable to shift the TM ions from the centre of O_6

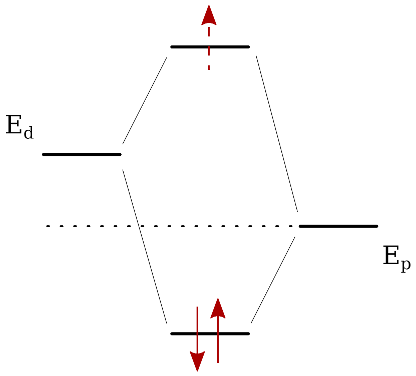

Figure 1.4.: Energy levels of the orbital configuration of O-TM-O chain unit in ABO_3 perovskite.

octahedra towards one (or three) oxygen(s) to form a strong covalent bond at the expense of weakening the bonds with other oxygen ions, as shown in Fig. 1.3 (b). The hybridization matrix element t_{pd} (defined as the overlap between the wave functions of electrons in Ti and O ions) changes to $t_{pd}(1+gu)$, where u is the distortion and g is the coupling constant. In the linear approximation, corresponding terms in the energy $\sim (-t_{pd}^2/\Delta)$, where Δ is the charge transfer gap, cancel each other [7]. However, the second-order approximation produces an additional energy difference:

$$\delta E \cong -(t_{pd}(1+gu))^2/\Delta - (t_{pd}(1-gu))^2/\Delta + 2t_{pd}^2/\Delta = 2t_{pd}^2(gu)^2/\Delta.$$

If the corresponding total energy gain $\sim u^2$ exceeds the energy loss due to the ordinary elastic energy $\sim Bu^2/2$ of the lattice distortion, such a distortion would be energetically favourable and the system would become ferroelectric. Referring to Fig. 1.4, one observes that only the bonding bands would be occupied (solid arrows) if the TM ion has an empty d-shell, a process that only allows for electronic energy. If there is an additional d-electron on the corresponding d-orbital (dashed arrow), this electron will occupy an antibonding hybridized state, thus suppressing the total energy gain. This seems to be one of the factors suppressing the tendency of magnetic ions to make a distorted shift associated with ferroelectricity [7, 8].

In addition to the ligand-field hybridization of a B-site (TM) cation by its surrounding anions, which is responsible for the ferroelectric order, the existence of

$(ns)^2$ (lone-pair) ions may also favour breaking the inversion symmetry, thus inducing and stabilizing the ferroelectric order. In general, those ions with two valence electrons can participate in chemical bonds using (sp)-hybridized states such as sp^2 or sp^3. Nevertheless, this tendency may not be always true and, for some materials, these two electrons may not eventually participate in such bonding. They are called the 'lone-pair' electrons. The ions Bi^{3+} and Pb^{2+} have two valence electrons in an s-orbit, which belong to the lone pairs. The lone-pair state is unstable and will invoke a mixing between the $(ns)^2$ ground state and a low-lying $(ns)^1(np)^1$ excited state, which eventually leads these ions to break the inversion symmetry [9, 10]. This 'stereochemical activity of the lone pair' helps to stabilize the off-centre distortion and, in turn, the ferroelectricity. In typical ferroelectrics PbTiO3 and Na0.5Bi0.5TiO3, both the lone-pair mechanism and the ligand-field hybridization take effect simultaneously [9].

The ions with lone-pair electrons, such as Bi^{3+} and Pb^{2+}, are always locate at A-sites in an ABO_3 perovskite structure. This allows magnetic TM ions to locate at B-sites so that the incompatibility for TM ions to induce both magnetism and ferroelectricity is partially avoided. The typical examples are $BiFeO_3$ and $BiMnO_3$, where the B-site ions contribute to the magnetism and the A-site ions via the lone-pair mechanism lead to the ferroelectricity. There has been until now an intense investigation of $BiFeO_3$ and $BiMnO_3$ all over the world, which focuses on the enhanced ferromagnetism and ferroelectricity. The strong magneto-electric coupling in the macroscopic sense, such as the mutual control of ferroelectric domains and antiferromagnetic domains, were revealed by recent experiments. Therefore, it may be beneficial to devote some effort to addressing these two materials. In both $BiFeO_3$ and $BiMnO_3$, Bi^{3+} ions with two electrons in a 6s orbit (lone pair) shift away from the centrosymmetric positions with respect to the surrounding oxygen ions, favouring the ferroelectricity. As we will see in Chapter 4 this type of distorsion of Bi ions also yields the ferroelectricity in $Bi_5Ti_5O_{17}$ perovskite.

1.1.3. Polarization assessment

Going back to macroscopical world, the question that now we ask is: how to measure the spontaneous polarization in ferroelectrics?

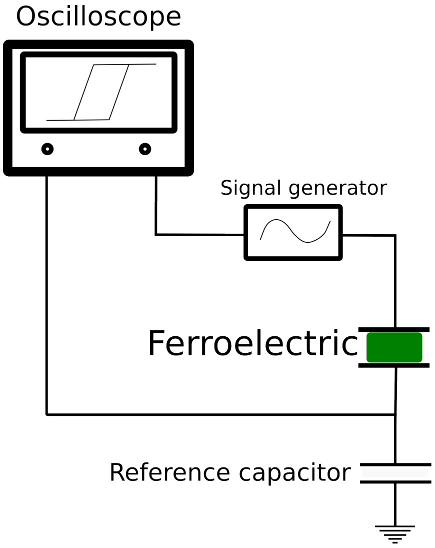

Figure 1.5.: Sketch of the usual Sawyer-Tower circuit used to measure the polarization of a ferroelectric material sample.

The experimental way is surprisingly simple: the classic Sawyer-Tower circuit, shown in Figure 1.5, accomplish this task. Since the capacitor and ferroelectric are in series, the charge must be the same. Hence, measuring the voltage variation, we obtain the charge of the ferroelectric by $Q = C \cdot V$.

From the theoretical point of view the macroscopic electric polarization is more difficult to define. Indeed, it had been a source of controversial interpretations until 90s years, when modern theory of polarization was introduced.

Microscopically, the simplest way is to consider the dipole of unit cell as a well defined quantity. Although this is possible for finite systems as molecules, it become ill-defined in bulk solids: choosing two different but equally valid cells we can obtain two opposite estimates of polarization.

Alternatively, we can consider the dipole per unit volume of a finite piece of matter

$$P = P_{ion} + P_{el} = \frac{1}{V}\left[-e\sum_{l} Z_l \mathbf{R}_l + \int d\mathbf{r}\rho(\mathbf{r})\right]$$

but, though it is well defined, it is not a bulk property depending on the shape and the truncation of the sample. If we think to what we do in experiments, when bulk tensors such that for piezoelectricity, dielectric permittivity etc., we actually derived them from a variation of P with respect to suitably chosen perturbations. Also for spontaneous polarization, the actual measured quantity is only the difference ΔP between two state of the crystal. Therefore, to assess the polarization as a bulk property from the theory, the basic quantity of interest is the difference ΔP in polarization between two different states of the same solid.

This is the first key concept in modern theory of polarization. The second important point, again taken from experiment, is that the quantity to take into account is the current insted of the charge [14]. Therefore, we have to extract the observable polarization from the phase of wavefunction rather than from the squared modulus of it. Within a finite system, the two alternate descriptions are equivalent, since the continuity equation states that the charge piling up at the surface during the continuous transformation is related to the current that flows through the bulk region. However, in an infinite crystal in the thermodynamic limit, this connection does not longer hold: the charge and the current, described by the wave function's modulus and phase respectively, then carry quite different informations. In this same limit, macroscopic polarization is a property of the current not of the charge. Therefore, in order to assess ΔP in an infinite periodic crystal, the macroscopic current flowing through the unit cell have to be measured. The Berry phase of Bloch orbitals performs exactly this task in an elegant and effective way.

The modern theory of polarization is based on works of Resta [15], who see in ΔP an integrated macroscopic current, of King-Smith and Vanderbilt [17], who identified in ΔP a geometric quantum phase [19, 20]. It is an approach very elegant and computationally powerful, as has been demonstrated in many calculations of various real materials [17, 21, 22]. We refer the reader to those reference to have a complete knowledge about this topic (see also [14] for a review).

Here we will just follow the paper of Resta [16] to get an idea of how this theory works considering a one dimensional ferroelectric model (Fig. 1.6 (top)). First, we need to define a scalar parameter λ defining the amplitude of ferroelectric distortion, that assumes two different value for centrosymetric ($\lambda = 0$) and for ferroelectric ($\lambda = 1$) structures. The potential $V_\lambda(x)$ has the period a of the lattice for any value of the parameter. Taking into account the simplest model of an insulator, we have only two electrons per cell that occupy a single band with the

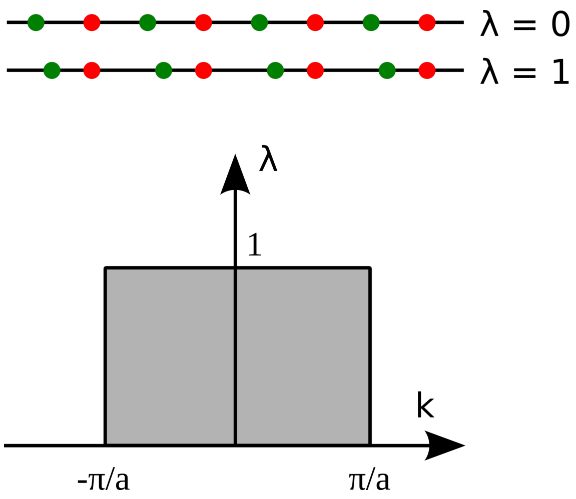

Figure 1.6.: (top) Schematic representation of a one-dimentional para- and ferroelectric material (top and bottom, respectively). (bottom) The circuit in (k, λ)-plane chosen to calculate the Berry phase.

following wavefunctions:

$$\psi_\lambda(k, x) = e^{ikx} u^k_\lambda(x)$$

where k is the Bloch vector in the one-dimensional Brillouin zone $[-\pi/a, \pi/a]$, $u^k_\lambda(x)$ is the periodic function with period a. The Hamiltonian of this system will depend on parameters k and λ. Thus, it is possible to write a two-dimensional parameter ξ having k and λ as components, and consider as integration curve C the contour of the rectangle in the (k, λ) plane, to calculate the Berry phase γ in usual formulation that we will see in the separated subsection 1.1.3. The polarization difference ΔP between the ferroelectric $(\lambda = 1)$ and the non-polar $(\lambda = 0)$ structures coincides with the integrated current which flows through the linear chain while the ions are continuously displaced. According to the modern theory, this quantity is

$$\Delta P = e\gamma/\pi + \Delta P_{ion} \tag{1.1}$$

where the first term represent the electronic contribution, where e is the electron charge, and ΔP_{ion} is the trivial contribution of the classical ions. The dimensions of polarization are dipole per unit length.

The Berry phase approach is basically a one-electron theory, such a the band theory of solids. Thus, the main results can be reformulated in any mean-field theoretical scheme, as in the most famous and common density functional theory (DFT) of Kohn and Sham. A correct many-body extention is accessible, though. Since ΔP is adiabatic observable of electronic ground state, the DFT framework is appropriate. Within it, further, ΔP is shown to be a property of the manifold of occupied Kohn-Sham orbitals, in particular it depends on the phases of these orbitals in a gauge-invariant way [14].

Nowaday, the three-dimensional analogue of Eq. 1.1 has been implemented in several DFT first-principles codes and used for an enormous number of real materials investigations. Indeed, in the case of ferroelectric polarization, thanks to modern theory of polarization, the numerical results display a quite surprising agreement with the experimental data. The very first case study was $KNbO_3$ in its tetragonal phase [15, 17]: the theory predicts a spontaneous polarization P_S of 0.35 C/m^2, compared with early measurements of about 0.37 C/m^2 [18]. Other successful theoretical predictions of polarization are those for the most studied ferroelectric material, such as $BaTiO_3$, $BiFeO_3$, $PbTiO_3$: theoretical values of 0.32, ~0.95, 0.88 C/m^2 have been found respectively [23]. Incidentally, I have performed a berry phase calculation of bulk $PbTiO_3$, in GGA-PBE approximation, finding a value of 0.86 C/m^2.

Berry phase

In this short subsection, I will reproduce the formulation of Berry phase proposed by Resta in paper [16], since I found it clear and algebraically simple but still effective to explain this very general concept.

One starts with the most generic quantum Hamiltonian having a parametric dependence:

$$H(\xi)\,|\psi(\xi)\rangle = E(\xi)\,|\psi(\xi)\rangle$$

where ξ is defined in a suitable domain: a two-dimensional ξ with real values has been chosen for illustration in the Figure 1.6 (bottom). In the original Berry paper $H(\xi)$ is the electronic Hamiltonian of a molecule in the Born-Oppenheimer approximation, and ξ is a nuclear coordinate [19]. But the theory is quite general and applies to the most disparate parametric dependence: in the theory for the macroscopic polarization of a crystalline dielectric the parameter ξ is a rather exotic one. We assume that $|\psi(\xi)\rangle$ is the ground state, non-degenerate for any ξ. The phase difference $\Delta\phi_{12}$ between the ground eigenstates at two different ξ points is defined in the most natural way as

$$e^{-i\Delta\phi_{12}} = \frac{\langle\psi(\xi_1)\,|\psi(\xi_2)\rangle}{|\langle\psi(\xi_1)\,|\psi(\xi_2)\rangle|}$$

$$\Delta\phi_{12} = -\mathrm{Im}\log\langle\psi(\xi_1)\,|\psi(\xi_2)\rangle$$

This phase cannot have any physical meaning. In fact, any quantum mechanical state vector is arbitrary by a constant phase factor: "choice of the gauge" will be used in the following as a synonym for the (arbitrary) choice of such a phase. For instance, in numerical implementations the gauge is typically chosen by the diagonalisation routine. A simple change of gauge at ξ_1 and/or at ξ_2 will give the phase difference the most arbitrary value. Despite this, when one considers the total phase difference γ along the closed path in the Figure 1.7:

$$\begin{aligned}\gamma &= \Delta\phi_{12} + \Delta\phi_{23} + \Delta\phi_{34} + \Delta\phi_{41}\\ &= -\mathrm{Im}\log\langle\psi(\xi_1)\,|\psi(\xi_2)\rangle\langle\psi(\xi_2)\,|\psi(\xi_3)\rangle\langle\psi(\xi_3)\,|\psi(\xi_4)\rangle\langle\psi(\xi_4)\,|\psi(\xi_1)\rangle\end{aligned}$$

one immediately realizes that the phase difference is gauge invariant, since all the gauge-arbitrary phases cancel in pairs. The most common Berry phase γ is defined in the continuum limit. Suppose we have a smooth closed curve C in the parameter domain, as in the Figure 1.7, and we discretize it with a set of N points, we can then assume that the gauge is chosen such that $|\psi(\xi)\rangle$ is single-valued and varies in a differentiable way along the path. The phase difference between two contiguous points is therefore given by:

$$e^{-i\Delta\phi} = \frac{\langle\psi(\xi)\,|\psi(\xi+\delta\xi)\rangle}{|\langle\psi(\xi)\,|\psi(\xi+\delta\xi)\rangle|}$$

$$-i\Delta\phi \simeq \langle\psi(\xi)\,|\psi(\xi+\delta\xi)\rangle\cdot\delta\xi$$

When the set of points becomes dense, the total phase difference γ converges to

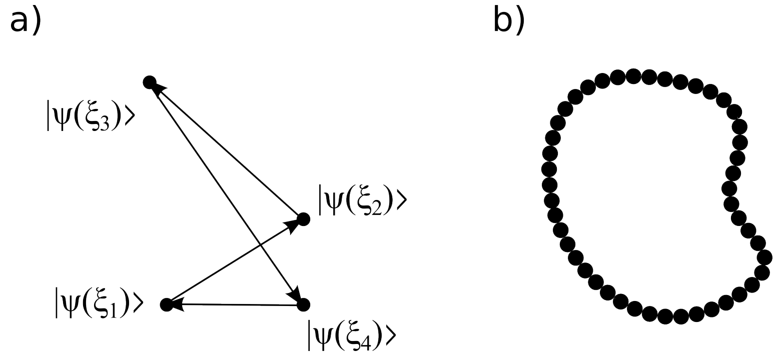

Figure 1.7.: (a) A closed circuit made of only four points representing stable states of the probed system during the ξ parameter changing. (b) Continuos closed path made of infinite little changes of the ξ parameter over which Berry phase is calculated.

the circuit integral of a real linear differential form, called the Berry connection:

$$\gamma = \sum_{s=1}^{N} \Delta\phi_{S,S+1} \to i \oint_C \langle\psi(\xi)\ |\psi(\xi + \delta\xi)\rangle \cdot \delta\xi$$

The above simple-minded algebra leads to a result of overwhelming physical importance, namely that a gauge-invariant quantity is potentially a physical observable. Traditionally, we are accustomed to regarding any observable effect in quantum mechanics as the eigenvalue of some operator. The main message of Berry's milestone paper can be spelled out by saying that there are also observable effects of a completely different nature: the phase γ cannot be expressed in terms of the eigenvalues of any operator, whereas it is by definition a gauge-invariant phase of the state vector. Several observables having the nature of a Berry phase have been found in different ares of physics: the macroscopic polarization of a crystalline dielectric is one of them, very recently discovered, but not the least by far. Having understood that the Berry phase in general may provide a qualitatively novel quantum observable, one naturally wonders how and why this happens. To answer, one must re-examine the initial assumption of a parametric Hamiltonian, and realize its most fundamental meaning. In general, a quantum system having a parametric dependence in its Hamiltonian cannot be isolated: the parameter schematizes a kind of coupling with other variables not described by the given quantum Hamiltonian, or more generally with “the rest of the universe”, to use Berry’s words. The parametric Hamiltonian allows one to deal with a part of a larger system as if it were isolated: as a trade-off, some observable effects may occur as gauge-invariant phases.

1.2. Depolarizing field problem

If we suppose to terminate the crystal by two interface perpendicular to the polarization, we expect a buildup of free opposite charge at the surfaces, generating a macroscopic dipole, that in bulk would be screened by the opposite sign charge density of adjacent periodic cells. These unscreened surface charges generate a field that counteracts to the ferroelectric distortion and making energetically difficult for the sample to sustain the ferroelectric state. Since the magnitude of this depolarizing field depends on the thickness of the slab considered, its influence increases with reduced size and it is important to take into account of it for a correct description of small ferroelectric systems. Thus, the problem of a critical thickness is crucial to exploit ferroelectric materials as thin films in microelectronic devices, as capacitors for example.

The presence of this field inside the ferroelectric material has been observed experimentally and theoretically predicted and calculated (see references inside [103]). In the paper of Junquera and Ghosez [103], a supercell of $BaTiO_3$ slab between two metallic electrodes of $SrRuO_3$ representing a capacitor, was studied. In particular the relation between the total energy of the cell and the ferroelectric distortion parameter was calculated for different thicknesses of ferroelectric thin film. They found that the limit for a stable ferroelectric phase is 6 basic unit of $BaTiO_3$ as clearly shown in Figure 1.8.

They further observe that near the interface $BaTiO_3/SrRuO_3$ there is a complex rearrangement of charge, but the screening effect of metal is not perfect. This means that an unscreened charge remains at the interfaces. The proof come from the electrostatic potential: inside the metal it is zero, but near the interfaces it drops causing an almost linear behaviour inside the ferroelectric, namely an electrostatic field, opposite to polarization, is still present inside it. The magnitude of this depolarizing field depends first on the screening length of the metal and

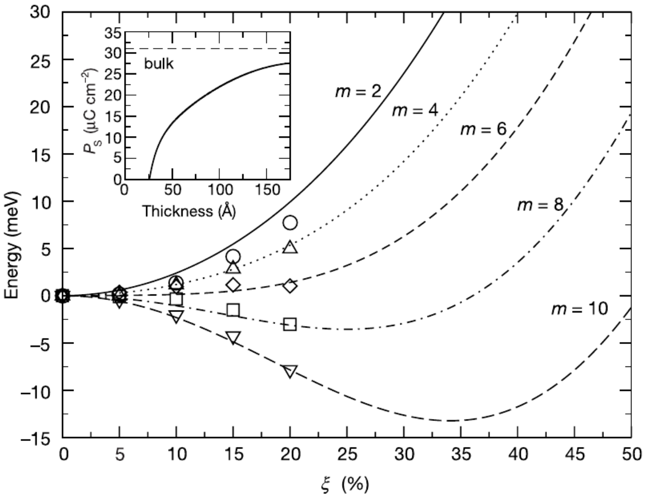

Figure 1.8.: Free energy versus distorsion paramter $\xi(\%)$ of the $BaTiO_3$ in the $BaTiO_3/SrRuO_3$ supercell for different number of layers. Stability of spontaneous polarization is found only beyond a thickness of 6 layers. In the inset, the polarization increasing respect with the thickness of ferroelectric until it reaches the bulk maximum value for quite thick sample. Figure from Ref. [103].

the polarization of the thin film which determine the potential drop and second on the film thickness: $\Delta V = 2\mathbf{E}/l$.

Energy of film in presence of this field is $E = U - \mathbf{P} \cdot \mathbf{E}$, where U is the internal energy under zero field, and $\mathbf{P} \cdot \mathbf{E}$ is the depolarizing field contribution to total energy. U is approximated from the bulk soft-mode double-well energy. Contribution from atomic displacements and from the electronic polarization are taken into account to calculate polarization P. The depolarizing field E_d is deduced from the slope of electrostatic potential inside the ferroelectric.

In this model they assume that the modification of the bonding at the interface plays only a minor role, thus the dominant effect is electrostatic one. Thus, under this assumption, in the case of zero internal field, for example in perfect screening scenario, total energy E is equal to U and the ferroelectric has the same behavior as in the bulk. But in the real case of metal interface, the screening is not perfect and a sizable depolarizing fields appears.

The main effects of this field are, first, the suppression of ferroelectricity at

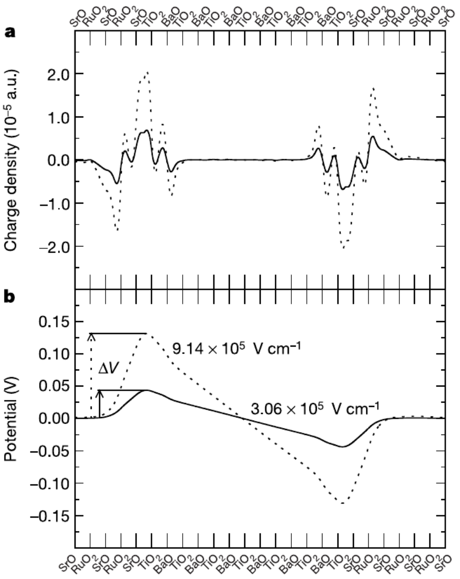

Figure 1.9.: Figure from Ref. [103]. (a) Total charge density of $m = 6$ thickness, and (b) electrostatic potential for two level of distorsion of $BaTiO_3/SrRuO_3$ supercell. The value of residual electric fields are shown.

finite size, and second, the reduction of the spontaneous polarization also well above the critical thickness, indeed the bulk polarization is achieved slowly for film of increasing size.

Moreover, the depolarizing field has been shown to be the principal cause of the reduced capacitance value in high-permittivity insulators capacitors by Stengel and Spaldin in [24]. They performed an ab-initio study of a capacitor with metal electrodes of $SrRuO_3$ and a high-permittivity dielectric $SrTiO_3$, which they applied an external electric field on. They showed that the calculated permittivity achieves the classical value only in a narrow part of the dielectric and decreases much around the interfaces. They calculated also the induced potential in both cases of fixed atoms in the zero field positions, relaxing only the electrons under a voltage bias, and of relaxed atomic positions. In the first case the uniform electric field inside the dielectric slab was equal to classical value $E = \Delta V/l$. In the second case, the field in the dielectric was drastically reduced. The difference of the two potentials is the component of the potential that steam from the relaxation of ions. It basically

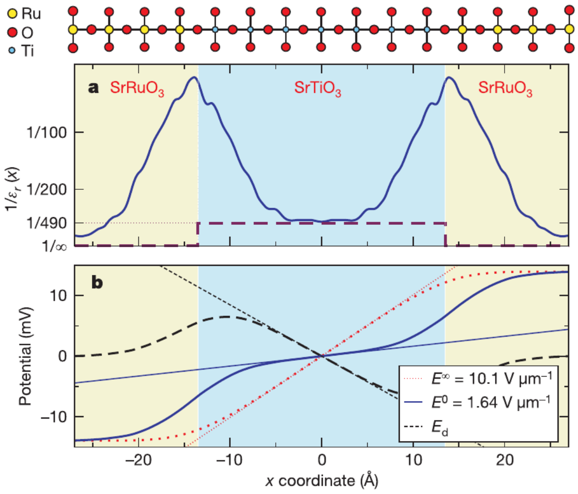

Figure 1.10.: Figure from Ref. [24]. (a) Theoretical and calculated values of permittivity and (b) electrostatic potential due to only electrons (red curve) and additional ions relaxation (blue curve). The difference of previous potentials leads to the depolarizing field, in the $SrRuO_3/SrTiO_3/SrRuO_3$ model of capacitor.

induces a polarization of the layers near the interface and an electrical field that counteracts to relaxation and reduces the total electrical field inside the insulating slab because of its opposite sign respect to that of external field. This is the same depolarizing field seen before.

Until now we have shown that the depolarizing field has a detrimental effect in the real capacitors, with both normal or ferroelectric dielectric insulator film, reducing their capacitance value. In the next section we are going to see that the residual field inside the ferroelectric slab of a capacitor is the key concept in another type of device: the ferroelectric tunnel junctions (FTJ).

1.3. Giant electroresistance in FTJ

Ferroelectric tunnel junctions (FTJs) are devices that enjoy a tunneling current between two metallic electrodes through a thin ferroelectric insulator. The main feature of this device is that this tunnelling current or the resistance is strongly influenced by switching the polarization orientation of the ferroelectric barrier.

This phenomenon is known as tunneling electro-resistance (TER) effect.

One of the physical mechanism behind the TER effect in ferroelectric tunnel junction is the change of the electrostatic potential profile induced by the reversal of electric polarization in ferroelectric. As we have said before, a polarization surviving also in thin ferroelectric films, generates surface charges only partially screened by the metal electrodes and hence a depolarizing field remain inside the ferroelectric. If the two interfaces are identical, the reversal of polarization yields two symmetrically identical potential profiles, that does not change the tunnelling resistance. Whereas, imagining to have two different interface M_1-FE-M_2, for example using two different metals, the two potential profiles would be different for opposite polarization directions. Thus, in this last case the tunneling electrons will across a different potential and TER effect will appear.

I will show in the following the simple but effective electrostatic model presented by Zhuravlev et al in Ref. [31], to investigate the TER effect and assess it in a ferroelectric tunnel junction made by different metals (M_1-FE-M_2).

In their model, they consider a ferroelectric thin film of thickness d placed between two different semi-infinite metal electrodes. The ferroelectric is assumed to be uniformly polarized in the direction perpendicular to the interfacial plane. The polarization $\mathbf{P}$ creates the surface charge densities $\pm\sigma_P = \pm|\mathbf{P}|$ on the two surfaces of the ferroelectric film. These polarization charges, $\pm\sigma_P$, are screened by the screening charge per unit area, $\pm\sigma_S$, which is induced in the two metal electrodes, as is shown schematically in Fig. 1.11(a).

It is assumed that the ferroelectric is perfectly insulating so that all the compensating (screening) charge resides in the electrodes. Further, it is assumed that the FTJ is short circuited, equalizing the electrostatic potentials of the two electrodes at infinity. In order to find the distribution of the screening charge and the potential profile across the junction, they apply the usual Thomas-Fermi model of screening (as in Ref. [65]). According to this model the screening potential within metal 1 ($z \leq 0$) and metal 2 ($z \geq d$) electrodes is given by

$$\varphi(z) = \begin{cases} \frac{\sigma_S \delta_1 e^{-|z|/\delta_1}}{\epsilon_0} & z \leq 0 \\ -\frac{\sigma_S \delta_2 e^{-|z-d|/\delta_2}}{\epsilon_0} & z \geq d \end{cases} \tag{1.2}$$

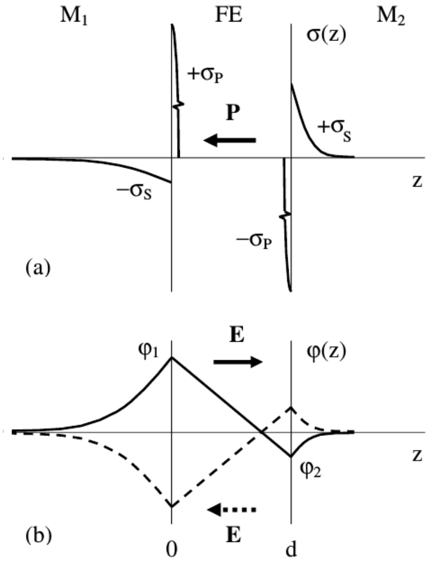

Figure 1.11.: Figure from Ref. [31]. (a) Charge density and (b) electrostatic potential for the ME_1-FE-ME_2 model. Note the different charge distribution inside the two different metals and the relative different potetial heights.

Where δ_1 and δ_2 are the Thomas-Fermi screening lengths in the M_1 and M_2 electrodes and σ_S is the magnitude of the screening charge per unit area which is to be the same in metals 1 and 2 due to the charge conservation condition. The screening charge σ_S can be found from the continuity of the electrostatic potential, implying that the potential drop within the ferroelectric film is determined by a constant electric field in the ferroelectric:

$$\varphi(0) - \varphi(d) = \frac{d(P - \sigma_S)}{\epsilon_F}. \tag{1.3}$$

To be noted that here P is considered to be the absolute value of the spontaneous polarization, and the introduction of the dielectric permittivity ϵ_F is required to account for the induced component of polarization resulting from the presence of an electric field in the ferroelectric. Now using Eqs. 1.2 and 1.3 and introducing the dielectric constant $\epsilon = \epsilon_F/\epsilon_0$ it possible to write:

$$\sigma_S = \frac{dP}{\epsilon(\delta_1 + \delta_2) + d}. \tag{1.4}$$

It is evident from Eq. 1.4 that for "good" metals in which the screening length is small (a fraction of an Angstrom) and for not too thin ferroelectrics, such that $\epsilon(\delta_1+\delta_2)/d \ll 1$, a full screening occurs, i.e., $\sigma_S = P$, which implies no depolarizing field $\mathbf{E}$ in the ferroelectric. In the opposite limit, $\epsilon(\delta_1+\delta_2)/d \gg 1$, the screening charge tends to zero and the depolarizing field increases to saturation at $\mathbf{E} = -\mathbf{P}/\epsilon$. Figure 1.11(b) shows the electrostatic potential in a M_1-FE-M_2 junction assuming that metals M_1 and M_2 have different screening lengths, such that $\delta_1 > \delta_2$. It follows from Eq. 1.2 that different screening lengths result in different absolute values of the electrostatic potential at the interfaces, so that $\varphi(0) \neq \varphi(d)$, which makes the potential profile highly asymmetric, as it is seen from Fig. 1.11(b). The switching of the polarization in the ferroelectric layer leads to the change in the potential which transforms to the one shown in Fig. 1.11(b) by the dashed line. Thus, due to different screening lengths in the two metals that make the electrostatic potential profile asymmetric, the switching of the polarization orientation in the ferroelectric barrier should inevitably lead to the change in the resistance of the junction. In order to predict the magnitude of the resistance change associated with polarization switching, the thickness of the ferroelectric barrier is assumed to be so small that the dominant transport mechanism across the FTJ is the direct quantum-mechanical electron tunneling. The overall potential profile $V(z)$ seen by transport electrons is a superposition of the electrostatic potential shown in Fig. 1.11(b), the electronic potential which determines the bottom of the bands in the two electrodes with respect to the Fermi energy E_F, and the potential barrier created by the ferroelectric insulator. For simplicity, the barrier potential is assumed to have a rectangular shape of height U with respect to the E_F. The electronic potential within the metal electrodes is determined by the screening lengths δ_1 and δ_2 which are related to the Fermi wave vectors $k_{1,2}$ according to the Thomas-Fermi theory, by $k_{1,2} = \frac{\pi a_0}{4\delta_{1,2}^2}$ where a_0 is the Bohr radius.

The resulting potential $V(z)$ for the two opposite orientations of polarization in the ferroelectric barrier is shown schematically in Fig. 1.12 for $\delta_1 > \delta_2$.

The difference $\varphi(0) \neq \varphi(d)$ controls the asymmetry in the potential profile which is decisive for the resistance change on polarization switching. Indeed, the average potential barrier height seen by transport electrons traveling across the ferroelectric layer for polarization pointing to the left, $U_L = U + (\varphi(0) - \varphi(d))/2$,

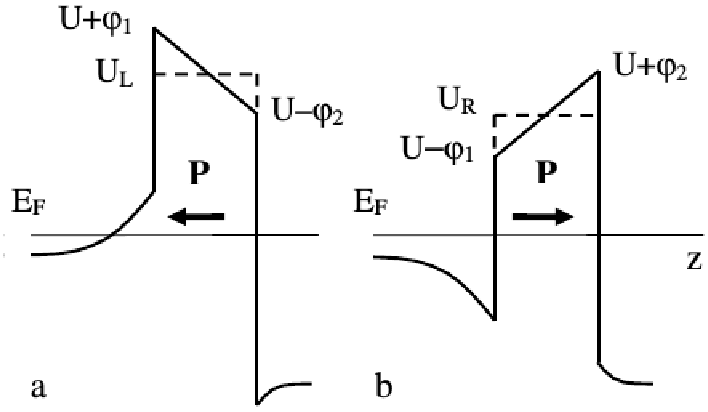

Figure 1.12.: Potential barrier seen by the electrons accordingly with the polarization direction. Note that for (a) case the highest value is lower than the highest in the (b) case, namely the mean values are in this relation $U_L > U_R$. Figure from Ref. [31].

is not equal to the average potential barrier height for polarization pointing to the right, $U_L = U + (\varphi(d) - \varphi(0))/2$, as is seen from Figs. 1.12(a) and 1.12(b). In addition, polarization switching leads to the change in the effective thickness of the tunneling barrier which is evident from Figs. 1.12(a) and 1.12(b). This occurs if the electrostatic potential φ at the M_1-FE interface exceeds the Fermi energy in metal 1.

In order to have a quantitative description of the electronic transport through these two different potential profiles, they calculate the conductance G_L and G_R for polarization pointing to the left and for polarization pointing to the right, respectively. Considering a small applied bias voltage the conductance of a tunnel junction per area A is obtained using the standard expression [66]:

$$\frac{G}{A} = \frac{2e^2}{h} \int \frac{d^2 k_{||}}{(2\pi)^2} T\left(E_F, \mathbf{k}_{||}\right),$$

where $T\left(E_F, \mathbf{k}_{||}\right)$ is the transmission coefficient evaluated at the Fermi energy E_F for a given value of the transverse wave vector $\mathbf{k}_{||}$. The transmission coefficient is obtained from the Schrodinger equation for an electron moving in the potential $V(z)$ by imposing a boundary condition of the incoming plane wave normalized to

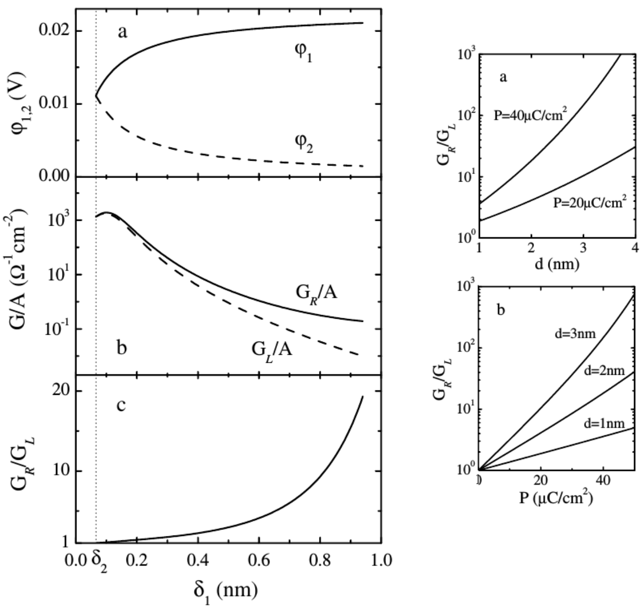

Figure 1.13.: Giant electro-resistance GER respect to metal screening parameter δ as calculated in the ME$_1$-FE-ME$_2$ model from Ref. [31]. It is shown GER ratio as function of both polarization and thickness of the ferroelectric layer.

unit flux density and by calculating the amplitude of the transmitted plane wave. Under the assumption, for simplicity, that electrons have a free electron mass in all the three layers. Using typical values for screening length for metal M$_2$ and for U and ϵ for perovskite ferroelectric, they calculate the conductances for the polarization directions and their ratio in function of δ_1, as shown in Fig. 1.13.

The two conductances start from a shared value, that of the condition of equal screening length where potential profiles are symmetric, and they decrease with the increasing of $\delta_1$that mean an increasing of potential barrier and they separated after a while because of the difference between the potential barrier U_L and U_R increase. The ratio of the conductance show an exponential growth, exceeding factor 10 as $\delta_1$approaches 1 nm.

In Fig.1.13 the relation of the conductance ratio with the thickness and the polarization of the insulating film is also shown. The ratio can be very high (10^2-10^3) and change exponentially changing both the thickness and the polarization, again because these two parameters influenced heavily the high and the shape of potential barriers in the two state of polarization. For this reason this ratio and the TER effect in ferroelectric tunnel junction are called giant electro-resistance ratio and effect (GER), respectively.

These quantitative assessment, though approximated, will be in good agreement with our findings on the junction studied and exposed in the following section 2.

1.4. Interface Magnetoelectric effect

In this section, we focus on interface magneto-electric (ME) effects caused by pure electronic mechanisms, namely of the changing the interface magnetization by applied electric field, that could be both external and “internal”. Since in every ferromagnetic (FM) interface, or surface, the time-reversal symmetry is broken by the ferromagnetism and the space-reversal symmetry by the interface itself, the ME effect always occurs. It is possible to isolate two mechanisms yielding the interface ME effect: (i) spin-dependent screening and (ii) interface bonding. From classic electrostatic, a metal film exposed to an electric field, respond with an induced surface charge $\sigma = \epsilon_0 E$ that screens the electric field according to its own screening length. If the metal is FM, the screening charge is spin dependent due to the exchange splitting of the spin bands. This induces a surface magnetization M_{surf} [26], as demonstrated by Duan et al. [27] in a ab initio calculation of Fe (001) surface exposed to an external electric field. A linear contribution to M_{surf} is determined by the surface ME susceptibility as follows [27]:

$$\mu_0 M_{surf} = \alpha_S E.$$

In SI units, α_S is measured in $Tm^2V^{-1} = s$. In a simple approximation, the screening contribution to α_S :

$$\alpha_S = \frac{\mu_B}{ec^2}\frac{n_\uparrow - n_\downarrow}{n_\uparrow + n_\downarrow}, \tag{1.5}$$

where $n_\uparrow, n_\downarrow$ are the surface spin-dependent density of states at the Fermi energy. The ME susceptibilities have been calculated from first principles for elemental FM metals Fe, Co and Ni [27]. It was found that the effect is small,

$\alpha_S \sim 10^{-22} Tm^2V^{-1}$, which is about the same order as for Cr_2O_3 but limited to the surface (i.e. $\alpha_S \sim a/a0$, where $a_0 \sim 1$ Å). Interestingly, as follows from equation 1.5, for half metals the surface ME coefficient is a universal constant $\alpha_S = \frac{\mu_B}{ec^2}$. A viable way to enhance the ME effect is that of interfacing a ferromagnet with a dielectric, since the induced surface charge scales with the dielectric constant $\sigma = \epsilon_0 \kappa E$. Thus, the ME effect increases, by two or more orders of magnitude, exploiting high-κ dielectrics, which have a dielectric constant as large as $\kappa = \epsilon/\epsilon_0 \sim 100$ and even higher. First-principles calculations, developed by Rondinelli et al. in [25], have predicted the enhanced ME susceptibility at the $SrRuO_3/SrTiO_3$ interface, i.e. $\alpha_S \sim 2 \times 10^{-20} Tm^2V^{-1}$, which is larger by two orders in magnitude than that for the FM metal surfaces [27], harnessing the large dielectric constant of $SrTiO_3$.

In particular, they investigate the response of the $SrRuO_3/SrTiO_3$ model capacitor to an applied electric field, firstly, applying an external bias of $\Delta V = 27.8$ mV across the capacitor plates, and allowing the ions to relax until their equilibrium positions. The resulting planar and macroscopically averaged change in magnetization is shown in Figure 1.14 (top). The overall induced magnetic moment is localized at the interfaces, and amounts to $2.5 \times 10^{-3} \mu_B$ per surface unit cell, corresponding to a surface spin density of $0.27 \mu C/cm^2$. The accumulation of spin is exactly equal in magnitude and opposite in sign at the left and right electrode so that the overall induced magnetic moment of the heterostructure is zero, consistent with the symmetry of the system. From the planar average of the induced spin density without macroscopic averaging (Fig. 1.14 (top)), it is clear that the dominant contribution to the induced magnetization is accumulation of spin on the interfacial RuO_2 layer. Interestingly, this effect is partially compensated by a smaller opposite induced spin density in the adjacent RuO_2 layer. Whereas, the induced spin on the $SrTiO_3$ side of the interface, which is provided by the exponentially vanishing tails of the metal-induced gap states, is small.

Secondly, they isolate the electronic response of the system repeating the electric field calculations with the ions frozen in their initial centrosymmetric positions. The magnetization charge for this case, corresponding experimentally to the high-frequency limit, is shown in Figure 1.14 (down). Since keeping the ions fixed any structural effect on magnetism is completely removed, any induced magnetization

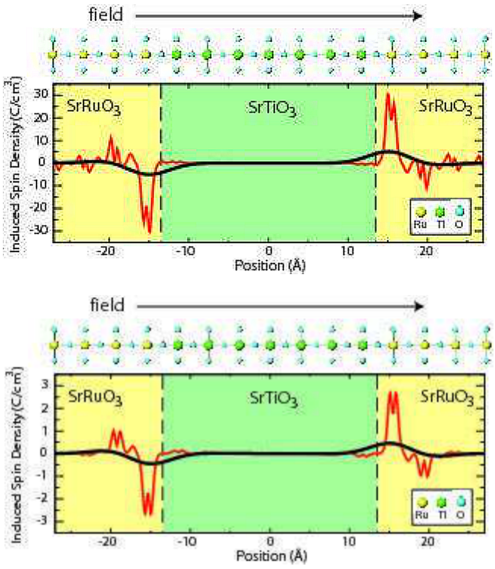

Figure 1.14.: Induced spin density as calculated in the SrRuO$_3$/SrTiO$_3$/SrRuO$_3$ capacitor by Rondinelli at al in Ref. [25]. The difference of the two pictures consist in the effect of the ion relaxation (top) that increase induced spin density of one order of magnitude. But the important aspect is shown in the bottom image: induced spin density remains, though reduced, without ions relaxation being an electronic effect.

must be of intrinsic electronic origin, and can only be ascribed to the capacitive accumulation of spin-polarized carriers at the interface. In this case they obtain an induced magnetic moment at each interface of $1.80 \times 10^{-4}\mu_B$ per unit cell, corresponding to a spin-polarized charge density of $0.019\mu C/cm^2$, hence all of these values are an order of magnitude lower than the corresponding quantities in the static-field case.

For both cases, they calculate a quantity labeled as “spin capacitance density” $C_S = \frac{\sigma_S}{V}$, where σ_S is the amount of spin polarization per unit area induced by the voltage V. This definition in an analog of the charge capacitance density per unit area, $C = \frac{\sigma}{V}$, where σ is the surface density of free charge stored at the electrode. Moreover, to avoid the dependence from the capacitor features and extract the fundamental properties of the interface response, the define the parameter $\eta = C_S/C$.

They found a similar value of η for both static-field and high-frequences cases, indicating that the mechanisms leading to the screening of polar phonons in the static regime are the same as those screening electronic bound charges in the high-frequency regime, where changes in chemical bonding and/or structure are not possible. Therefore, they conclude that this system provides the first example of a carrier-mediated magneto-electric effect, which results entirely from the capacitive accumulation of spin-polarized carriers at the interfaces. Further, they give an explanation of the origin of the carrier-mediated magneto-electric effect: on application of an external field, free carriers accumulate at the capacitor plates, which are partially screened by the dielectric polarization of the $SrTiO_3$ film. In the half-metallic limit all displaced electrons are spin-polarized in the same direction (up in the figure 1.15); in the present case there is a partial cancellation between spin-up and spin-down carriers that reflects the incomplete spin polarization at the Fermi level of the interfacial $SrRuO_3$ layer. This process accumulates up-spin magnetization adjacent to the positively charged electrode, leaving behind an absence of up-spin magnetization (or equivalently down-spin polarized holes) at the negative plate.

These electronically driven ME effects can be further enhanced by employing an FE material to produce a field effect, that we mention as “internal” in the beginning of this Section. In this case, the spin-dependent screening in a FM

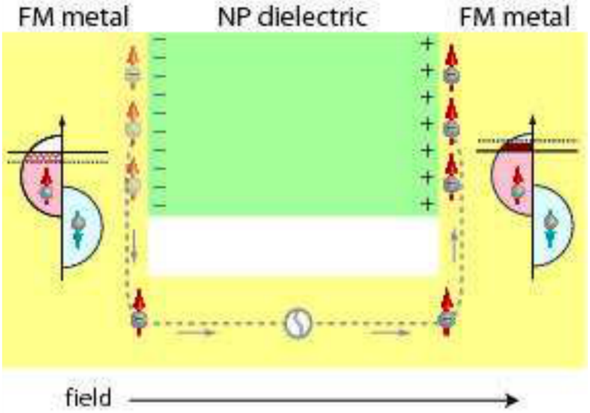

Figure 1.15.: Rondinelli at al in Ref. [25] proposed this schematic model to explain that the screening charges from a magnetic metal have a preferential spin. This gives rise the spin polarized charge density at the two surfaces metal-insulator.

material occurs in response to the polarization charge at the FE/FM interface. The latter can be changed by switching the FE polarization orientation by applied electric field. Such an ME effect was predicted for the $SrRuO_3/BaTiO_3$ interface in the work of Niranjan et al. [49]. They found from ab-initio calculations that because of the ferroelectricity in the $BaTiO_3$, the magnetizations of the $SrRuO_3$ at the left and right interfaces differ significantly. In particular, integrating the spin density over the four unit cells of $SrRuO_3$ nearest the interfaces, they assessed a total magnetic moment of $3.20\mu_B$ and $3.51\mu_B$ for the left and right interfaces, respectively. Therefore the net change in interfacial magnetic moment per unit area caused by the polarization reversal is $\Delta M = 0.31\mu_B/a^2$. Comparing the total magnetic moment of $3.55\mu_B$, of interfacial $SrRuO_3$ unit cell in the paraelectric $BaTiO_3$ state, with the ferroelectric state, they see that the change in magnetic moment induced by the polarization is $-0.35\mu_B$ for the left interface and $-0.04\mu_B$ for the right interface. This is quite different from a linear expected behavior where the changes in the moments at the two interfaces would be equal and opposite, as found in the previous $SrTiO_3$ case. Therefore, their calculations clearly show the highly nonlinear dependence of the ME coupling respect to the magnitude of the ferroelectric polarization.

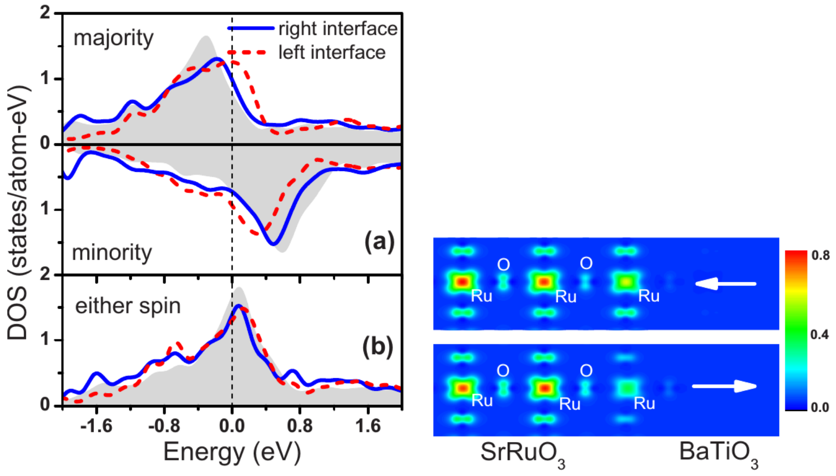

Figure 1.16.: Figures from Ref. [49]. (left) Different spin-dependent local density of states projected onto the Ru 3d orbitals at the two interfaces of $SrRuO_3/BaTiO_3$ supercell (color lines) respect with those in the middle of $BaTiO_3$ (gray): different spin states are accessible depending on the interfaces, or equivalently on the polarization direction. (right) Spin density in the (100) plane cutting through the Ru atoms.

In Figure 1.16 (left) the change in spin density at the $SrRuO_3/BaTiO_3$ [001] interface with polarization reversal is shown. It is clear that the largest change occurs within the interfacial RuO_2 mono-layer. Unlike the case that we will mention next, where the interface ME effect is largely determined by the interface bonding, there are no strong bonding effects dominating the ME coupling at the $SrRuO_3/BaTiO_3$ [001] interface. In Figure 1.16 (right) the spin-polarized densities of states projected onto the Ru 3d orbitals at the right and left interfaces are shown. It is seen that there is a clear change in the exchange splitting between the two interfaces giving rise to a change in the relative population of the two spin channels and therefore to the change in magnetic moment. The origin of the change in exchange splitting is the screening of the bound polarization charges of the ferroelectric at the interface, which they demonstrate using the Stoner model of ferromagnetism. Finally, though the relationship 1.5 between ΔM and E is nonlinear, since the ferroelectric polarization is a nonlinear function of applied electric field, an order-of-magnitude assess of α_S is still accessible. Considering a coercive field $E_c = 100kV/cm$ to reverse the polarization of $BaTiO_3$ and tak-

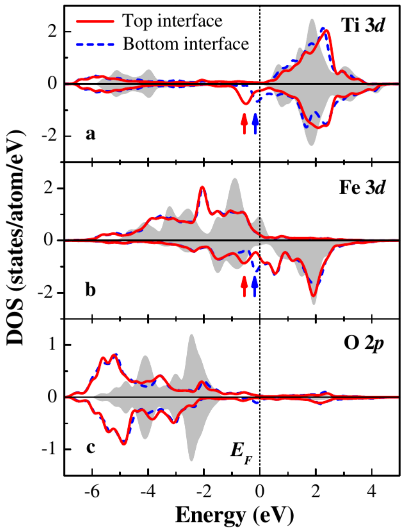

Figure 1.17.: Density of states projected onto Ti 3d, Fe 3d, O 2p orbitals at the two interfaces of Fe/BaTiO$_3$/Fe heterostructure studied in Ref. [108] . The key role is played only by interfacial Ti and Fe 3d orbitals near the fermi level that show spin-polarized states not accessible in the bulk and polarization dependent.

ing into account that $\Delta M = 0.31\mu_B/a^2$, they find the surface ME coefficient $\alpha_S \sim 2 \times 10^{-18} T m^2 V^{-1}$.

In addition to the spin-dependent screening, described in previous cases, the interface bonding mechanism may play an important role in the ME effect at the FM/FE interfaces. In the paper of Duan et al. [108], they perform an ab-initio calculation of the junction Fe/BaTiO$_3$/Fe, for increasing number of ferroelectric layers ($m \geq 4$). They observe that the magnetic moments of Fe atoms at the interfaces, equals for paraelectric BaTiO$_3$, become different in ferroelectric case and in turn interface Ti atoms show an induced magnetic moment different for the two interfaces. In this case, the presence of ferroelectricity in BaTiO$_3$ causes the magnetic moments of interface Fe and Ti atoms to deviate from their values in the paraelectric state. This is due to the change in the strength of bonding between the Fe and Ti atoms induced by ferroelectric displacements. For the electrically polarized multilayer ($m \geq 4$), the upward polarization makes Ti atoms move away from the bottom interface and towards the top interface. This causes the Fe-Ti bond length to be shorter and, hence, the overlap between the Fe 3d and Ti 3d orbitals to be stronger at the top interface compared to the bottom interface. As a result, the minority-spin bonding state lies deeper in energy and, hence, is more populated for Fe and Ti atoms at the top interface than at the bottom interface, as indicated by the arrows in Figs. 2(a) and 2(b). Thus, ferroelectric instability enhances the induced magnetic moment on top Ti atoms but reduces the magnetic moment of bottom Ti atoms. The change is opposite for Fe atoms: their magnetic moments are enhanced at the bottom interface but reduced at the top interface.

They have measured a change of the interface magnetic moments $\Delta\mu_{Fe} = 0.22, \Delta\mu_{Ti} = 0.25$ for Fe and Ti respectively, in $m = 16$ case. Considering again this difference for the two interfaces as the change in the same interface when the electric polarization is switched, it is possible to estimated the surface ME coefficient, $a_S \sim 2 \times 10^{-18} Tm^2V^{-1}$, that is four orders of magnitude higher than that for the Fe/vacuum interface [27]. Similar effects were predicted for Fe_3O_4/$BaTiO_3$ [28] and Co_2MnSi/$BaTiO_3$ [29] interfaces.

1.5. MTJ and MFTJ

The phenomenon of electron tunneling has been known since the advent of quantum mechanics and reflects the wave nature of electrons. It consist in the ability of electrons to traverse a potential barrier that exceeds their kinetic energy. Tunnel junctions exploiting this quantum-mechanical effect are made of two metal electrodes separated by a very thin insulating (e.g., Al_2O_3 or MgO) or a vacuum barrier. Among the numerous useful electronic devices based on this phenomenon, we mention:

- the Josephson junction, where tunneling occurs between two superconductors separated by a thin insulating layer, that has found important practical applications in superconducting quantum interference devices (SQUIDs), integrated circuits, and particle detectors.[33]
- scanning tunneling microscopy (STM), the conventional tool for studying the arrangement of individual atoms and molecules on surfaces.[34]

The advent of the so called “spintronic” has triggered an increasing interest in electron tunneling, especially within heterostructures composed of magnetic and non-magnetic materials, to exploit the electron spin in data storage and processing [36, 37].

By using ferromagnetic metal electrodes separated by a thin insulating barrier leads to the idea of a magnetic tunnel junction (MTJ) [39], as seen in Figure 1.18, where a spin-dependent electron tunneling occurs. Basically, it happens because the number of electrons parallel and antiparallel to the magnetization of a ferromagnet has an imbalance that causes a measurable difference in the tunneling current carried by majority- and minority-spin electrons [38].

Therefore, we can drive the tunneling current in the MTJ by an applied magnetic field that change the relative orientation of the magnetizations of the two ferromagnetic layers [40, 41]. This phenomenon is known as tunneling magnetoresistance (TMR) [42]. The key quantity is the TMR ratio, namely the relative change in resistance of a MTJ between parallel and antiparallel magnetization orientation. From the experimental side, the observation confirm a large and reproducible TMR at room temperature [40]. This opens the the door to potential application in spin-electronic devices such as magnetic field sensors and magnetic random access memories (MRAMs), where an enormous effort of research has been doing. In particular has been tried to enhance TMR and reduce MTJ resistance by improving and tuning the properties of the ferromagnetic electrodes and the insulating barrier. The Ref. [43] report a large TMR ratios up to 70%, close to the limit reported in Ref [44] of the intrinsic spin polarization of 40–50% for 3d ferromagnetic electrodes interfaced with amorphous Al_2O_3 barriers.

Now, combining the previously described MTJ and the FTJ it is possible to obtain an artificial multiferroic material, where ferroelectric and ferromagnetic orders coexist. Due to the interplay among magnetic, electric, and transport properties, these multiferroic heterostructures reveal new physics and could be used to design novel functional devices. Multiferroic tunnel junctions (MFTJs) exploit the capability to control electron and spin tunneling via ferromagnetic and ferroelectric polarizations of the MFTJ constituents [45]. A schema of MFTJ is shown in 1.18: it could be seen both as a particular type of MTJ where a ferroelectric thin film serves as a tunneling barrier, or as a particular type of FTJ that has ferromagnetic metal electrodes. The MFTJ represents a four-state resistance device where its resistance can be switched both by electric and magnetic fields, since TMR and

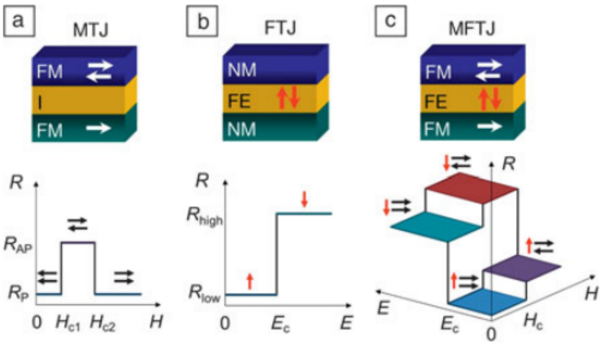

Figure 1.18.: A sketch of different types of junctions from [32]: (a) MTJ, (b) FTJ, (c) MFTJ. In the first one the tunneling resistance depends on direction of magnetization in the metallic electrodes. In the second one, it depends on the polarization orientation of the ferroelectric layer. In the third one, a join of the two previous resistance levels occurs yielding to a four level resistance device depending on both polarization and magnetization direction.

TER effects coexist, as reported by Zhuravlev et al [46, 47].

The heterostructure made with perovskite oxide films of $SrRuO_3$ (as ferromagnetic electrodes) and $BaTiO_3$ (as ferroelectric barrier) has been taken as a model of MFTJ and intensively studied by density functional calculations, revealing the key functional properties of this device and predicting the coexistence of TMR and TER effects. The Ref. [48] shows in detail as the TMR effect is the consequence of wavefunction symmetry conservation across the epitaxial $SrRuO_3/BaTiO_3$ interfaces: in the parallel magnetic configuration, because of the symmetry both spin channels contribute to the conductance, while in the antiparallel magnetic configuration, the conductance is strongly suppressed due to the symmetry mismatch, yielding a sizable TMR. On the other hand, as previously described, the TER effect originates from the asymmetric interface: RuO_2/BaO at one interface and TiO_2/SrO at the other one create a different polarization profile when the ferroelectric polarization is switched. Further, the ferroelectric polarization switching and the interfacial magneto-electric effect influences the spin polarized tunneling and TMR [49].

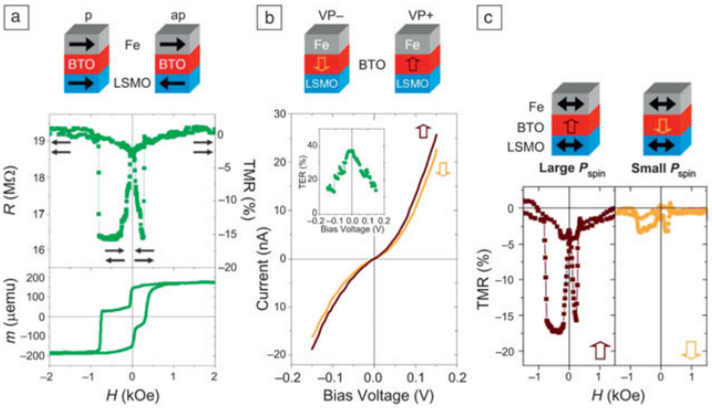

Figure 1.19.: Experimental assessment of the tunneling resistance when an electric or/and a magnetic fields are applied on a Fe/BaTiO$_3$/LSMO sample. Four level of resistance are recognizable but they are too close each other. Images from [32].

Garcia et al. [50] assessed experimentally the impact of ferroelectric polarization of the barrier on spin-dependent tunneling, probing a MFTJs composed of an La$_{2/3}$Sr$_{1/3}$MnO$_3$ (LSMO) electrode, a BaTiO$_3$ ferroelectric tunnel barrier (1 to 3 nm), and a Fe or Co counter-electrode. They found a large negative TMR at 4 K, reflecting a negative spin polarization for the Fe/BaTiO$_3$ interface. By applying short voltage pulses of ±1 V, they observed reversible changes of the tunnel resistance linked to the variation of the barrier height with the ferroelectric polarization direction, with a TER of about 30%. More interestingly, the amplitude of the TMR was also found to strongly depend on the direction of the ferroelectric polarization. As can be seen for a typical junction in Figure 1.19(c), the TMR measured at an applied bias voltage of –50 mV varies from a high value (–17%) to a low value (–3%) when the electrical polarization points toward Fe or LSMO, respectively. The observed change in TMR is consistent with the predicted change of the spin polarization at the Fe/BaTiO$_3$ interface and the induced magnetic moment on the interface Ti atoms, previously described. These results reveal that the spin polarization of tunneling electrons can be electrically tuned in MFTJs by switching the ferroelectric polarization of the barrier and demonstrate the existence of four level of resistance one for each combination of the ferroelectric and ferromagnetic states. By the way, here the main problem of MFTJ's applicability resides: resistance levels are too close each other, causing difficulties in the read/write process.

Triggered by these important theoretical and experimental results, we started an ab-initio study of a MFTJ, different in the ferroelectric barrier, that could go in the direction to enhance the separation of the resistance levels, increasing the TER effect.

2. $SrRuO_3/PbTiO_3/SrRuO_3$ MFTJ

In the following section I report the work published in the paper [127], whereby, as principal investigator, I perform all the calculations and great part of the analysis of their results, with my supervisor's support. Briefly, we will see that first-principles density functional calculations show that the $SrRuO_3/PbTiO_3/SrRuO_3$ multiferroic junction with asymmetric (RuO_2/PbO and TiO_2/SrO) interfaces has a large ferroelectric depolarizing field, whose switching changes the interface transmission probabilities for tunneling electrons, leading to electroresistance modulation over several orders of magnitude. The switching further affects the interface spin density, naturally driving magneto-resistance as well as modulated spin-dependent in-plane resistivity, which may be exploited in field-effect devices.

2.1. Introduction and method

Multiferroic junctions are stacks of metallic ferromagnets and insulating ferroelectrics where electroresistance and magneto-resistance modulation[101, 102] have been obtained via polarization switching in the ferroelectric interlayer. Ferroelectric (FE) materials –especially perovskite oxides– are used as tunnel barriers between metal electrodes. Polarization charges accumulate at the interfaces of the finite FE layer with the rest of the stack, and cause a depolarizing field in the FE. Despite the strong screening by the metal electrodes, a sizable field survives in typical junctions. This persistence is the basis for nanoscale device concepts for data storage.[103, 104, 105] A large ("writing") external bias across the FE is used to switch the FE depolarizing field and polarization, and a small ("reading") bias is then used to read the resistance of the stack in the newly realized state.

This resistance may –in fact, in the present case, does– depend on polarization (i.e. depolarizing field) orientation, for instance because of interface structure or of asymmetries in potential profile along the junction and the associated tunneling probability. If that is the case, an electroresistance effect is realized. When ferromagnetic (FM) electrodes are added to the junction, a multiferroic tunnel junction (MFTJ) is realized. Electron tunneling from the electrode through the FE barrier is now spin-dependent, and the tunneling current also depends on the relative orientation of magnetization of the two electrodes, or on the local induced magnetization. Thus, in MFTJs, tunneling magneto- and electro-resistance (TMR and TER) effects coexist, leading to four distinct states accessible via electric and magnetic external fields.[106, 107] Further, because of the same asymmetries, the interface polarization charge is spin-polarized to a degree depending on polarization direction. MFTJs may thus exhibit interfacial magneto-electricity (ME), i.e. changes in interface magnetization induced by FE polarization reversal, hence ultimately driven by an electric field.[108, 27] The polarization switching changes sign and value of the FE charge at a given interface, but also its relative majority or minority spin content, establishing a tunable interface magnetization. Of course, this will affect both the tunneling (typically ballistic) and the in-plane (typically diffusive) transport in either spin channel. In this paper, we study with first-principle calculations a $SrRuO_3/PbTiO_3/SrRuO_3$ (SRO/PTO/SRO) multiferroic tunnel junction, and specifically its tunneling electroresistance, interfacial ME coupling, and in-plane transport. Due to the chemical asymmetry of the interfaces and the strong polarization of the FE layer, the electroresistance modulation is up to two orders of magnitude larger than in previous studies on $BaTiO_3$-based MFTJs.[106, 109] We also find a smaller but potentially useful tuning of in-plane resistance, originating from polarization-induced magnetization changes. Interface ME is present, with coupling coefficients similar to other MFTJs. [110] The electronic and atomic structure of the SRO/PTO/SRO junction is calculated within density functional theory in the generalized gradient (GGA) approximation and the projector augmented wave (PAW) as implemented in the VASP code.[111] PTO has been relaxed in tetragonal symmetry, obtaining a=3.924 Å, c=4.176 Å, Ti-O on-axis bonds 1.79 Å and 2.38 Å, FE energy gain over paraelectric 108 meV, polarization P=0.86 C/m^2. PTO cells with this structure and cubic SRO have been stacked keeping the in-plane lattice constant of PTO. The two interfaces between insulator and metal, RuO_2/PbO at one side and TiO_2/SrO at the other, are labeled 'Ru' and 'Ti' below and are simulated in an in-plane 2×2 section. The supercell has 7 layers of PTO and 6 layers of SRO as short-circuited ferromagnetic electrode, for a total of 260 atoms. We consider the two ferroelectric states of PTO with polarization P pointing in opposite directions, perpendicular to the interfaces; all the quantities pertaining to P pointing from RuO_2/PbO to the TiO_2/SrO ("Ru to Ti") are depicted in blue, while those for P pointing from TiO_2/SrO to RuO_2/PbO ("Ti to Ru") are in red. All configurations are reoptimized in length and relaxed with force tolerance 40 meV/Å, using a 4×4×1 k-point Monkhorst-Pack mesh.

2.2. Results

2.2.1. Charge and potential

To analyze the total charge density (built adding narrow Gaussian charges at the ions location to the electronic charge) and electrostatic potential in the junction in the two polarization states, we feed their average over the sectional area $A{=}4a^2$ of our 2×2 planar cell to a one-dimensional square-wave filter to obtain the macroscopic average[112]

$$\bar{\bar{n}}(z) = \frac{1}{aA} \int\limits_{z-a/2}^{z+a/2} dz' \int\limits_{A} n(x, y, z')\, dx\, dy. \tag{2.1}$$

Similarly to Ref.[113], we extract the monopole component of the macroscopically averaged density as

$$\frac{1}{2}[\bar{\bar{n}}^{\rightarrow}(z - z_0) - \bar{\bar{n}}^{\leftarrow}(z_0 - z)] \tag{2.2}$$

combining the density profiles $\bar{\bar{n}}^{\rightarrow}$ and $\bar{\bar{n}}^{\leftarrow}$ for the two P states (z_0 is chosen to minimize the monopoles and ends up near the midpoint of the FE layer). The results are shown in Fig.2.1. Secondly, the asymmetric interfaces of highly polarized PTO produce quite different potential profiles for the two polarization directions,

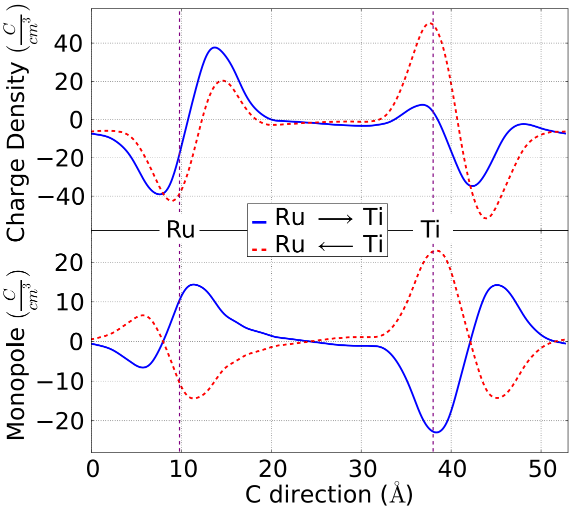

Figure 2.1.: Macroscopic average (top) of the total charge density, and its monopole component (bottom) for the two directions of P in PTO.

without any symmetry-breaking layer of other materials interposed between electrode and barrier.[109] This implies that the tunneling resistance along the junction will be changed by the switching of PTO polarization. As suggested by simplified models,[31] for such asymmetric potential and large residual electric field one expects a strong TER effect, which we now demonstrate calculating a) the semiclassical tunneling conductance through the 1D potential profile of the junction, and b) the transmission coefficient from the evanescent-wavefunction ratio in the insulator.

2.2.2. Tunneling electroresistance: WKB

To quantify the TER in our junction, we first study the semiclassical tunneling conductance through the 1D potential profile of the junction. An appropriate model for the potential profile through which the electrons tunnel is the position-dependent conduction band edge of the junction referred to Fermi energy E_F. To extract this profile, we calculate for the two polarization orientations the layer-resolved local density of states (LDOS), which is displayed in Fig.2.3. The position dependent PTO band edges shift along the junction at a rate determined by the depolarizing field, whose value is in the mid 10^8 V/m as already indicated by the

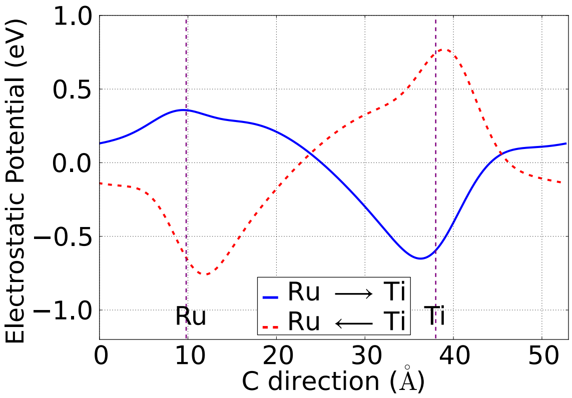

Figure 2.2.: Asymmetric electrostatic potential profiles along c for opposite P's in PTO. The depolarizing field is ~5×10^8 V/m.

averaged potential profile. We then extract from the LDOS the position of the conduction edge in each layer, and use it to construct the potential profiles for the two values of P, which, as shown in Fig.2.4, are strongly asymmetric. We then calculate the tunneling probability in the semiclassical Wentzel-Kramers-Brillouin approximation through these two profiles vs. injection energy, choosing the Fermi energy as zero. (This describes electrons tunneling into the PTO conduction band. Hole tunneling is neglected due to the large barriers and effective masses.) As shown in Fig.2.5 the ratio $G_{\rightarrow}/G_{\leftarrow}$, i.e. the TER, is between 50 and 350 depending on energy, and therefore up to two orders of magnitude larger than in BaTiO$_3$/SRO junctions.[106] The absolute values of G are comparable with those found for similar junctions. We note that if we roughly estimate the writing voltage needed to reverse the depolarizing field in this structure as the field times the PTO thickness we find $E{\cdot}d{\sim}2$ V; thus, it would be safe to use a standard[115] reading voltage of 0.5-0.6 V, which would yield a near-maximum TER.

2.2.3. Tunneling electroresistance: Transmission function

The second indication of a giant TER effect comes from the two transmission functions $T^{\rightarrow,\leftarrow}\left(\mathbf{k}_{||}\right)$ across the two interfaces in the two poling directions. For not too thin a barrier, the transmission function of a tunnel junction could be

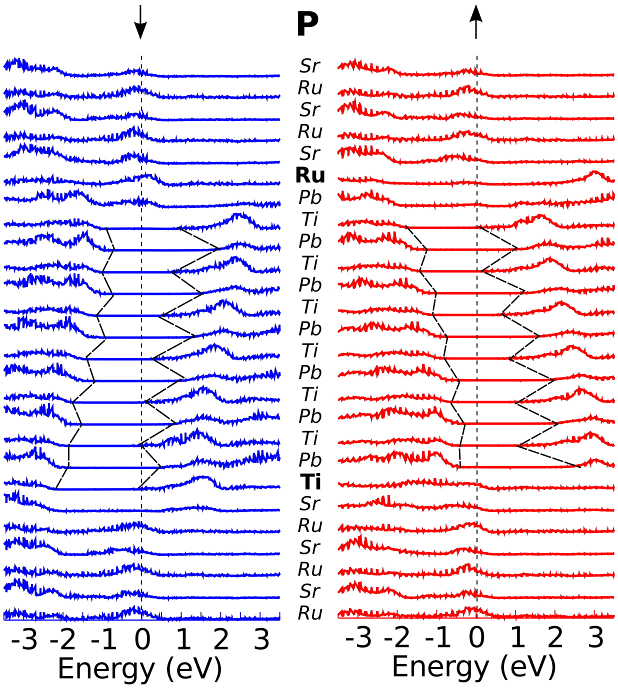

Figure 2.3.: LDOS for the two polarization states.

factorized[117] as

$$\begin{aligned} T^{\rightarrow}\left(\mathbf{k}_{||}\right) &= t_{\mathrm{Ru}}^{\rightarrow}\left(\mathbf{k}_{||}\right)\exp\left(-2\kappa\left(\mathbf{k}_{||}\right)d\right)t_{\mathrm{Ti}}^{\rightarrow}\left(\mathbf{k}_{||}\right) \\ T^{\leftarrow}\left(\mathbf{k}_{||}\right) &= t_{\mathrm{Ru}}^{\leftarrow}\left(\mathbf{k}_{||}\right)\exp\left(-2\kappa\left(\mathbf{k}_{||}\right)d\right)t_{\mathrm{Ti}}^{\leftarrow}\left(\mathbf{k}_{||}\right) \end{aligned} \tag{2.3}$$

where d is the barrier thickness, $\kappa\left(\mathbf{k}_{||}\right)$ is the lowest decay rate in the barrier and $t_{\mathrm{Ru,Ti}}^{\rightarrow,\leftarrow}$ are the transmission probabilities from the left or right electrode into the barrier across the interfaces (Ru or Ti respectively) for an electron with a given $\mathbf{k}_{||}$, for both polarization directions. In our junction, the two interfaces differ both chemically and electrostatically depending on the direction of polarization, hence we have four different t's to assess. Assuming the same exponential decay for the two polarizations, we have

$$\frac{T^{\rightarrow}}{T^{\leftarrow}} = \left(\frac{t_{\mathrm{Ru}}^{\rightarrow}}{t_{\mathrm{Ti}}^{\leftarrow}}\right)\cdot\left(\frac{t_{\mathrm{Ti}}^{\rightarrow}}{t_{\mathrm{Ru}}^{\leftarrow}}\right). \tag{2.4}$$

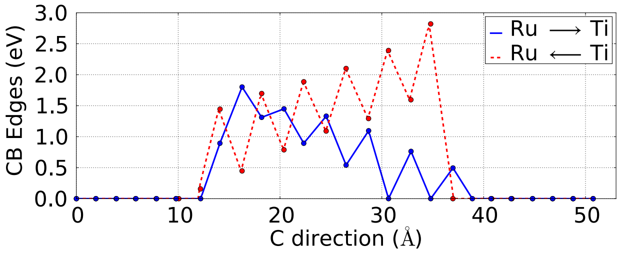

Figure 2.4.: CB edge potential profile for tunneling.

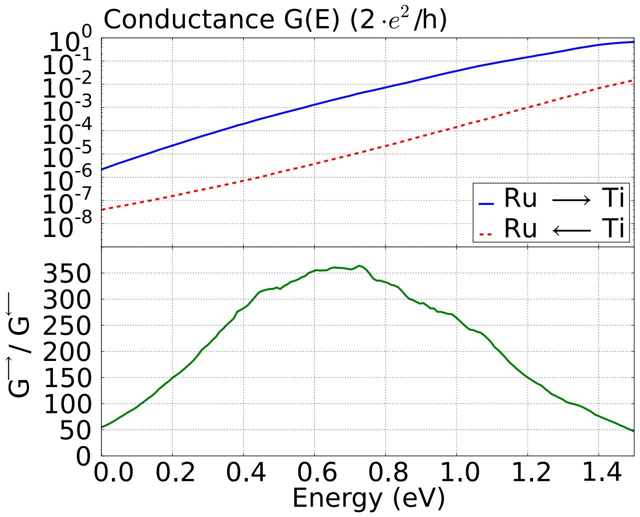

Figure 2.5.: Top: conductance in the WKB approximation for tunneling through the 1D potential profiles shown in Fig. 2.4. Bottom: the TER between the two P states, topping at about 350.

The two t ratios can be extracted from the ratio of the density of metal-induced gap states at distance z from the two interfaces for the two poling directions, i.e.

$$\left|\psi^{\rightarrow;\leftarrow}_{\mathrm{Ru,Ti}}\right|^2 \propto t^{\rightarrow;\leftarrow}_{\mathrm{Ru,Ti}}\left(\mathbf{k}_{||}\right)\exp\left[-2\kappa\left(\mathbf{k}_{||}\right)z\right]. \tag{2.5}$$

The upper panels of Fig.2.6 shows the wavefunctions as function of z for $\mathbf{k}_{||}$=0 at the Fermi energy along the junction for the two polarization directions, and the lower panels display their ratios. Thus, $t^{\rightarrow}_{\mathrm{Ru}}/t^{\leftarrow}_{\mathrm{Ti}}$~25 and $t^{\rightarrow}_{\mathrm{Ti}}/t^{\leftarrow}_{\mathrm{Ru}}$~10, so that the transmission ratio $T^{\rightarrow}/T^{\leftarrow}$ is about 250, a measure of the TER comfortingly similar to the WKB result shown above.

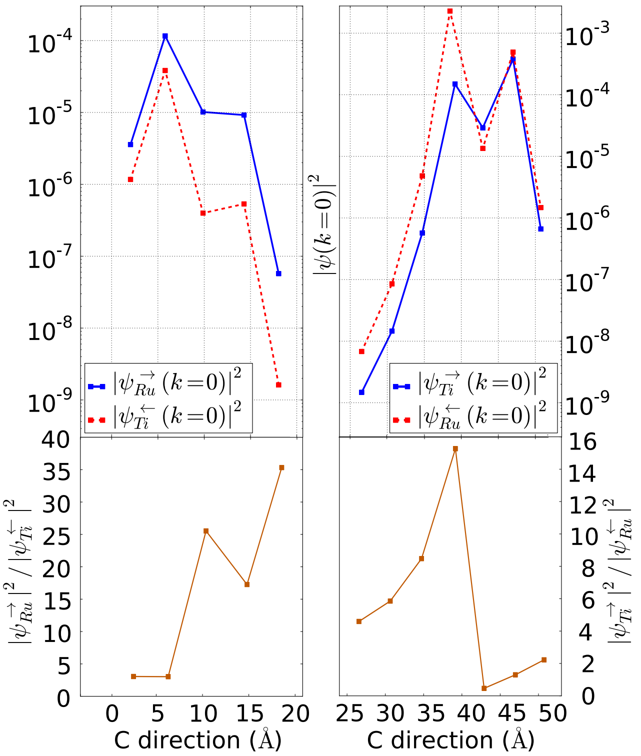

Figure 2.6.: Probability densities at the Fermi energy and $\mathbf{k}_{||}=0$ (top) and their ratio (bottom) for the two polarization directions near the interfaces. Values taken at Ti sites

2.2.4. Interface barriers and the origin of asymmetry

The asymmetry giving rise to the large TER is of electronic origin. This can be seen from the LDOS in Fig.2.3: at the Ru-Sr-Ti interface (bottom right in Fig.2.3), the PbO layer opposes a large barrier to tunneling, while the TiO_2 layer adjacent to SRO is metallized; at the Ru-Pb-Ti interface (top left in Fig.2.3) the PbO layer in contact with SRO is metallized, and the first barrier is the smaller one provided by the TiO_2 layer. Put differently, the conduction Schottky barriers between SRO and PTO for the two interfaces are different; indeed, our estimated difference in the conduction edge position at the interface agrees with the calculated[120] 0.7 eV difference between Schottky barriers of the two interfaces.[133] Since despite the gap underestimate in GGA this difference is well reproduced, both the TER and the absolute tunneling conductance should be considered quite accurate. We conclude that the smaller TER asymmetry in SRO/$BaTiO_3$ is related to its lesser or absent Schottky barrier asymmetry.[121] Ionic screening, in turn, presents no significant surprise: cationic displacements in the junction are rather well behaved, as shown by Fig.2.7; they agree largely with previous estimates[120] and are fairly similar to BTO/SRO (although here they are larger on average consistently with the larger polarization of PTO).

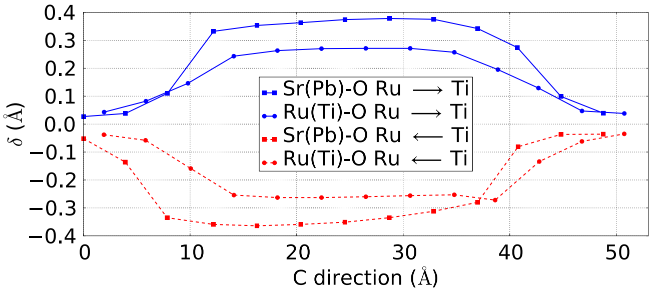

Figure 2.7.: Cation displacement with respect to the plane of surrounding oxygens.

2.2.5. Interface magnetoelectricity

We now consider the interface ME effect. We elect to estimate the interface ME coefficient α assuming a linear magnetization-field relation

$$\mu_0 \Delta M = \alpha E. \tag{2.6}$$

Given the likely importance of non-linearity for the high fields involved here, this should be considered an order-of magnitude estimate. There is some latitude in deciding which magnetization changes are to be considered, depending on the operational procedure or application envisaged. In the present context, the natural scenario is polarization switching: ΔM is the integrated difference of magnetization density at each interface between the two polarization states. Clearly, two interface-related ME coefficients will result, either one of which will be relevant in practice depending on which interface is active in the specific experiment or application. To operationally implement this scenario, one just needs to switch P via the writing voltage. To calculate the ΔM's we define in analogy to the charge density in Sec.2.2.1 the macroscopic averages of the magnetization density

$\overline{\overline{m}}^{\rightarrow}(z)$ and $\overline{\overline{m}}^{\leftarrow}(z)$ for the two states Ru→Ti and Ru←Ti of PTO polarization. In Fig.2.8 we report the planar and macroscopic averages To calculate the α's we

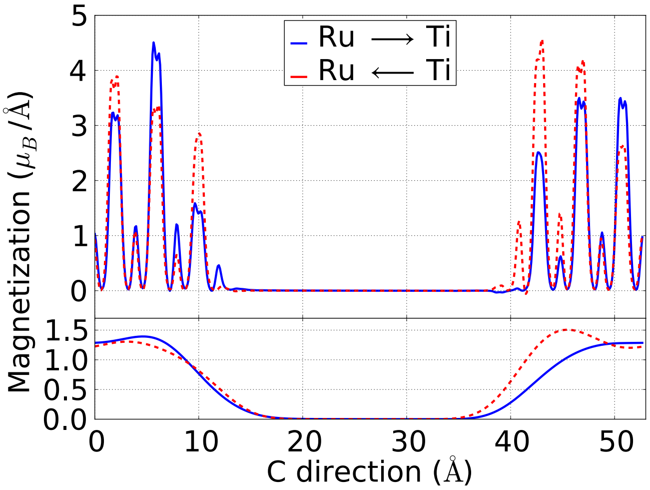

Figure 2.8.: Planar and macroscopic averages of the magnetization in the two P states.

conventionally choose the initial P state to be Ru→Ti and the final state Ru←Ti. The magnetization changes at the Ru or Ti interface are

$$\begin{aligned} \Delta M_{\mathrm{Ru}} &= \int\limits_{\mathrm{Ru}} (\overline{\overline{m}}^{\rightarrow} - \overline{\overline{m}}^{\leftarrow})\, dz \\ \Delta M_{\mathrm{Ti}} &= \int\limits_{\mathrm{Ti}} (\overline{\overline{m}}^{\rightarrow} - \overline{\overline{m}}^{\leftarrow})\, dz, \end{aligned} \tag{2.7}$$

where the integrals are done near each interface between the region of zero magnetization within PTO and the region of constant magnetization within SRO, specifically (see Fig.2.8) between 2 and 21 Å for the Ru interface, and 31 and 49 Å for the Ti interface. We choose as electric field in Eq.2.6 the depolarizing field E_{dep}, which is taken positive by convention (a different choice will simply change the sign of both ME coefficients). We then obtain the ME coefficients as

$$\alpha_{\mathrm{Ru}} = \frac{\mu_0 \Delta M_{\mathrm{Ru}}}{E_{\mathrm{dep}}}, \quad \alpha_{\mathrm{Ti}} = \frac{\mu_0 \Delta M_{\mathrm{Ti}}}{E_{\mathrm{dep}}}. \tag{2.8}$$

Table 3.1 summarizes the induced magnetizations (Eq.2.7) and the ME coefficients at the two interfaces (Eq.2.8). Again the asymmetry in the interfaces shows up dramatically. The ME coefficients are somewhat smaller than those predicted for other similar MFTJs,[27, 110] despite our induced magnetizations being larger. This is due to our assuming conservatively a switching electric field larger than typical operational coercive fields of PTO. These may be 5 to 20 times smaller depending on external conditions and sample properties (and hence the α_s could be larger by the same factors). Some additional insight can be gained by examining in Fig.2.9 the atom-resolved average magnetic moments obtained integrating the magnetization density within atomic spheres defined by the PAW construction. Consistently with its larger ME coefficient, the Ti interface (right side of each panel) is more magnetically polarizable than the Ru interface. For Ru←Ti polarization (right panel), magnetization builds up in the first Ru layers, spilling over into the Ti metallized layer and through to the first insulating PbO layer. In Ru→Ti polarization (left panel), the interface Ru's lose some (and Ti and oxygens, all) of their moment. At the Ru interface (left side of each panel), the magnetization does not extend at all into PTO (specifically in the PbO layer) in either case, and the SRO magnetization mostly redistributes among Ru's and O's in the first and second layer, changing only slightly overall (see also Fig.2.8). In closing this Section, we note that another possible choice for ΔM is the interface magnetization density change with respect to zero electric field. In our case, this translates into the magnetization difference at the two interfaces with or without the depolarizing field, i.e. for ferroelectrically-distorted or paraelectric PTO. As P, i.e. the field, can be turned on in two ways, this procedure produces four ME coefficients, $\alpha^{\rightarrow}_{\rm Ru}\simeq\alpha^{\leftarrow}_{\rm Ru}$=0.62, $\alpha^{\rightarrow}_{\rm Ti}$=0.14, $\alpha^{\leftarrow}_{\rm Ti}$=1.75, in units of 10^{-11}G·cm^2/V. This polarization "turn-on" scenario, unfortunately, is essentially impracticable. It would require forcing PTO across its ferroelectric transition, e.g. by lowering the temperature

Table 2.1.: Magnetization changes ($\mu_{\rm B}$ per interface cell) and ME coefficients (10^{-11}G·cm^2/V) upon switching P from Ru→Ti to Ru←Ti.

Interface	ΔM	α
Ru	–0.31	–0.11
Ti	4.46	1.62

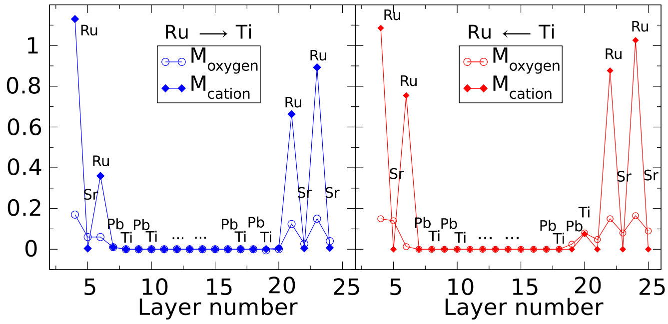

Figure 2.9.: Atom-resolved magnetization (μ_B per atom) for the two polarization states (a few SRO layers omitted).

across the Curie point T$_c$, with a small poling voltage applied to the junction to select the desired P state. This is largely incompatible with device operation due to the high T$_c$≃500° C.

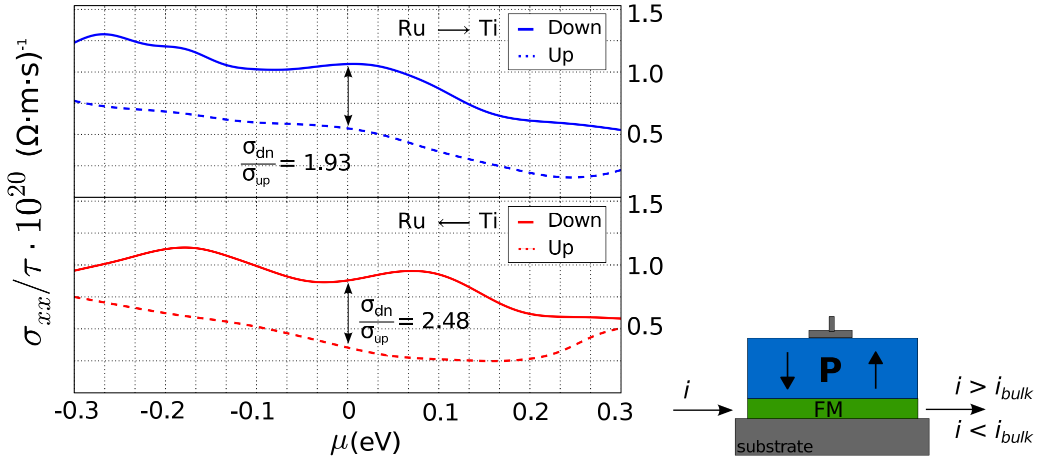

Figure 2.10.: In-plane spin-resolved conductivity vs chemical potential for the two polarization states. Bottom: schematic device concept exploiting conductivity modulation.

2.2.6. In-plane conductivity modulation

The sizable interface asymmetry and ME coupling will influence the in-plane current in the SRO layer. To assess this effect, we use the BoltzTraP[118] code to calculate the conductivity in the plane of the junction in the diffusive regime as

$$\sigma_{\alpha\beta}\left(T;\mu\right) = \frac{1}{\Omega}\int \sigma_{\alpha\beta}(\epsilon)\left[-\frac{\partial f\left(T;\epsilon\right)}{\partial\epsilon}\right]d\epsilon \tag{2.9}$$

with

$$\sigma_{\alpha\beta}\left(\epsilon\right) = e^2\sum_{i\mathbf{k}}\tau_{i,\mathbf{k}}v_\alpha\left(i,\mathbf{k}\right)v_\beta\left(i,\mathbf{k}\right), \tag{2.10}$$

where i is a band index, τ a relaxation time, v the group velocity calculated from the band structure, and f the occupation function. Assuming τ constant, we can plot σ/τ vs chemical potential. Although the scattering mechanisms may not be described in full detail, this approximation is quite sufficient to address conductivity ratios between polarization states. (We note in passing that diffusive conductivity is appropriate for in-plane transport, but may be inapplicable to tunneling transport depending on the nature of the Fermi surface of the junction system. In the present case this approach gives a TER $\sim 10^5$ which, while consistent with similar calculations for 1+6 PTO/SRO superlattices,[122] is probably significantly overestimated.) The in-plane spin-resolved conductivity in the diffusive regime in the two polarization states is shown in Fig.2.10. The total conductivity changes by 35% upon polarization switching. Also, the switching modulates the down to up-spin conduction ratio (2.5 to 1.9) by ±15% compared to the calculated bulk value (2.2). Such sizable modulations may be employed in in-plane field-effect devices such as that sketched in Fig.2.10. The electrically-stored polarization orientation could be read electrically from the current modulation in the metal channel, i.e., effectively, as a modulated resistivity; this could be done either with the total current, or one of the spin components if polarized contacts are used. Another application of this configuration may be a filter or modulator of the incoming current, measuring the outgoing spin-polarized current calibrated to that of the bulk. Note that our calculations measure the conduction within the whole PTO/SRO layer system, and there is no way to single out the net contribution of each interface; the exact values of the modulation will thus depend on SRO thickness, and will change if one of the interfaces (e.g. SRO/substrate) is “ferroelectrically dead”.

2.3. Summary

In conclusion, we considered a multiferroic tunnel junction with asymmetric interfaces and a large-polarization FE. Very different potential profiles result for the two polarization states, and lead to a giant TER of up to 350. The interface charge accumulation is spin-polarized, with magnetization and magnetization changes depending on the interfaces and on polarization orientation, with sizable ME coefficients. The ME coupling affects the in-plane diffusive transport of the junction changing the majority to minority conductivity ratio, as well as the total conductivity. In particular, upon P inversion, the conductivity is modulated by 35% and its spin polarization by ±15%, which is presumably exploitable in practical applications. In forthcoming work we plan to study TMR, which may be expected to be high also, as well as the effects of magnetic doping of the FE layer.

3. V doping of $PbTiO_3$

In this section, I report a conference proceeding [12], whereby I perform all calculations aimed to *ab initio* predictions on the proper multiferroic (ferromagnetic, insulating and ferroelectric) character of $PbTiO_3$ doped with vanadium. V impurities coupled ferromagnetically carry a magnetization of 1 μ_B each. The coupling is expected to be strong, since the paramagnetic solution is higher by 150 meV/vanadium, and no stable antiferromagnetic solution was found. The electronic gap in the doped system is about 0.2-0.3 eV in GGA, hence the system is properly multiferroic. V doping increases the spontaneous polarization in $PbTiO_3$, with an approximate perceptual rate of 0.7 $\mu C/cm^2$.

Here we report the first principles prediction of a multiferroic state of lead titanate doped with magnetic vanadium. PTO is a well-known tetragonal perovskite with a high spontaneous polarization (86 $\mu C/cm^2$) of displacive origin. $PbVO_3$ also happens to be tetragonal, and with an even higher spontaneous polarization (152 $\mu C/cm^2$). Previous studies have shown its ground state to be an antiferromagnetic insulator (C-type), making it not especially interesting as a multiferroic. Motivated by our previous study of V-doped ferroelectric titanates [127], we examine the magnetic properties of vanadium diluted within the robust PTO ferroelectric.

Ab initio calculations are performed within density functional theory in the generalized gradient approximation (GGA) by Perdew-Wang using the PAW method [213] as implemented in the VASP code [210]. Standard cutoff is used for the plane wave basis, and the k-point mesh for the bulk is 8×8×8 (appropriately rescaled for defect super cells). The Berry phase technique is used to calculate the polarization change upon V doping, using strings of 16 points in the polarization direction.

After studying PTO and PVO in the respective ferroelectric phases, we substituted V for one Ti in a 2×2×2 tetragonal supercell of ferroelectric PTO, i.e. dopant concentration ∼12.5%. A selection of structure parameters (lattice con-

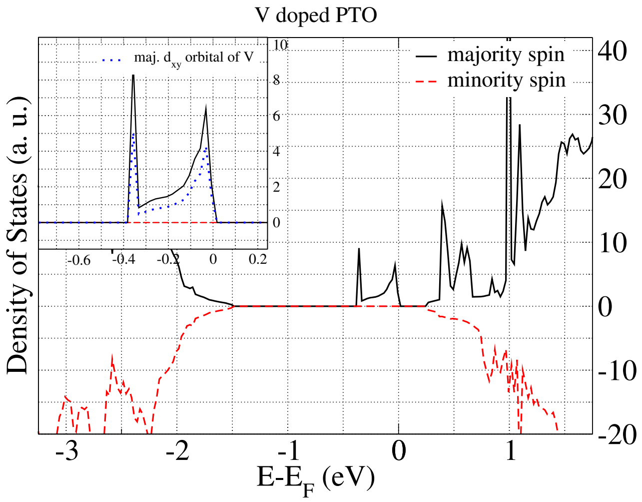

Figure 3.1.: Density of states for V:PTO. Positive curve is majority spin, negative is minority spin. Fermi energy is at 0 eV. Inset shows a zoom of the gap peak. The dotted line is a V *d*-up.

stants, distance of V or Ti from neighbouring O along the polar axis) are collected in Tab. 3.1. V has one excess electron compared to Ti, so it is, as expected, spin-polarized with a moment of 1 μ_B. Orbital angular momentum is assumed to be quenched. Fig. 3.1 displays the key result, i.e. the density of states (DOS) of ferromagnetic V:PTO. As we can observe, a fully occupied peak appears in the gap of PTO, placed so that a gap of about 0.2 eV survives. This DOS feature is obviously related to the excess V electron occupying antibonding conduction states. Indeed, as shown in the inset, the main contribution to that peak is that of spin-up *d* orbitals of V. Thus, PTO doped with vanadium is a small-gap ferromagnetic insulator thanks to the unpaired electron of dopant vanadium. The gap of PTO is of course underestimated due to the known [53] gap error of semi-local functionals; it may well be that the small V-related gap be also somewhat larger than calculated due to the same effects (self-interaction, xc discontinuity, etc.). In the cell just discussed, V is ferromagnetic by construction, being coupled to its periodic images. To study an antiferromagnetic configuration we consider two V's at the same concentration in a $2\sqrt{2}\times2\sqrt{2}\times2$ tetragonal cell. The two V are placed in that cell as far as possible from each other. While the ferromagnetic configuration is stable, the antiferromagnetic configuration is not. The V moments disappear

	V:PTO	PTO (Theor. / Expt.)	PVO (Theor. / Expt.)
a	7.848	3.924 / 3.895	3.806 / 3.804
c	8.351	4.175 / 4.171	4.979 / 4.677
V-O_{top}	1.709	-	1.700 / 1.677
V-O_{down}	2.377	-	3.278 / 3.01
Ti-O_{top}	1.792	1.795 / 1.75	-
Ti-O_{down}	2.380	2.380 / 2.42	-

Table 3.1.: Cell parameters for V doped PTO, bulk PTO and PVO. Theoretical values are calculated for this work in GGA approximation. Experimental values are from Ref. [101, 113]

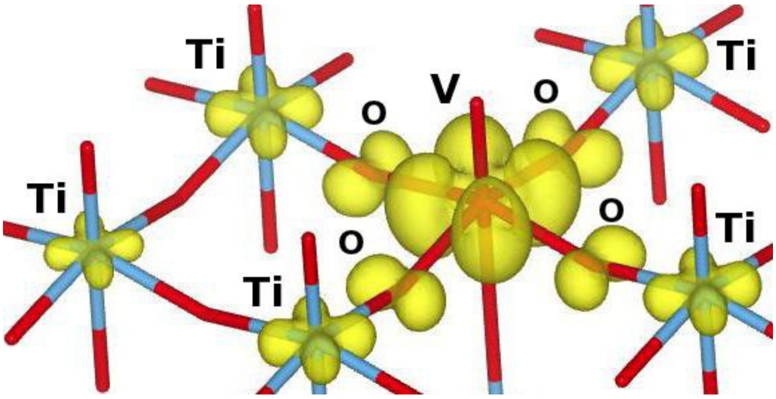

Figure 3.2.: Majority spin density of the spin-polarized electron of V in the basal plane (iso-level: $10^{-3}\,e/\text{Å}^3$). The state is anti-bonding with first-neighbor O's, has d_{xy}-like nodal structure, and propagates through d_{xy}-like Ti states. Charge paths along the vertical axis are negligible.

and the system converges to a metallic Pauli paramagnet of zero moment, which is about 300 meV higher in energy than the ferromagnet. Of course, this prevents the evaluation of a coupling parameter for magnetic models, but the ferromagnet seems quite stable nevertheless.

Inspection of the charge density of the impurity state (Fig. 3.2) suggests a d_{xy}-like nodal structure and coupling of V's via V-O-Ti-O-... paths in the basal plane, whereas hardly any density is to be found along the vertical axis. While the V-centered state is, as expected, anti-bonding with first neighbors, the bonding O-V states (which mimic those of the substituted Ti) appear to make for a larger charge accumulation in the V-O bond region (Fig. 3.3), matching the shorter V-O

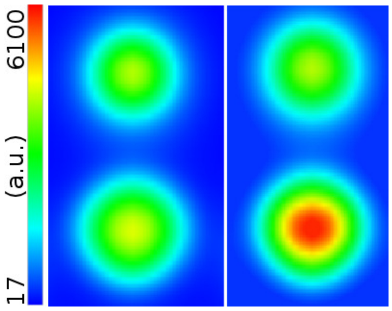

Figure 3.3.: Total charge density (in arbitrary units) in the vertical plane across a Ti-O bond in PTO (left) and a V-O bond in V:PTO. A slightly larger bond charge can be appreciated in V:PTO.

bond length compared to Ti-O (1.71 vs 1.79 Å).

Following Ref.[102], the equilibrium concentration is $[\mathrm{V}]{=}N_s \exp\left(-\mathrm{E_f}\left(\mathrm{V}\right)/\mathrm{kT_g}\right)$, Finally, we estimated the changes in polarization induced by V doping. At 12.5% V we find a polarization increase of 8.3 μC/cm^2, which agrees nicely with 8.25 μC/cm^2 obtained by linear interpolation between the bulk values of PTO and PVO mentioned previously. Therefore, in terms of polarization, V does not seem detrimental, but in fact benign.

During review we have become aware of a very recent study [54] of transition-metal doping in a perovskite ferroelectric ($BaTiO_3$), reporting results in general agreement with the ones just presented.

To conclude this section, I mention a survey that I have just started about doping the $SrRuO_3/PbTiO_3/SrRuO_3$ interfaces with vanadium (V). Our intention was that of improving both TER and interfacial ME effects, with a further difference at the interfaces due to a magnetic atom as V. We assessed the supercell where one of the four interfacial Ti is substituted with a V atom, for both polarization orientations. In essence, we did not find any significant difference in both electrostatic potential and induced spin density respect with we found for the undoped heterostructure. However, it remain an open and interesting issue to investigate, as an example the first next step could be the study of Ru interface doped with V atom.

4. Prediction of a native ferroelectric metal

In the following, I report an on-going work where, using first-principles calculations, we predict that the layered perovskite $Bi_5Ti_5O_{17}$ is a ferroelectric metal, i.e. it has nonzero density of states (DOS) at the Fermi energy E_F and metal-like conductivity coexisting with spontaneous polarization in zero field and switchable depolarizing field in a finite system. This is, to our knowledge, the first known example of coexistence of native electric polarization and native metallicity in a single bulk phase. My personal contribute has been about the search for depolarizing fields in the finite $Bi_5Ti_5O_{17}$ system.

4.1. Introduction

The possibility that metals can support ferroelectricity is an intriguing open issue in solid state physics. Anderson and Blount [203] showed that certain martensitic phase transitions involve inversion symmetry breaking, formally implying the existence of a polar axis in metals. “Metallic ferroelectric” behavior has thus been claimed for metals falling under this definition – i.e., undergoing centrosymmetric (CS) to non-CS structural transition – such as [204] Cd_2ReO_7 and $LiOsO_3$, or being natively non-CS [205] such as $(Sr,Ca)Ru_2O_6$. The same label has been attached to ferroelectric insulators whose polar distortion survives moderate metallicity induced by doping or proximity (for example, residual local electric polarization in $BaTiO_{3-\delta}$ up to $\delta \approx 0.09$, and incomplete metallic screening of depolarizing fields in metal-ferroelectric magnetoresistive junctions [103, 11]). However, it is fair to say that neither any of the systems mentioned, nor in fact any other to our knowledge, actually embodies a ferroelectric metal, which should satisfy a minimal checklist arguably including i) nonzero density of states (DOS) at the Fermi energy E_F and metal-like conductivity, ii) spontaneous polarization in zero field, and iii) finite and switchable depolarizing field in a finite system. In this paper, we report the first –to our knowledge– prediction of a genuine ferroelectric metal satisfiying the above requirements, the layered perovskite $Bi_5Ti_5O_{17}$ (Bi5517), which has a large spontaneous polarization orthogonal to the plane of maximum conductivity, a metallic DOS, and a depolarizing field (upon a moderate amount of doping with Ca). Our focus are layered perovskite titanates $A_nTi_nO_{3n+2}$ [206, 207], whose morphology foreshadowing low-dimensional behavior combines with their tunable conduction charge: assuming fixed ionic charges for A^{3+} and O^{2-}, Ti has nominal ionicity $(3+4/n)$, i.e., between 4+ for n=4 (the band insulator $La_2Ti_2O_7$, known for its record-high ferroelectric critical temperature of 1770 K) and 3+ in the $n=\infty$ limit (the Mott-insulating Ti-d^1 perovskite $LaTiO_3$). The metallic $n>4$ phases are not nearly as studied theoretically as the end compounds [208, 132]. Motivated by experimental reports of possible non-CS structures in n=5 phases [209], here we study $La_5Ti_5O_{17}$ (La-5517 hereafter) and $Bi_5Ti_5O_{17}$ (Bi-5517). For the first-principles density-functional calculations we combine the local density approximation to density-functional theory as implemented in VASP [210] and the variational pseudo-self-interaction-corrected (VPSIC) density-functional approach [132, 56] (successfully applied to many oxide heterostructures [211]) to analyze the structural instabilities and the electronic structure. In the VPSIC code we use ultrasoft pseudopotentials [212] with plane-wave cutoff 476 eV, and in VASP we use projector augmented waves [213] and plane-wave cutoff 500 eV. Brillouin zone integration is done on 4×4×4 and 12×4×8 grids for self-consistency and density-of- states, respectively. For transport, we use a refined version of Bloch-Boltzmann transport theory [214], interpolating the band structure over a 30×14×22 ab-initio calculated k-point values. To compute the electronic polarization we use a modified Berry phase [215] approach described below.

4.2. Structure

As shown in Fig.4.1, the n=5 layered titanate can be viewed as a stack of slabs containing five [011]-oriented perovskite-like planes and with an AO termination.

(We give directions in the pseudo-cubic setting defined by the principal axes of the perovskite structure.) The crystal axes are **b**||[011], which will be shown to coincide with the polar axis, and **a**=[100], **c**=$[0\bar{1}1]$, which define the plane hosting the low-dimensional electron gas. Our supercell, comprising (as shown in Fig.4.1) two 5-layer blocks along **b**, is compatible with all structures of interest here. To identify the ground state, we start from the high-symmetry ($Immm$ space group) structure, and condense all its unstable distortions as obtained from a Hessian analysis (a summary is in Table 4.1I). For La-5517, the ground state is CS $Pmnn$, barring the existence of polarization. (We also simulate the experimentally-proposed structure of Ref. [209], but find it to be a high-energy non-equilibrium configuration.) Inspired by the observation that perovskites where Bi^{3+} replaces La^{3+}, such as $BiFeO_3$ [216], are usually ferroelectric due to the Bi^{3+} tendency to form low-coordination bonds, we explored symmetry breaking in Bi-5517, obtained by replacing all La atoms with Bi's. As in La-5517, the $Immm$ phase of Bi-5517 is a relatively high-energy saddle point (Table 4.1). However, at variance with La-5517, $Pmnn$ is also a saddle point for Bi-5517. We then condense the unstable distortions of the $Pmnn$ structure, preparing low-symmetry initial configurations obtained by quasi-random off-centering of Bi atoms. We identify as lowest-energy solution the non-CS $Pm2_1n$ space group (i.e., with no mirror plane perpendicular to the stacking direction [011]). The displacements of Bi cations (highlighted by arrows in Fig.4.1) are of two basic types. The Bi's at the block edges (Bi_e in Fig. 4.1) go off-center, but their displacements at the two block sides are symmetric with respect to the central layer (an anti-ferroelectric configuration of sorts) and give no net dipole; the same is true for the smaller displacements of the Bi_m in the intermediate layer [217]. On the other hand, the Bi_c's in the central layer of the block, while CS in both $Immm$ and $Pmnn$, move off-center in $Pm2_1n$; a net, uncompensated electric dipole along **b** is expected, as we now discuss.

4.3. Polarization

As expected from its structure, $Pm2_1n$ Bi-5517 indeed possesses a robust spontaneous polarization $P_{\rm tot}$ along the [011] direction. Table 2 reports the results. Remarkably, the total calculated $P_{\rm tot}$=33 μC/cm^2 is in the same league as ferroelectric

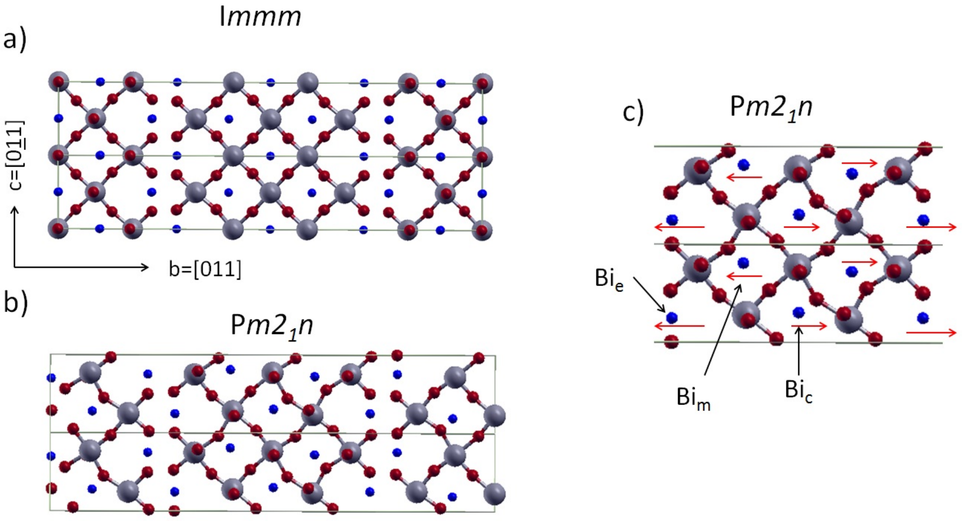

Figure 4.1.: Sketch of the structure of (a) *Immm* Bi-5517 and (b) $Pm2_1n$ Bi-5517. Bi is blue, O is red, and Ti is grey. The supercell axes are also indicated (**a**=[100] is orthogonal to the page). Cell is doubled along **c** to visualize the octahedral tilts. Panel (c) schematizes atomic displacements in a single 5-layer block. Arrows mark the shifts of Bi atoms from their high-symmetry positions. Bi displacements in the edge (Bi_e) and intermediate layers (Bi_m) compensate in an approximate way, but Bi_c in the central layer goes off-center giving rise to an uncompensated polarization along **b**.

perovskites (30 μC/cm^2 for $BaTiO_3$, for example). Ferroelectricity originates from Bi atoms moving off-center in the perovskite framework (Fig.4.1); this displacement is invertible with respect to the (011) plane, and should enable hysteresis. The ferroelectric well depth of 0.31 meV/Å^3 estimated from energy differences suggests a critical temperature upward of 500 K, by comparison with $La_2Ti_2O_7$. As discussed below, Bi-5517 is a metal. The calculation of polarization in metals is, to our knowledge, unprecedented. A technical qualification is therefore warranted. The electronic component of the polarization has contributions P_{val} from the occupied valence manifold and P_{cond} from the partially occupied conduction manifold. We implement two strategies to evaluate the last and most critical term. The first is based on the Berry phase approach, which shows that polarization in crystals is the integrated current flowing through the system as atoms displace

Table 4.1.: Energy (eV/cell) and lattice constants (Å) of various phases of La-5517 and Bi-5517. a, b, c are the lengths of the crystal vectors, which are parallel to the [100], [011], and $[0\bar{1}1]$ directions, respectively. The ground states are $Pm2_1n$ for Bi-5517 and $Pmnn$ for La-5517. Other energies are referred to these ground-states. Experimental lattice parameters for La-5517 are also reported for comparison.

	La-5517				Bi-5517			
Phase	E	a	b	c	E	a	b	c
$Immm$	0.74	3.885	31.276	5.439	1.55	3.863	31.461	5.435
$Pmnn$	0	3.912	30.805	5.422	0.21	3.902	30.975	5.418
$Pm2_1n$	–	–	–	–	0	3.890	31.100	5.461
Expt		3.929	31.466	5.532	–	–	–	–

Table 4.2.: Calculated polarization in μC/cm^2 for the $Pm2_1n$ ground-state of Bi-5517. The reference CS state is $Immm$. The conduction-electron contribution is calculated with both the Berry-phase approach and real-space integration (in brackets).

P_{ion}	P_{val}	P_{cond}	P_{tot}
55.52	–14.62	–7.52 (–4.0)	33.38

from CS (λ=0) to non-CS (λ=1): The second, entirely independent strategy is to obtain P_{cond} as the dipole associated to conduction electrons within 5-layer blocks in Bi-5517. This procedure would be exact if the conduction charge were confined within the block (which it largely is, the interblock overlap being small). In Fig.4.2 we compare the planar-averaged conduction charge of $Pm2_1n$ and of a CS system with $Pm2_1n$ cell parameters and $Immm$ atomic positions. The $Pm2_1n$ displacements produce an evident symmetry breaking, and a dipole appears within each block; a strong 2D charge confinement is also apparent, in agreement with the band structure analysis below. P_{cond} is the conduction contribution to the block dipole,

4.4. Band structure and confinement

$Pm2_1n$ Bi-5517, albeit polarized, is a metal, as can be seen in Fig. 4.3(a) from its atom- and orbital-resolved DOS. The conduction-electron density is low, 2.9×10^{21}

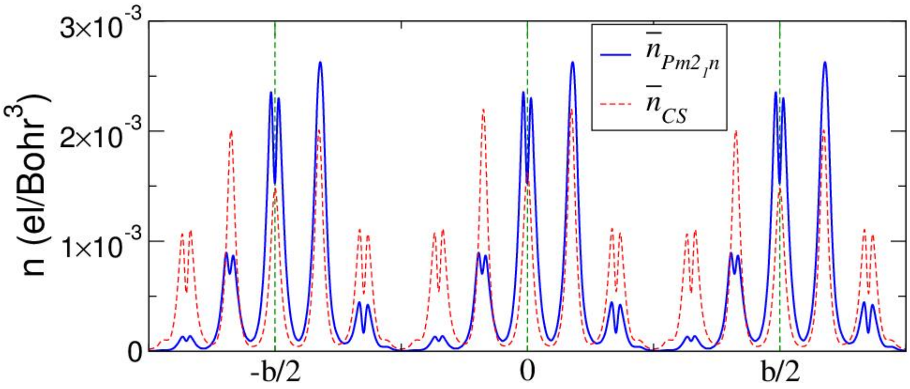

Figure 4.2.: Conduction charge density of Bi-5517, planar-averaged along the stacking direction (b is the lattice constant). $\overline{n}_{Pm2_1n}$ is calculated in the ground-state non-CS $Pm2_1n$ structure; $\overline{n}_{CS}$ is calculated in a fictitious CS system with $Pm2_1n$ cell parameters and $Immm$ atomic positions. The density is interpolated on a very dense grid to reduce real-space integration errors.

cm^{-3}. The Fermi energy (E_F) crosses the Ti $3d$ t_{2g} band manifold approximately 0.4 eV above the conduction band bottom (CBB). The near-CBB DOS shows that 40% of the conduction charge is confined within the central Ti layer, 25% in the two layers on either side, and only 5% reaches the block-edge Ti layer. The t_{2g} CBB is split (see Fig. 4.3B) into d_{yz} (rising in energy due to reduced hopping along the stacking and its lobes being orthogonal to the stacking plane) and d_{xy}/d_{xz} states (the hopping along x being unchanged by the stacking). In turn, d_{xy} and d_{xz} are also split; only d_{xy} has significant DOS below E_F in one of the 5-layer blocks, and only d_{xz} in the other, clearly signaling orbital ordering in the $Pm2_1n$ phase. Fig. 4.3(c) highlights the anisotropy of the conduction bands of $Pm2_1n$ Bi-5517. The two occupied bands per block are doubled, there being two blocks in the supercell; yet, the splitting due to inter-block coupling is negligible, confirming good confinement within each block. The inset of Fig. 4.3(c) shows that the bands in Γ-Y are completely flat, with no band crossing E_F; hence, along this path in the Brillouin zone the system is gapped. Figs. 4.4(a) and (b) show the Fermi surface. The lowest-energy S_1 consists of two disconnected parallel sheets, while the higher S_2 band contributes an elliptic tube. Along Γ-Y (the b or stacking direction), the FS is very flat and resistivity should be high; along Γ-X (the a in-

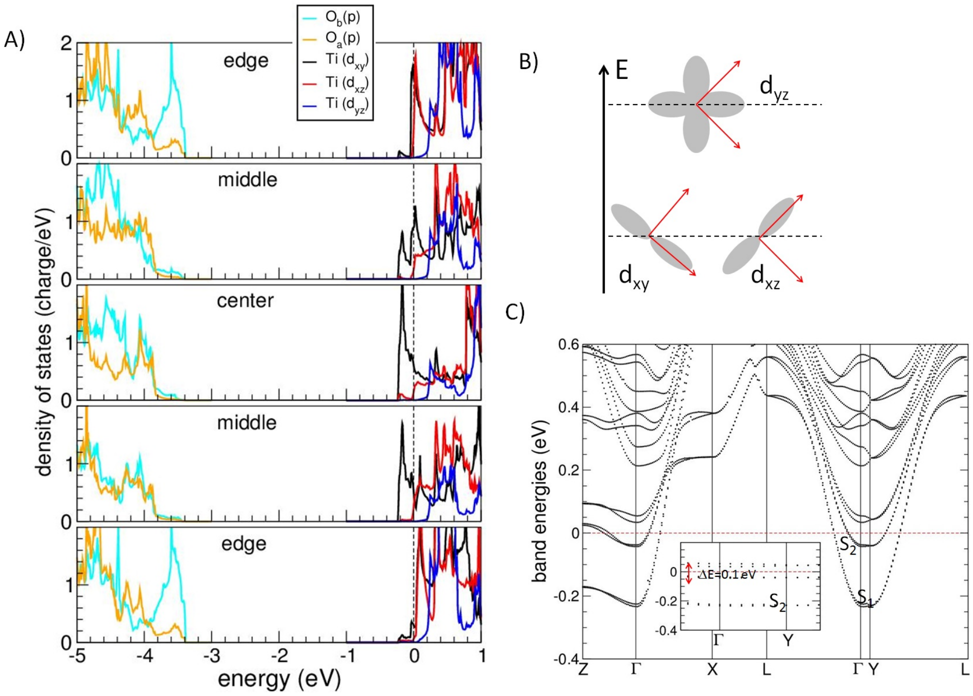

Figure 4.3.: (a): orbital- and atom-resolved DOS of $Pm2_1n$ Bi-5517. The five panels correspond to the five Ti layers in one block. O_a is in the TiO (011) planes, O_b in the intermediate planes (apical to Ti). (b): schematic energy splitting of the t_{2g} orbitals. Cartesian x, y, z refer to the elemental perovskite cubic cell, 45°-rotated in the (y,z) plane with respect to the (**b**, **c**) supercell axes. (c): conduction band structure; inset: zoom along Γ-Y. S_1 and S_2 label the two occupied conduction bands. ΔE is the gap along Γ-Y for k_x=0.

plane direction) the light-mass S_2 contributes to mobility, while S_1 is disconnected. Finally, along Γ-Z (the c direction) both sections contribute, but are expected to yield low conductivity as they have much larger mass than along Γ-X. Indeed, the resistivity (Fig. 4.4(c)) is largest along b (stacking direction), a half order of magnitude lower along c, and another nearly two orders of magnitude lower along the a axis (i.e. along octahedral apical bonds), so the conductivity is largely, though not strictly, one-dimensional. The ordering of the conductivities is quite consistent with experiments [207] for $Pmnn$ La-5517. Interestingly, as Fig.4.4(d) shows, a weak insulating upturn similar to La-5517 is reproduced inserting "defect-like" small activation energies in the conductivity model.

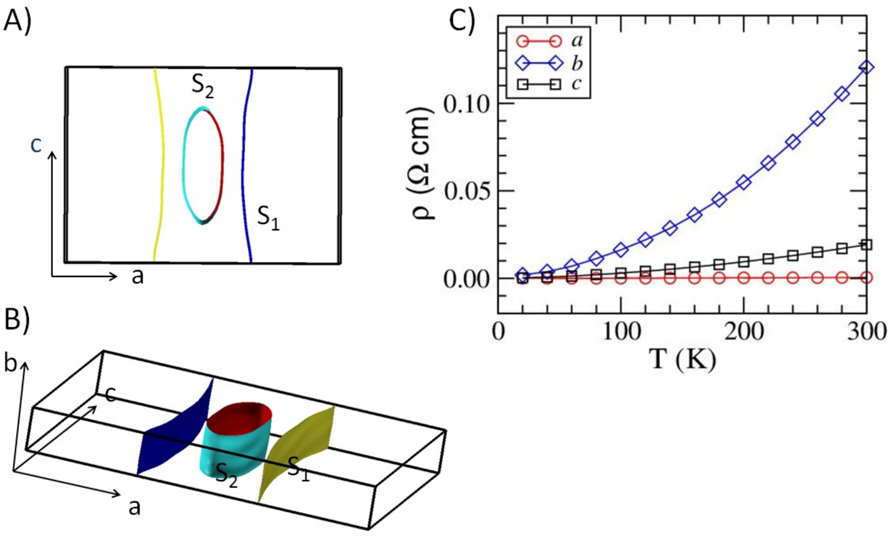

Figure 4.4.: Top (a) and 3D (b) views of the Fermi surface of $Pm2_1n$ Bi-5517. S_1 and S_2 are the occupied conduction bands of Fig. 4.3(c). (c): calculated resistivity along the 3 supercell axes.

4.5. Depolarizing field

We now undertake the assessment of the depolarizing field in a finite Bi-5517 sample. This is far from trivial for several reasons. Even in insulating ferroelectrics, in a slab in vacuum in periodic boundary conditions, the depolarizing field itself may be sufficient to kill ferroelectricity. We verified that this occurs for $PbTiO_3$, using a slab containing 4 Ti (total volume about 450 Å^3 including vacuum). If all the bulk polarization charge is 0.8 C/m^2 amassed at the surface of the slab (i.e. for no screening from the material), it would generate a field of 90 GV/m, i.e. a field energy of over 100 eV per simulation cell. We first keep the ions clamped in the ferroelectrically-distorted configuration, and evaluate the pure electronic response; the field is reduced to 5 GV/m, implying an effective electronic dielectric constant of order 18, and the field energy goes down to 0.3 eV. As the ferroelectric well depth of $PbTiO_3$ is about 0.08-0.1 eV, one expects that his excess energy may be sufficient to kill ferroelectricity. Indeed, relaxing the ions, we recover the paraelectric geometry. We estimate (see also below) that this will not apply to our Bi-5517 material. The bare field expected from ΔP is 37 GV/m with a field

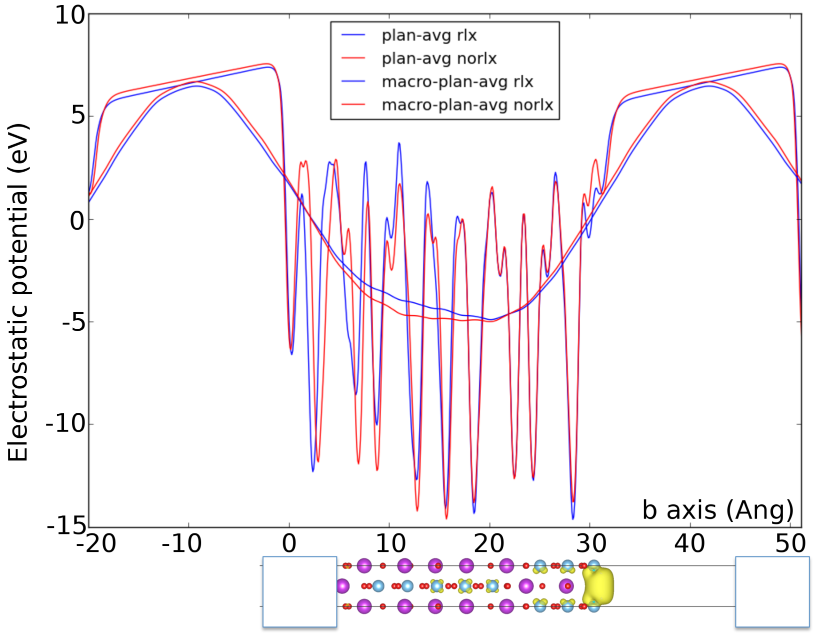

Figure 4.5.: Planar and macrocopic average of the local potential for a Bi-5517 slab in vacuum. A 3D view of the conduction charge is also shown. The large depolarizing field is a signature of ferroelectrics, indicating that the surface polarization charge largely survives the metallic screening due to the conduction charge rushing to the right side to screen the positive polarization charge.

energy in the slab of 51 eV. However, the screened field (in a specific instance to be discussed shortly) goes down to 0.6 GV/m, with a field energy of 0.02 eV. From the energy differences discussed earlier, the energy to destabilize the cell to a paraelectric state is 0.21 eV. So we are still comfortably on the ferroelectric-stable side. The next issue is the slab termination. A side product of the $PbTiO_3$ calculation above is that we verified that both the symmetrically-terminated (BaO surfaces on both sides) and asymmetrically-terminated (BaO and TiO_2 termination respectively) slabs have essentially the same depolarizing field. This need not, however, necessarily apply to our system, given the presence of free charge. Starting with symmetric surface-terminated slabs, we observe that a symmetric slab obtained from the bulk just adding vacuum above and below the primitive cell has essentialy zero residual field in the vacuum (which would imply, due to periodic boundary conditions, that the slab has a macroscopic dipole); also, relaxations seem to largely remove the central Bi displacements. This is a token of conduction charge screening: it turns out that conduction charge is bound into surface states at the upper and lower surfaces. Adopting a different, somewhat unrealistic, asymmetric termination with a $\mathrm{TiO_2}$ layer on one side and a BiO on the other, leads to a large field. The planar and macroscopic averages of the local potential along the *b* axis of a supercell containing a ℓ_{slab}=31 Å Bi-5517 slab and ℓ_{vac}=20 Å of vacuum, with polarization pointing from left to right are shown in Fig.4.5. Due to periodic boundary conditions, there is a finite field $\mathrm{E_{slab}}$ in the interior of the slab, and a field $\mathrm{E_{vac}}$ in vacuum. The effective field in the material, obtained either from the region of linear potential or from $\mathrm{E_{slab}}/\ell_{\mathrm{bulk}}=\mathrm{E_{vac}}\ell_{\mathrm{vac}}$, is around 18 MV/cm. Unfortunately, the observed screened field results from conduction charge moving to surface states on the Ti-terminated surface, rather than from screened polarization. Such charge at the surface naturally produces a field in the slab and vacuum. Besides the behavior of the symmetrically-terminated surface slab, a very strong support for the surface origin of the field in the case discussed is provided by a calculation in yet another surface termination, whereby we find a field *opposite* to that expected from polarization.

4.6. BTO/BZO superlattice

In view of the above negative results for the surface-terminated slab, we turn to a different simulational device. To prevent termination effects from adulterating the effects intrinsic to BTO, we use a superlattice of alternating BTO (one primitive cell, ℓ_{BTO}=≃31 Å) and $\mathrm{Bi_2Zr_2O_7}$ (BZO, one primitive cell, $\ell_{\mathrm{BZO}}\simeq$27 Å). Although we find it to be ferroelectric with $\mathrm{P}||c$ when relaxed in $Cmc2_1$ symmetry, BZO is kept here in the paraelectric $Cmcm$ structure. In this setting, BZO is an unpolarized cladding layer providing seamless stoichiometric continuity on the A cation site. This setting virtually eliminates the possibility of extrinsic surface- or interface-state related fields. BZO also provides effective confinement of the conduction electrons within BTO: examining the locally-projected DOS, we find that the BTO/BZO conduction band offset is about 2 eV. Unfortunately, despite a variety of attempts (including e.g. the application of external electric fields to nudge the system into a polarized state) we find that no residual field survives in pure BTO. A posteriori, this is unsurprising. Let us imagine that conduction charge (and compensating ions) is removed. The bare polarization field is then 45 GV/m (from only ionic and valence contributions). Ions and valence electrons will screen this field with their dielectric response; assumin a dielectric constant of 50, the screened field is 0.9 GV/m. Now let us reinstate the conduction electrons in the cell; even in the bulk, they counter the spontaneous P (see Table 4.2) with a contribution of around –7 μC/m^2; this alone gives a counter-field of 0.9 GV/m. Indeed the conduction charge hardly needs to rearrange at all to screen out the residual field in the superlattice. The difference of conduction densities in the bulk and superlattice integrates to nearly zero, and has practically no dipole.

4.7. Doping: residual field and switching

We thus went on to ascertain whether a field would survive a smaller but still fully metallic conduction density. To this end, we resort to Ca (i.e. hole) doping on the Bi site. We study $CaBi_9Ti_{10}O_{34}$ (CBTO below), i.e. BTO with one Ca per primitive cell, in the same supercell setting with BZO as before. The conduction density is now 1 electron/primitive cell or 1.5×10^{21} cm^{-3}, so the Fermi level is well into the conduction band. It turns out that this density reduction is sufficient to preserve a finite, and in fact fully developed, depolarizing field in the superlattice. The single conduction electron per cell is now mostly located in the block on the right of the cell, i.e. at the positive end of the bare P vector, and is unable to screen out P out entirely. This can be seen in Fig.4.6, which displays the conduction charge superimposed on the macroscopic average of the potential (including the interface offset; see SM). As Fig.4.5 shows, the final field in CBTO is a quite respectable $E_{\rm dep}$=0.6 GV/m after self-consistency and ionic relaxation. Assuming the same bare field as in BTO, from simple electrostatics (e.g. [219], Eq.3) one can estimate the total effective dielectric constant of CBTO at about 65; this matches reasonably the typical static dielectric constants of about 50 in $La_2Ti_2O_7$, the closest insulating materials for which data are available. Also, it suggests a modest counteraction of the conduction electrons as in the undoped BTO case. As already mentioned earlier on this amounts to a 20 meV field energy, which

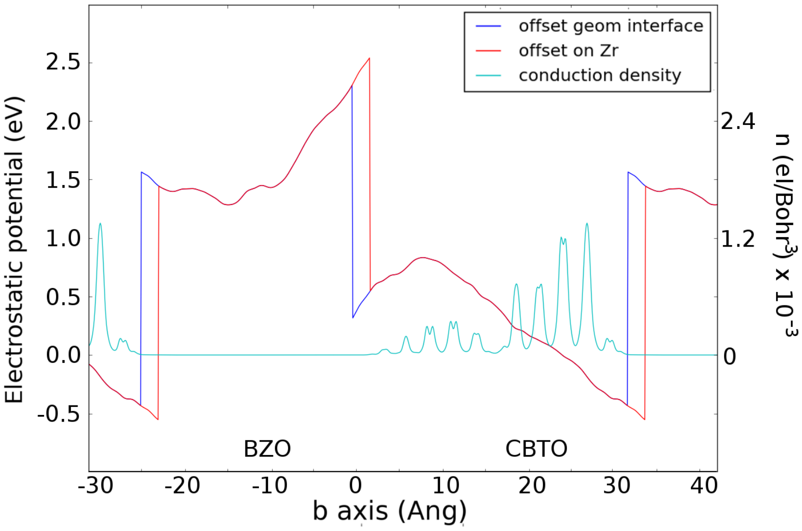

Figure 4.6.: Filter-averaged local potential and conduction charge of the CBTO/BZO superlattice. The large field is a ferroelectricity signature.

cannot affect ferroelectric polarization. The corresponding potential drop across the BTO cell portion is now smaller than the GGA gap, i.e. there is no overlap of the Fermi level on the valence band, and hence no attendant charge transfer. Therefore, all the field we observe in Fig.4.6 is a product of screened spontaneous polarization. As long as CBTO is sandwiched between cladding dielectric layers as in the present setting, the switching of the depolarizing field is straightforward and uneventful. *Thus, CBTO satisfies all the requirements of a proper ferroelectric, and as shown earlier, those of a metal as well. This qualifies CBTO as a genuine native ferroelectric metal.* If CBTO were to have direct metal contacts, a current flow is expected (zero-voltage screening at electrode interfaces is known to be insignificant; see e.g. Ref. [103]). As the voltage to be applied cannot exceed E_{gap}, the current density will never exceed that due to the present field, i.e. j=E_{dep}/ρ. The energy provided by the external voltage source acts to switch the polarization as well as to make current flow. The two processes have an associated energy density, respectively, equal to E dP/dt and Ej. The polarization current can be estimated assuming that P switching occurs in 10 psec (relatively quickly). Then, the ratio of the polarization to the current term of the energy density is about 10^{-2}. It is thus probably likely that conditions leading to current flow will produce enough energy to reverse P as well, were it only as a fluctuation.

4.8. Conclusions

In conclusion, we have designed a novel Bi-based layered-perovskite titanate where native metallicity, specifically in the form of a conductive low-dimensional electron gas, coexists with native ferroelectric polarization. The polarization develops in the $Pm2_1n$ ground state due to a Bi off-center displacement. A switchable depolarizing field exists in a finite Bi-5517 slab upon a moderate amount of Ca doping. Besides its high conceptual significance, our finding opens interesting perspectives for the innovative active elements where charge confinement, current flow, and ferroelectric polarization are integrated in the same material.

Part II.

Beyond DFT with *pseudo*-SIC method

5. Background

5.1. Pseudo-self-interacion correction approach

5.1.1. Self-interaction problem

The Density Functional Theory (DFT) in the Kohn-Sham (KS) formulation, along with the local spin density (LSDA) (or generalized gradient) approximation, describe quasiparticle, namely interacting particle renormalized to independent particle in an effective potential. We have to keep in mind two main concept of this description: first, it includes correlation between particles due to Coulomb repulsion, actually it is overestimated; second, its “band” feature does not limit the particles interactions description; third, all states are defined as Bloch states with a certain grade of “localization” depending on their norm confinement. Based on these considerations, KS-LSDA scheme should manage to describe strongly correlated systems requiring a simultaneous treatment of delocalized and localized states and their mutual interactions. However, standard KS-LSDA does often fail in situations involving strong localization and predominant on-site interactions.

In the following, we will summarize the thesis of the paper [56], which is the basement of the “pseudo-self-interaction correction” method. Briefly, they identify the incomplete cancellation of Hartree (classical electrostatic) and exchange energies in the LSDA energy functional as the first major difficulty of KS-LSDA. This lead to an undesired nonphysical contribution, the self-interaction (SI), which may be minor, and effectively insignificant, for delocalized states, but it is important for highly localized states, leading to serious errors and sometimes qualitative failures.

The pseudo-self-interaction-correction (pSIC) method is a KS-LSDA approach in which the LSDA approximation is supplemented by a potential which removes the SI for all states with nonzero orbital occupation. The pSIC method is thus configured as a practical extension of LSDA, aimed at including strongly correlated materials in the treatment, but without loosing the precious simplicity of LSDA which largely derives from its local density-dependent form of electron (i.e. Hartree plus exchange-correlation) energy $E_{hxc}[n(r)]$, and single-particle effective potential $V_{hxc}[n(r)]$. Since the pSIC is not a radical departure from LSDA, it still offers its invaluable ability to calculate a vast array of properties for large systems (several hundreds atoms), limiting the computational cost at minimum. This is likely the most valuable feature of pSIC, making it different from the majority of other approaches that treat strong electron correlation from a first-principles perspective.

However, starting from LSDA and its local dependence on the one-particle electron density bears a serious downturn, namely the necessary inclusion of the interaction of a particle with its self-generated potential that it is labelled as SI. Employing the Janak formulation [58] to express quantitatively the SI, starting from the expression for the local screening potential:

$$V_{hxc}(\mathbf{r}) = \sum_{i=1}^{N-1} \int d\mathbf{r}' \frac{|\psi_i(\mathbf{r}')|^2}{|\mathbf{r}-\mathbf{r}'|} + V_{xc}\left[n(\mathbf{r})\right] - V_{xc}\left[n_N(\mathbf{r})\right]$$

$$+ f_N \int d\mathbf{r}' \frac{|\psi_N(\mathbf{r}')|^2}{|\mathbf{r}-\mathbf{r}'|} + V_{xc}\left[n_N(\mathbf{r})\right], \tag{5.1}$$

where the third and fourth term on the right hand accounts for Hartree and exchange-correlation SI contributions of the Nth particle, and $n_N(\mathbf{r}) = f_N|\psi_N(\mathbf{r})|^2$ is the charge density and f_N the orbital occupation of the same particle. The Hartree SI is dominant, and has a linear dependence on f_N, while in LSDA $V_{xc}[n_N(\mathbf{r})] \sim n_N^{1/3}$.

It is worth to point out that this is definitely not the only, but surely the most immediately recognizable shortcoming of the LSDA potential, and its most apparent point of departure from the exact, unknown Kohn-Sham potential.

As we said, because of locality of potential, local exchange is significantly smaller than the diagonal part of the Hartree potential, and this results in a substantial SI contribution being left uncancelled, and LSDA eigenvalues depart from the measured electronic removal energies. This departure is strongly limited eliminating the SI following the recipe of Perdew and Zunger [59] (PZ) that for free atoms recovers a very good agreement between eigenvalues and photoemission data. The so called PZ-SIC procedure simply subtracts the SI energy from the total LSDA energy functional E^{LSDA}as follows:

$$E^{SIC}[n] = E^{LSDA} - \sum_i \left(E_h[n_i] + E_{xc}^{LSDA}[n_i] \right), \tag{5.2}$$

where i represent all atomic quantum numbers, and the (spin-polarization dependent) exchange-correlation energy is referred to the fully polarized state. From this functional, applying the usual Kohn-Sham minimization procedure, an 'almost' SI-free single-particle equation for particle i results

$$V^{SIC}[n, n_i] = V^{LSDA}[n] - V_h[n_i] - V_{xc}^{LSDA}[n_i]. \tag{5.3}$$

Here we point out an important detail: the explicit dependence of V^{SIC} on the charge density of state i. The SIC potential is thus orbital-dependent. This characteristics does not imply any serious consequence for free atoms, but it becomes crucial for extended states, making difficult the removal of SI in those systems. Indeed, the majority of interesting (especially strongly correlated) materials are are characterized by a mixture of localized and hybridized valence charge, so that the presence and the relevance of SI cannot be a priori ruled out and should be evaluated case-by-case. As we said, the SI effect strongly depends on electron localization: in the strong localization limit, the Hartree term is dominant over local exchange, whereas in weak localization limit the first term is almost balanced by the second, reducing the SI error. Moreover, orbital character is another important discriminant between low-SI and high-SI states. Typically, highly-localized d and f, and to a lesser extent, radially nodeless 2p electrons are high-SI, rather independently on the specific surrounding chemical environment. A good example of the SI dependence from the occupation of states is that of wide-gap semiconductor such as ZnO and GaN. These systems have a fully occupied d states that in LSDA calculations stay 3 eV higher in energy then the corresponding excitation energies. The agreement is recovered in within LSDA itself reducing the occupation of those states to one-half. This empirical criterion known as Slater's rule, can in fact explained by the presence of SI.

This concept of SI depending on occupation remains valid in extended systems, but a radical change occurs, if we move to a Bloch view where electron charge spreads throughout the system and cannot be uniquely assigned to a specific ionic center. Finding a viable and quantitative interpretation of charge localization in extended systems is thus a strict condition to the introduction a practically quantifiable and physically sound notion of SI.

Wide literature about the diverse and practically valuable strategies implemented exist: the PZ-SIC (sometime referred to as LSDA-SIC in literature) directly subtract from the energy functional the LSDA SI of the single-particle state, as illustrated by equations (5.2,5.3). This formulation has been practically implemented in the LMTO (linear-muffin-tin orbital) basis, as well as in the ASA (atomic sphere approximation) . A formally alternative is, though substantially equivalent, the PZ-SIC approach exploiting the properties of the Wannier functions. For details about these different approaches, see references inside [56]. Briefly, in PZ-SIC the necessary requirement to define a non-vanishing SI is assuming fully localized, thus non-Bloch like, solutions for the SIC Hamiltonian. Though this is perfectly legitimate in principle, however, abandoning Bloch's theorem and translational symmetry in favor of localized states may give rise to very serious complicancies at both the methodological and interpretative level. Moreover, apart from differences due to specific implementations, in general the PZ-SIC seem to have an strong tendency to charge localization, which causes a large overcorrection of single-particle energies with respect to their LSDA energies.

In 1996 Vogel, Kruger, and Pollmann [60] (VKP) introduced a radically simplified procedure to parametrize the SI in terms of atomic counterparts and extract it from the band energy of wide-gap insulators. In this strategy the Bloch-state view is fully conserved, and it is assumed that some degree of localization, and then an 'effective' SI, is present in the Bloch states, and must be removed. The procedure is based on pseudopotential (PP) formalism modified to include the angular moment-dependent atomic SI within each PP projector and make it SI-free by construction:

$$V_l^{pSIC}(r) = V_l^{PS}(r) - V_H[n_l(r)] - V_{xc}^{LSD}[n_l(r)],$$

where V_l^{PS} is the usual ion-core PP (minus a long-range local part which is customarily subtracted and treated separately), and the second and third terms are the SI atomic part for angular moment l (assuming radial symmetry, so that only l-dependence survives), and $n_l = |\phi_l|^2$ the corresponding atomic charge. The PP projector acting on Bloch states is then written in the usual fully-separable Kleinman-Bylander (KB) form

$$\hat{V}^{pSIC} = \sum_l \frac{\left|V_l^{pSIC}\phi_l\right\rangle \left\langle \phi_l V_l^{pSIC}\right|}{\left\langle \phi_l \left| V_l^{pSIC} \right| \phi_l \right\rangle}. \tag{5.4}$$

This procedure had satisfying results for a series of wide-gap insulators and especially for the fairly ionic II-VI compounds. The success of this approach is comprehensible observing the case of bulk ZnO. There, each group of valence bands have a rather well defined atomic-angular character, and each of them (Zn 3s, 3p, 3d, and O 2s, 2p) is corrected by its own atomic SI, according to equation (5.4). While this turns out to be a good assumption for II-VI wide-gap insulators, in general it is not. This is because the bands that have predominant angular character suffer from a reduced SI than the corresponding orbitals in the free atom, mainly for three reasons: first, charge spreading, especially dominant in covalent or metallic bonding, largely dilutes the effects of SI. Second, hybridization among different atomic states is more likely than bands characterized by a sharp orbital character. Third, in the pSIC scheme in equation (5.4) highly localized (e.g. Zn 3d, O 2s), moderately localized (O 2p) and weakly localized (Zn 3s, 3p) bands are all corrected by the full atomic SI, even if they are not occupied. This is the key aspect of VKP scheme success, but it is also a questionable aspect, since the SI should vanish for empty states. Based on these considerations, the applicability of the VKP pSIC approach is limited to a very restricted number of cases and a suitable generalization of the formalism is needed, in order to overcome a good portion of these shortcomings, and defining an efficient and generally applicable band theory approach for strongly correlated materials.

5.1.2. The essence of pSIC

In the following, we will see the basic concepts of the pseudo-SIC method as developed by Filippetti and Spaldin [57], starting from the idea of the VKP approach seen before. Basically they formulate an approach that extends the applicability of pSIC to a large variety of cases. The key concepts at the basis of this generalization could be summarized as:

- an atomic SI projector is a generally valid form even outside the PP formalism and can be built and exploited in a single-particle scheme, but
- the SI projector cannot be purely atomic. It must depend on the specific chemical environment to simulate the charge distribution of the real system in effective way;
- the latter dependence should conserve the virtues of LSDA: state-independence, locality of the effective single-particle potential, and invariance under unitary transformation of the eigenstates;
- as in the ordinary PP formalism, the SIC projector must be transferable, unique and fixed once for all for any given atomic species.

Based on these principles, they proposed a pSIC projector similar to Kleinman-Bylander (KB) form [61],

$$\hat{V}^{\sigma}_{SIC} = \sum_i \frac{|\gamma^{\sigma}_i\rangle \langle\gamma^{\sigma}_i|}{C^{\sigma}_i}, \tag{5.5}$$

where

$$\gamma^{\sigma}_i(\mathbf{r}) = V^{\sigma}_{HXC}\left[n^{\sigma}_i(\mathbf{r})\right]\phi_i(\mathbf{r})$$

is the usual KB projection function, but now V^{σ}_{HXC} is in place of the usual PP potential, and

$$C^{\sigma}_i = \langle\phi_i|\, V^{\sigma}_{HXC}\left[n^{\sigma}_i\right] |\phi_i\rangle$$

the normalization factor of the KB PP. The Kohn-Sham pSIC equations then become

$$\left[-\nabla^2 + \hat{V}_{PP} + \hat{V}^{\sigma}_{HXC} - \hat{V}^{\sigma}_{SIC}\right] |\psi^{\sigma}_{n\mathbf{k}}\rangle = \epsilon^{\sigma}_{n\mathbf{k}} |\psi^{\sigma}_{n\mathbf{k}}\rangle\,,$$

where V_{PP} is the ordinary PP projector, replaced, where possible, by the nuclear potential in an all-electron scheme, and $\epsilon^{\sigma}_{n\mathbf{k}}$ and $\psi^{\sigma}_{n\mathbf{k}}$ the Kohn-Sham eigenvalues and eigenfunctions.

In the VKP approach, $V^{\sigma}_{HXC}\left[n^{\sigma}_{i}\right]$ is simply the i-state atomic potential at full occupation. Filippetti and Spaldin proposed a simple but effective way to introduce in $V^{\sigma}_{HXC}\left[n^{\sigma}_{i}\right]$ the dependence on the true chemical environment, i.e. writing $n^{\sigma}_{i}(\mathbf{r}) = p^{\sigma}_{i}\left|\phi_i(\mathbf{r})\right|^2$: ϕ_i is still the atomic orbital, but its weight into the density is determined by an effective occupation number p_i (analogous to the Janak fractional occupation number in free atoms f_i, Eq. (5.1) of previous section). In the extended system case, it is possible to calculate it in self-consistent way as atomic orbital projection onto the manifold of the occupied Bloch states:

$$p^{\sigma}_{i} = \sum_{n\mathbf{k}} f^{\sigma}_{n\mathbf{k}} \left\langle \psi^{\sigma}_{n\mathbf{k}} \middle| \phi_i \right\rangle \left\langle \phi_i \middle| \psi^{\sigma}_{n\mathbf{k}} \right\rangle , \tag{5.6}$$

where the $f^{\sigma}_{n\mathbf{k}}$ are Fermi occupation numbers. This expression has two important advantages. First, the treatment to insulators and metals alike is easily generalized. Second, it introduces an intuitive, automatic scaling of the amount of SI attributed to each Bloch state according to its atomic character. Indeed, it has two limits: in the lower $p^{\sigma}_{i} = 0$ (unoccupied state), the pSIC correction vanishes and the Kohn-Sham equations reduce to that of the ordinary LSDA; in the upper $p^{\sigma}_{i} = 1$, the pSIC correction is fully atomic-like. In other words, the p^{σ}_{i} have the important role of charge localization parameters for the Bloch states, in the sense we have seen before. Notice that since they do not depend on each individual Bloch state $(n, \mathbf{k})$ they represent an average localization measure, avoiding the downturns of the PZ-SIC.

However, the introduction of p^{σ}_{i} bears a problem: it requires the recalculation of $V^{\sigma}_{HXC}\left[n^{\sigma}_{i}\right]$ at each self-consistency iteration for each atom and angular component, resulting in an increased computational cost with respect to the plain LSDA scheme, especially for large-size systems. To avoid this problem, the potential $V^{\sigma}_{HXC}\left[n^{\sigma}_{i}\right]$ has been expressed as a parametric function of the orbital occupations, that in linear approximation becomes

$$V^{\sigma}_{HXC}\left[n^{\sigma}_{i}\right] = \alpha\, p^{\sigma}_{i}\, V^{\sigma}_{HXC}\left[\left|\phi_i\right|^2\right] ,$$

where α is a relaxation coefficient always set equal to 1/2 (for more insightful discussion on the role of this coefficient we refer to [56]). In this way $V^{\sigma}_{HXC}\left[|\phi_i|^2\right] = V^{\sigma}_{HXC}\left[n^{\sigma}_i; p^{\sigma}_i = 1\right]$, namely the atomic SI potential for the fully occupied orbital is set in the initialization procedure, while only p^{σ}_i is recalculated during the self-consistency cycle.

The atomic SIC potential is further approximated in reference [57] by its radial counterpart, introducing atomic quantum numbers l, m_l and the atomic label ν, and become:

$$V_{HXC}\left[n^{\sigma}_{\nu,l,m_l}(\mathbf{r})\right] = \alpha\, p^{\sigma}_{\nu,l,m_l}\, V_{HXC}\left[n_{\nu,l}(\mathbf{r}); 1\right], \tag{5.7}$$

where $n_{\nu,l}(r)$ is the radial pseudo-charge density of orbital $(l, m_l\ )$. Substituting this expression in equation (5.5), the pSIC projector can be rewritten, in covariant form, as

$$V^{\sigma}_{SIC} = \sum_{\nu,l,m_l,m'_l} \frac{\left|\gamma_{\nu,l,m_l}\right\rangle \alpha\, p^{\sigma}_{\nu,l,m_l,m'_l} \left\langle\gamma_{\nu,l,m'_l}\right|}{C_{\nu,l,m_l,m'_l}}, \tag{5.8}$$

with the projectors

$$\gamma_{\nu,l,m_l}(\mathbf{r}) = V_{HXC}\left[n_{\nu,l}(\mathbf{r}); 1\right] \phi_{\nu,l,m_l}(\mathbf{r}).$$

The normalization coefficients

$$C_{\nu,l,m_l,m'_l} = \int d\mathbf{r}\, \phi_{\nu,l,m_l}(\mathbf{r}) V_{HXC}\left[n_{\nu,l}(\mathbf{r}); 1\right] \phi_{\nu,l,m'_l}(\mathbf{r}), \tag{5.9}$$

are purely atomic and can be set as in the ordinary KB PP formalism, while all the dependence on the specific environment is contained in the orbital occupation numbers. The equation 5.8 contains in essence all the key ingredients of the pSIC approach.

The following section is dedicated to the generalization to the Vanderbilt ultrasoft PP scheme (USPP) [212] whereby this method is actually implemented. Before concluding this section, we comment the Figure 5.1, in which the effect of pSIC is exemplified in four different case with different weight of correlation: Al as a simple metal, Si as a covalent semiconductor, ZnO as a ionic insulator, and CuO

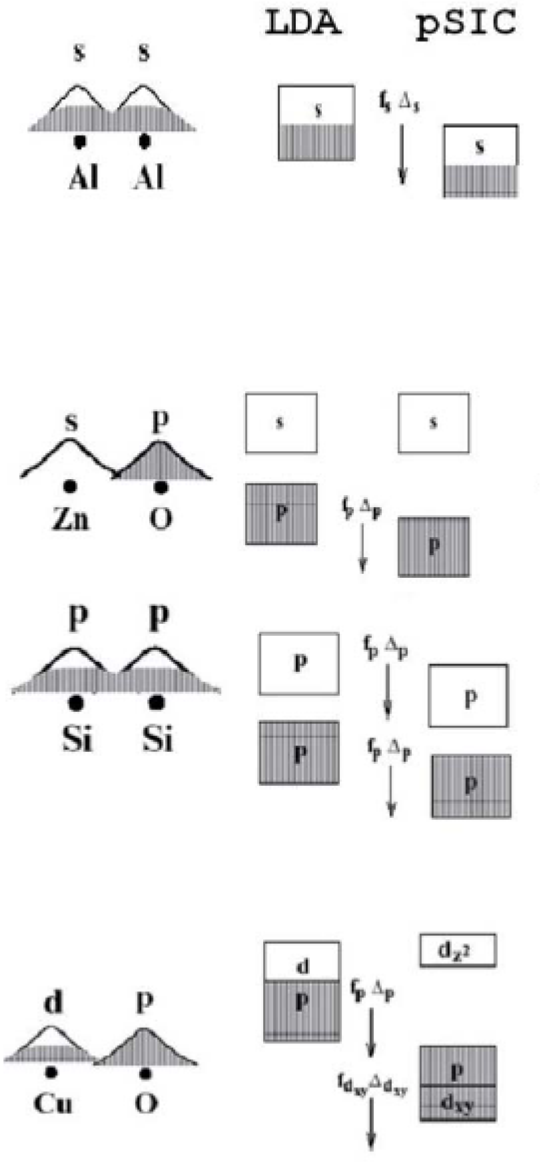

Figure 5.1.: Schematic picture from [56] that shows the effect of self-interaction removal in different types of materials: from the top, a metal (Al), a wide-gap (ZnO) and a narrow gap (bulk Si) semiconductor, a correlated insulator (CuO).

as a Mott insulator.

In the case of Al, since its half-filled band around E_F is constitute of Bloch states having the same orbital character, $\hat{V}^{\sigma}_{SIC}$ shifts down with the same energy all these states, and we do not observe any effects and thus any differences with standard LDSA band structure. For Si, valence and conduction bands, while obviously separated by the energy gap, have a substantially similar orbital character, namely a sp^3 hybridized states, on average over all k-points. For occupied valence states the SIC is small, basically because they are rather delocalized. Thus the pSIC and LSDA band structures are much similar, and the gap error is only partially corrected: the indirect gap changes from 0.4 eV in LSDA to 0.7 eV in pSIC, still much smaller than the experimental 1.17 eV. This might seem disappointing, but actually for gap assessing of covalent semiconductors, the problem stem from the DFT method itself.

Now we consider more interesting ZnO case. The key point is that in this prototypical wide-gap insulator the valence and conduction manifolds have significantly different orbital character [63]. Hence, the fully occupied valence O $2s$, $2p$ and Zn $3d$ bands are downshifted by an amount close to their atomic SIC counterparts, while conduction Zn $3s$, 3p bands remain nearly unchanged. As a result, the pSIC description shows a largely increased energy gap and appreciably downshifted Zn $3d$ bands. Finally, CuO illustrates how the pSIC approach works for Mott insulators: in LSDA no energy gap opens and the system is (erroneously) metallic and non magnetic, with E_F cutting near the top of the hybridized O $2p$-Cu $3d$ band manifold. Within pSIC, the filled O $2p$ and Cu $3d$ bands are downshifted in energy, except for one band per Cu corresponding to the only unoccupied state (orbital character d_{z^2} in the picture) which remains unchanged, so that a fundamental gap opens up, and the correct insulating spin-polarized ground state is restored.

We refer the reader to the paper [56] for a review of recent applications demonstrating the usefulness and accuracy of the pSIC method.

5.1.3. pSIC-USPP formulation

In this section, I reproduce the pSIC-USPP formulation as presented in [56].

The PP approach is a methodological milestone in the application of first-principles calculations to realistic, large-size systems. While originally confined to the study of covalent semiconductors and metals using plane-waves basis set, nowadays the PP technique is considered reliable and efficient for any material, and implemented in most codes. This is helpful for the implementation of pSIC, whose basic ingredients closely mirror those of the ordinary PP techniques. Some complication in the pSIC formalism is introduced, however, in the case of USPP, which release the norm-conservation condition on the pseudo wavefunctions by freezing-in part of the valence charge close to the ion-core. In this way, the pseudo wavefunctions and the respective PP can be very smooth (i.e. 'ultrasoft'), and expressed in plane-waves basis with a formidable saving of computing cost. The USPP is a key ingredient of plane-waves basis set implementations, especially for systems with localized charge, and allows the simulation of large-size systems needed e.g. to treat doping in a realistic manner with atomic substitutions in supercell. Thus, we consider the pSIC generalization to USPP an integral part of an efficient and practically viable plane-waves basis implementation. In the USPP approach the electron charge density is

$$n^\sigma(\mathbf{r}) = \sum_{n\mathbf{k},\sigma} f^\sigma_{n\mathbf{k}} \, |\psi^\sigma_{n\mathbf{k}}(\mathbf{r})|^2 + \sum_{n\mathbf{k},\sigma} f^\sigma_{n\mathbf{k}} \sum_{\alpha\alpha'} \langle \psi^\sigma_{n\mathbf{k}} \, | \beta_\alpha \rangle Q_{\alpha\alpha'}(\mathbf{r}) \langle \, \beta_{\alpha'} | \, \psi^\sigma_{n\mathbf{k}} \rangle \, ,$$

where $\alpha = [n, l, m, R]$ and $\alpha = [n', l', m', R]$ are orbital quantum numbers and atomic positions R, and β_α the USPP projector functions. The first term within square brackets is the ultrasoft charge, the second term the 'augmented' charge, i.e. the portion of pseudo valence charge density localized within the atomic core radii, where

$$Q_{\alpha\alpha'}(\mathbf{r}) = \phi^{AE}_\alpha(\mathbf{r})\phi^{AE}_{\alpha'}(\mathbf{r}) - \phi^{PS}_\alpha(\mathbf{r})\phi^{PS}_{\alpha'}(\mathbf{r}),$$

is the 'frozen' atomic augmented charge, obtained as difference between all electron (ϕ^{AE}_α) and pseudo (ϕ^{PS}_α) atomic charges.

The KS equations are generalized as

$$\left[-\nabla^2 + V_{LOC}(\mathbf{r}) + \sum_{\alpha\alpha'} |\beta_\alpha \rangle D^\sigma_{\alpha\alpha'} \langle \, \beta_{\alpha'}| + V^\sigma_{HXC}(\mathbf{r}) \right] \psi^\sigma_{n\mathbf{k}}(\mathbf{r}) = \epsilon^\sigma_{n\mathbf{k}} \hat{S} \psi^\sigma_{n\mathbf{k}}(\mathbf{r}),$$

where $V_{LOC}(\mathbf{r})$ is the long-range local part of the pseudopotential, $D^\sigma_{\alpha\alpha'}$ the non-local part and S the overlap matrix which generalizes the orthonormality condition

$$\hat{S} = 1 + \sum_{\alpha\alpha'} |\beta_\alpha\rangle q_{\alpha\alpha'} \langle\beta_{\alpha'}| \, ,$$

where $q_{\alpha\alpha'}$ are the integrals of the augmented charges $Q_{\alpha\alpha'}(\mathbf{r})$, and $\left\langle \psi^\sigma_{nk} \middle| \hat{S} \middle| \psi^\sigma_{n'k'} \right\rangle = \delta_{n,n'}\delta_{k,k'}$. Finally, the non-local pseudopotential projector is made up of two contributions

$$D^\sigma_{\alpha\alpha'} = \tilde{D}_{\alpha\alpha'} + \int d\mathbf{r} \, \left(V_{LOC}(\mathbf{r}) + V^\sigma_{HXC}(\mathbf{r})\right) Q_{\alpha\alpha'}(\mathbf{r}). \tag{5.10}$$

The first term on the right-hand side of equation 5.10 is the usual Kleinman-Bylander projector, and contributes to the 'bare' pseudopotential (i.e. it is calculated within the atomic reference configuration). The second term is specific to the USPP formalism, and represents the action which the local and screening potentials exert on the augmented charges. Since this term depends on V^σ_{HXC}, it has to be updated during the self-consistency cycle. With USPP, two elements of the pSIC formalism must be appropriately generalized. First, the occupation numbers p^σ_i introduced in equation 5.6 becomes

$$p^\sigma_{\nu,l,m_l,m'_l} = \sum_{n\mathbf{k}} f^\sigma_{n\mathbf{k}} \left\langle \psi^\sigma_{n\mathbf{k}} \middle| \hat{S}\phi_{\nu,l,m_l} \right\rangle \left\langle \phi_{\nu,l,m'_l}\hat{S}^* \middle| \psi^\sigma_{n\mathbf{k}} \right\rangle ,$$

where the overlap matrix S now ensures the correct normalization. Since the non-local part of the USPP depends on the screening potential itself (see Eq. 5.10) it must also be descreened by its SI

$$\hat{V}^\sigma_{AUG-SI} = \sum_{\nu,l,m_l} \sum_{\alpha\alpha'} |\beta_\alpha\rangle \left(\alpha \, p^\sigma_{\nu,l,m_l,m_l} \int d\mathbf{r} \, V^\alpha_{HXC}\left[n_{\nu,l}(r);1\right] Q_{\alpha\alpha'}(\mathbf{r}) \right) \langle\beta_{\alpha'}| \, .$$

This expression, reported in reference [57], is the exact SI (in the sense of the PZ procedure) of the augmented USPP potential, but has the disadvantage of being slightly non-covariant. Actually, an alternative, approximated but covariant form is used [56]. Thus, the KS equations for the pSIC-USPP approach are:

$$\Bigg[-\nabla^2 + \hat{V}_{LOC}(\mathbf{r}) + \sum_{\alpha\alpha'} |\beta_\alpha\rangle D^\sigma_{\alpha\alpha'} \langle\beta_{\alpha'}| + \hat{V}^\sigma_{HXC}(\mathbf{r})$$

$$- \left(\hat{V}^{\sigma}_{SI} + \hat{V}^{\sigma}_{AUG-SI} \right) \Big] \left| \psi^{\sigma}_{n\mathbf{k}} \right\rangle = \epsilon^{\sigma}_{n\mathbf{k}} \hat{S} \left| \psi^{\sigma}_{n\mathbf{k}} \right\rangle ,$$

where $\hat{V}^{\sigma}_{SIC}$ is given by equations (5.5,5.7,5.9).

5.2. Dielectric function

The intent of this section is to remind the relation between the microscopic and macroscopic description of the interaction between a material and the electromagnetic field [64]. While in a macroscopic picture we exploit Maxwell's equations to define macroscopic quantities like absorption, light scattering, reflectivity, that are measurable by spectroscopy experiments, in the microscopic one, we use ideas such as the excitation of an electron as a consequence of the absorption of a photon, or the creation of an electron-hole pair, etc.

Therefore we need a relation ables to link these two distant pictures, namely band structure of a solid, and in particular electronic excited states, with optical properties of solids involved in the experiments. The frequency-dependent dielectric function $\epsilon(\omega)$ plays exactly this central role.

5.2.1. From Maxwell equations to dielectric function

We start from the famous Maxwell's equation in presence of matter:

$$\nabla \times H = \frac{1}{c}\frac{\partial D}{\partial t} + \frac{4\pi}{c}\mathbf{j}_{ext}. \tag{5.11}$$

Complex dielectric function stem from the specification of the constitutive equation $D = D[E, H]$. Indeed, in case of negligible non-linear effect, it is possible to define a linear relation for it that also defines the complex dielectric tensor ε

$$D(\mathbf{r}, t) = \int d\mathbf{r}' \int dt' \varepsilon(\mathbf{r}, \mathbf{r}', t - t') E(\mathbf{r}', t').$$

For our purpose we forget the tensor nature of ε and write it as a function of frequency, having the relation

$$D(\omega) = \epsilon(\omega)E(\omega). \tag{5.12}$$

We remind the important relation $\epsilon(-\omega) = \epsilon^*(\omega)$, that steam from that $D(r,t)$ is real.

Next, we consider the relation that connect the electric field E with its derived field D via polarization P:

$$D = E + 4\pi P, \tag{5.13}$$

and the linear relation between P and the macroscopic electric field E via electric susceptibility:

$$P = \chi_e E, \tag{5.14}$$

and joining them, we have

$$\epsilon = 1 + 4\pi\chi_e. \tag{5.15}$$

Now from Eq. (5.11) and Eq. (5.12), and considering that external sources are zero, $j_{ext} = 0$, we have

$$\nabla \times H(\omega) = -\frac{i\omega\epsilon(\omega)}{c}E(\omega) = -\frac{i\omega}{c}E(\omega) - \frac{i\omega 4\pi}{c}P(\omega)$$

where we have used Eq.s (5.14) and (5.15).

Finally, from the Ohm's law (Eq. (5.12)), we obtain

$$\epsilon = 1 + \frac{4\omega i\sigma}{\omega},$$

which shows the link between the dielectric function ϵ and the conductivity σ of a material.

Without external sources, Maxwell's equation of electric field yields

$$\nabla^2 E = \frac{\mu\varepsilon}{c^2}\frac{\partial E}{\partial t^2}.$$

The general solution of this equation is

$$E = E_0 e^{i(\mathbf{K}\cdot\mathbf{r}-\omega t)}, \tag{5.16}$$

where $|\mathbf{K}|^2 = \frac{\omega^2}{c^2}\mu\varepsilon$. Supposing a propagation along x direction, so $\mathbf{K} = \frac{\omega}{c}\sqrt{\mu\varepsilon}x$, we have

$$E(x,t) = E_0 e^{i\frac{\omega}{c}x\sqrt{\mu\varepsilon}} e^{-i\omega t}.$$

Considering a propagation in vacuum, imposing $\sigma = 0, \mu = \varepsilon = 1$, we have the plane wave solution

$$E(x,t) = E_0 e^{i\omega(\frac{x}{c}-t)}.$$

The solution (5.16) inside a medium of finite conductivity is the damped wave

$$E(x,t) = E_0 e^{i\frac{\omega}{c}x\mathcal{N}} e^{-i\omega t}, \tag{5.17}$$

where we have introduced the complex refractive index $\mathcal{N} = \varepsilon = \nu + i\kappa$.

The refraction index and the extinction coefficient are the real and the imaginary part of $\mathcal{N}$, respectively. They are related to the real ε_1 and the imaginary part ε_2 of ε, through $\varepsilon_1 = \nu^2 - \kappa^2$, $\varepsilon_2 = 2\nu\kappa$ relations, where ν and κ are not independent, since ε_1 and ε_2 are related by the Kramers Kronig relations [68]. Thus, Eq. (5.17) becomes

$$E(x,t) = E_0 e^{i\frac{\omega}{c}x\nu} e^{i\frac{\omega}{c}x\kappa} e^{-i\omega t}.$$

From it, we can define the optical skin depth δ as the distance where the amplitude of the field is reduced by $1/e$,

$$\delta = \frac{c}{\omega\kappa},$$

and the absorption coefficient α as the inverse distance where the intensity of the field (proportional to $|E(x)|^2$) is reduced by $1/e$:

$$\alpha = \frac{2\omega\kappa}{c} = \frac{\omega\varepsilon_2}{\nu c}, \tag{5.18}$$

that gives a linear relation between the absorption coefficient and the imaginary part of the dielectric function. As a reminder, we note that all these quantities are frequency dependent, in the most general case.

5.2.2. Microscopic-Macroscopic connection

Considering a N-electrons system exposed to an electro-magnetic perturbation, its Hamiltonian H_0 changes its kinetic term according to

$$\sum_j \frac{1}{2}\mathbf{p}_j^2 \longrightarrow \sum_j \frac{1}{2}\left(\mathbf{p}_j - \frac{\mathbf{A}(\mathbf{r}_j,t)}{c}\right)^2 ,$$

where $\mathbf{A}$ is the vector potential of the electro-magnetic field in the Coulomb gauge ($\nabla \cdot \mathbf{A} = 0$ and scalar potential $\phi = 0$) and $\mathbf{p}_j - \mathbf{A}(\mathbf{r}_j,t)/c$ can be seen as a generalized velocity v. If we neglect non-linear effects in $1/c$, we can separate Hamiltonian in two parts as $H = H_0 + H_1$ where the second term is the radiation perturbative field

$$H_1 = -\frac{1}{c}\sum_j \mathbf{A}(\mathbf{r}_j,t) \cdot \mathbf{p}_j .$$

This term can be treated within the well known time-dependent perturbation theory, in order to find the transition probability (per unit time), which allows for the absorption of the incoming radiation:

$$P_{i\to f} = 2\pi \left|\langle f \left|\mathbf{A}(\mathbf{r}_j,t) \cdot \mathbf{p}_i\right| i\rangle\right|^2 \delta(E_f - E_i - \omega),$$

where the initial and final states $|i\rangle$, $|j\rangle$ and E_i, E_f are eigenfunctions and eigenvalues of the many-body Hamiltonian H_0, respectively. If now, one specifies the perturbation A

$$\mathbf{A}(\mathbf{r},t) = A_0\hat{\mathbf{e}}e^{i(\mathbf{q}\cdot\mathbf{r}-\omega t)} + c.c.$$

with $\hat{\mathbf{e}}$ is the polarization vector and $\mathbf{q}$ is the wave vector of the radiation, the transition probability becomes

$$P_{i\to f} = 2\pi \left(\frac{A_0}{c}\right)^2 |\hat{\mathbf{e}} \cdot \mathbf{M}_{if}|^2 \delta(E_f - E_i - \omega), \tag{5.19}$$

where $\mathbf{M}_{if} = \langle f \left| e^{i\mathbf{q}\cdot\mathbf{r}}\mathbf{p}\right| i\rangle$.

The absorption coefficient is defined as the energy absorbed in the unit time in the unit volume divided by the flux of energy

$$\alpha(\omega) = \frac{\omega W(\omega)}{u(c/\nu)},$$

where c/ν is the speed of the light in the matter, the average energy density $u = \frac{\nu^2 A_0^2 \omega^2}{2\pi c^2}$ and the number of transition per unit time per unit volume $W(\omega)$ is given by the sum of (5.19) over all possible transitions. Thus, $\alpha(\omega)$ becomes

$$\alpha = \frac{4\pi}{\nu\omega c}^{2} \sum_{ij} |\hat{\mathbf{e}} \cdot \mathbf{M}_{if}|^2 \delta(E_f - E_i - \omega).$$

In the case of solid system, the many-body level i can be substituted by a double index v, k, band and wave vector indices (in the first Brillouin zone) in a single particle picture. In addition, the transmitted momentum q can usually be neglected, since its wavelength in light is very small, around $400 - 700\, nm^{-1}$. Therefore, considering only vertical transitions, i.e. from an occupied state v, k to an empty state c, k, and using reciprocal space to better exploit the translational invariance of an infinite solid, one obtains the imaginary part of the complex dielectric function, ε_2, from the macro absorption coefficient (5.18)

$$\varepsilon_2 = 2\frac{4\pi^2}{\Omega} \lim_{q \to 0} \frac{1}{q^2} \sum_{v,c,\mathbf{k}} \left| \left\langle c\mathbf{k} + \mathbf{q} \left| e^{i\mathbf{q}\cdot\mathbf{r}} \right| v\mathbf{k} \right\rangle \right|^2 \delta(\epsilon_{c\mathbf{k}+\mathbf{q}} - \epsilon_{v\mathbf{k}} - \omega). \qquad (5.20)$$

By using the Kramers-Kronig relations, the expression of the real part $\varepsilon_1(\omega)$ can be obtained. The Eq. (5.20) is particularly important because it represents a connection between the macroscopic optical constants such as absorption index and the microscopic structure of the material, namely the band structure of a solid. We just note that releasing the single particle approximation more complicated relations are needed to describe dielectric function ε_2.

5.2.3. Implementation within *pseudo*-SIC code

The calculation of dielectric function is part of the most of the DFT codes, such as VASP [210] and QuantumESPRESSO [69]. We have ported the routine for computation of $\varepsilon(\omega)$ from this last code, because of its similarity with our in-house code PWSIC that implements the pSIC method. Following the *epsilon.x* man page (see online repository of [69]), we report some detail of how the dielectric tensor is computed.

The imaginary part of the dielectric tensor $\epsilon_2^{\alpha,\beta}(\omega)$ can be viewed as a response function that comes from a perturbation theory with adiabatic turning on:

$$\epsilon^{\alpha,\beta}(\omega) = 1 + \frac{4\pi e^2}{\Omega N_{\mathbf{k}} m^2} \sum_{n,n'} \sum_{\mathbf{k}} \frac{\hat{\mathbf{M}}_{\alpha,\beta}}{(E_{\mathbf{k},n'} - E_{\mathbf{k},n})^2} \cdots$$

$$\cdots \left\{ \frac{f(E_{\mathbf{k},n})}{E_{\mathbf{k},n'} - E_{\mathbf{k},n} + \hbar\omega + i\hbar\Gamma} + \cdots \right.$$

$$\left. \cdots \frac{f(E_{\mathbf{k},n})}{E_{\mathbf{k},n'} - E_{\mathbf{k},n} - \hbar\omega - i\hbar\Gamma} \right\} \tag{5.21}$$

where Γ is the adiabatic parameter and, for the total energy conservation it must tend to zero. This is the way in which the Dirac Delta function appears and this means that every excited state has an infinite lifetime, i.e. is stationary.

$$\epsilon_2^{\alpha,\beta}(\omega) = \frac{4\pi e^2}{\Omega N_{\mathbf{k}} m^2} \sum_{n,n'} \sum_{\mathbf{k}} \frac{\hat{\mathbf{M}}_{\alpha,\beta} f(E_{\mathbf{k},n})}{(E_{\mathbf{k},n'} - E_{\mathbf{k},n})^2} \cdots$$

$$\cdots \Big[\delta(E_{\mathbf{k},n'} - E_{\mathbf{k},n} + \hbar\omega) + \delta(E_{\mathbf{k},n'} - E_{\mathbf{k},n} - \hbar\omega) \Big] \tag{5.22}$$

This situation is nonphysical because the interaction with electromagnetic field (even in the absence of photons, i.e. spontaneous emission) gives an intrinsic broadening to all exited states, hence the lifetime is finite and Γ must be greater than zero. In the limit of small but non vanishing Γ the dielectric tensor turns into the Drude-Lorentz one:

$$\epsilon_2^{\alpha,\beta}(\omega) = \frac{4\pi e^2}{\Omega N_{\mathbf{k}} m^2} \sum_{n,\mathbf{k}} \frac{df(E_{\mathbf{k},n})}{dE_{\mathbf{k},n}} \frac{\eta\omega\hat{\mathbf{M}}_{\alpha,\beta}}{\omega^4 + \eta^2\omega^2} + \cdots$$

$$\cdots + \frac{8\pi e^2}{\Omega N_{\mathbf{k}} m^2} \sum_{n \neq n'} \sum_{\mathbf{k}} \frac{\hat{\mathbf{M}}_{\alpha,\beta}}{E_{\mathbf{k},n'} - E_{\mathbf{k},n}} \cdots$$

$$\cdots \frac{\Gamma\omega f(E_{\mathbf{k},n})}{\left[(\omega_{\mathbf{k},n'} - \omega_{\mathbf{k},n})^2 - \omega^2\right]^2 + \Gamma^2\omega^2} \tag{5.23}$$

where the input parameters Γ and η are respectively *intersmear* and *intrasmear* parameters, namely the former is the Drude-Lorentz broadening parameter for the interband contribution, and the second is the broadening parameter for the intraband, i.e. metal Drude like term, in case of Gaussian broadening applied during the self-consistent calculations. Finally, by means of the Kramers-Kronig transformation, the real and complex part of dielectric function are calculated.

Now, we consider the squared matrix elements that is defined as follow:

$$\hat{\mathbf{M}}_{\alpha,\beta} = \langle u_{\mathbf{k},n'}|\hat{\mathbf{p}}_\alpha|u_{\mathbf{k},n}\rangle\langle u_{\mathbf{k},n}|\hat{\mathbf{p}}^\dagger_\beta|u_{\mathbf{k},n'}\rangle \tag{5.24}$$

$$\propto u^\star_{\mathbf{k},n'}(\mathbf{r})\frac{d}{dx_\alpha}u_{\mathbf{k},n}(\mathbf{r})u^\star_{\mathbf{k},n}(\mathbf{r})\frac{d}{dx_\beta}u_{\mathbf{k},n'}(\mathbf{r}) \tag{5.25}$$

the double index reveals the tensorial nature of $\epsilon_2(\omega)$, since it depends on the probing direction, while $|u_{\mathbf{k},n}\rangle$ is one of the components of the single particle Bloch function obtained by the DFT calculation. Since also PWSIC works on a plane wave set, the Bloch functions of the matrix element 5.24 are decomposed as follow:

$$|\psi_{\mathbf{k},n}\rangle = e^{i\mathbf{G}\cdot\mathbf{r}}u_{\mathbf{k},n} = \frac{1}{\sqrt{V}}\sum_{\mathbf{G}} a_{n,\mathbf{k},\mathbf{G}}e^{i(\mathbf{k}+\mathbf{G})\cdot\mathbf{r}} \tag{5.26}$$

and consequently:

$$\hat{\mathbf{M}}_{\alpha,\beta} = \Big(\sum_{\mathbf{G}} a^\star_{n,\mathbf{k},\mathbf{G}}a_{n',\mathbf{k},\mathbf{G}}G_\alpha\Big)\Big(\sum_{\mathbf{G}} a^\star_{n,\mathbf{k},\mathbf{G}}a_{n',\mathbf{k},\mathbf{G}}G_\beta\Big). \tag{5.27}$$

Defined in this way the matrix element accounts only for interband transitions, i.e. vertical transition in which the electron momentum **k** is conserved (optical approximation). In standard optics the intraband transitions give a neglectable contribution due to the very low momentum transferred by the incoming/outcoming photon.

In all cases illustrated above the non-local contribution due to the pseudopotential is neglected. In fact the correction to the matrix element that take into account the non-local part of the Hamiltonian it's not implemented. Thus in the following, we summarize this problem as reported by Kageshima and Shiraishi [70]. The main problem stays in the calculation of the momentum matrix element, fundamental for optical properties computation, as in $\varepsilon(\omega)$, defined as

$$\mathbf{P}_{mn} = \langle \phi_m \left| \mathbf{p} \right| \phi_n \rangle \,, \tag{5.28}$$

within the pseudopotential framework. Generally speaking, ϕ_n are wave function of the nth electronic state, and $\mathbf{p}$ is the momentum operator. If wave functions were *all-electron,* the calculating of these momentum matrix elements, by their first derivative, would be calculated correctly. When the wave functions are obtained by the pseudopotential method, they are smoother around the atomic cores in order to minimize the number of base functions, compared with the actual wave functions that have more oscillation nearby the atomic cores. Such *core-localized* differences could affect momentum matrix elements calculated from Eq.(5.28) within the pseudopotential approach.

In their paper [70], Kageshima and Shiraishi introduce a *core-repair* term to calculate the momentum matrix using both norm-conserving or non-norm-conserving pseudopotential schemes.

The idea is to calculate the element $\mathbf{P}_{mn}$ between the mth state and the nth state, adding a atomic-dependent core-repair term. In such way $\mathbf{P}_{mn}$ becomes

$$\mathbf{P}_{mn} = \langle \psi_m \left| \mathbf{p} \right| \psi_n \rangle + \sum_{i,j,I} \langle \psi_m | \beta_i^I \rangle \, \mathbf{p}_{ij}^I \, \langle \beta_j^I | \psi_n \rangle \,, \tag{5.29}$$

where $\mathbf{p}_{ij}^I$ is defined as

$$\mathbf{p}_{ij}^I = \langle \phi_i^I \left| \mathbf{p} \right| \phi_j^I \rangle - \langle \psi_m^I \left| \mathbf{p} \right| \psi_n^I \rangle \,. \tag{5.30}$$

The second term of Eq. (5.29) is exactly the core-repair term and $\mathbf{p}_{ij}^I$ is the core-repair coefficient. In these equations, ψ_m is the pseudo-wavefunction of the mth state, ϕ_i^I is the ith actual wave function of the isolated Ith atom, ψ_i^I is the ith pseudo-wavefunction of the isolated Ith atom, and β_i^I is the projector extracting the part corresponding to ψ_i^I from pseudo-wavefunctions. As we can note all the core-repair coefficients can be calculated from Eq. (5.30) for isolated atoms, hence only once for each element, directly from the pseudopotential calculation. As authors note, equation (5.29) is very efficient in practical calculations reducing the time spent in computing the momentum matrix elements using pseudopotentials. Two key factor are important: the core-repair coefficients are essentially atomic, so they have to be calculated only once for each element; and in the case of separable-type pseudopotentials the values for $\langle \psi_m | \beta_i^I \rangle$ have already been calculated during the calculation. Furthermore, since the norm-conserving feature has not been assumed in deriving Eqs. (5.29) and (5.30) the core-repair term is valid for non-norm-conserving pseudopotentials as well. This allows the use of the Vanderbilt ultrasoft pseudopotentials to calculate the electronic and structural properties of materials with first-row or transition-metal elements, which are not easy to be calculated using general norm-conserving pseudopotentials.

We have begun to implement in our PWSIC code this core-repair contribution following this scheme and starting from the relative VASP routine that calculate it [71], even if properly modify since it is written for PAW scheme. However, our core-repair routine has not been full completed and tested yet. Hence, in the following we will assume that the dielectric function has been calculated without this correction. This is not critical for many materials as shown in [70, 71]. Some trial calculations of dielectric function have been performed to test the correct working of the implemented routine, for bulk material such as diamond, Si, SiC, GaAs, GaN, yielding to comparable results with those reported in Refs. [70, 71].

Concluding, I report in Figure 5.2 (top) the imaginary part of dielectric function of Ga_2O_3, calculated with PWSIC code together with that reported by He et al in [161] (bottom). The two spectra are in general agreement, considering also the different method used (Hybrids in the second one).

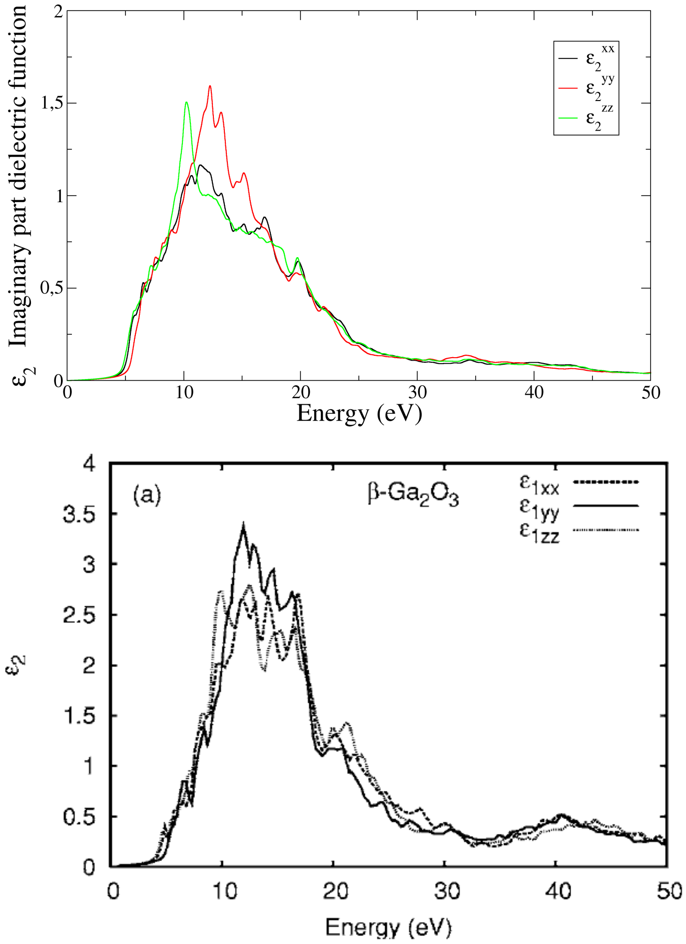

Figure 5.2.: Imaginary part of dielectric function $\epsilon(E)$ of Ga_2O_3 calculated with PWSIC code (top) and from Ref. [161] (bottom).

6. $CaCu_2Ti_4O_{12}$

Below, I report a work published in the paper [199], wherein I perform non-collinear calculation for some spin configuration of the paramagnetic phase and their relative dielectric functions. Moreover, I dealt with GW assessment of the gap. To summarize the work, we report the electronic properties of the quadruple perovskite $CaCu_3Ti_4O_{12}$ as obtained via several density-functional based methods, and propose a new interpretation of optical experiments to the effect that four distinct transitions (with onset around 0.7, 1.5, 2.5, and 3.4 eV) contribute to the spectrum. The comparison with experiment is satisfactory, especially after we account for the effects of spin disorder, which does not close the fundamental gap but suppresses the transition intensity. Our comparison shows that some of the methods we employ tend to strongly overestimate the gaps for standard values of the respective adjustable parameters.

6.1. Introduction

The popular line “If it’s been measured, why are you calculating it ?” attributed to Volker Heine emphasizes the need for electronic structure theory to harness its predictive and interpretive potential. In this paper, we revisit the low-energy optical properties of the quadruple perovskite $CaCu_2Ti_4O_{12}$ (CCTO henceforth, risen to popularity a decade ago[123] because of its anomalous dielectric response), heeding the advice implicit in Heine’s remark in two distinct respects. Firstly, theoretical predictions predated reliable experiments, and here we provide a new and improved interpretation of the latter. Secondly, electronic structure theory often revisits known results to provide additional insight and to validate its predictive power in retrospect. In this spirit we apply to CCTO several density-functional-theory (DFT) state-of-the-art methods, which yield a mixed bag of good and bad news. Some advanced methods appear to be struggling, while others yield satisfactory agreement with experiment.

6.1.1. Motivation

Early experimental reports[123] on CCTO circa 2002 had suggested a fundamental gap in excess of 2.5 eV. Values as low as 0.2 eV obtained in DFT local-density-approximation (LDA) calculations[124] were, not unreasonably, discounted in view of the known gap underestimation problem of local and semilocal functionals. Looking at the LDA bands, however, we realized that the lowest gap might be a low-energy transition between localized and predominantly Cu-like states, rather than the natural dipole-allowed transition between O p valence and Ti d conduction bands, a situation analogous to other Mott-like insulators.[125] Therefore, in 2006 we used[127] self-interaction corrected LDA (PSIC),[57] known by then to reproduce quite accurately the gaps in many Mott-like cuprates,[56] to find out how beyond-LDA bands would look like in the Cu-dominated gap region. We found that the fundamental gap (indirect, forbidden, and between mostly Cu-like states) was only about 0.6 eV, moderately increased in absolute value over the LDA value. This surprising result seemed to point to smaller-than-usual correlation effects in the nearly filled $3d$ Cu(II) shell; put differently, the on-site interaction, which self-interaction corrections largely restore to its correct size, appeared to be rather more screened at Cu sites in CCTO than in other magnetic Cu oxides.[56, 128] Systematic experiments (see Sec.6.3.3 below) first appeared in 2008, when Kant *et al.* inferred[129, 130] from optical conductivity an electronic structure qualitatively matching that suggested by LDA[124] and, to a somewhat larger extent, by PSIC,[127] with weak Cu-dominated transitions starting at about 0.5-0.7 eV. In 2011, a different picture was proposed,[131] to the effect that the “Cu-Cu” transition would start at about 1.8 eV, based on reflectivity measurements interpreted via GGA+U (Generalized Gradient Approximation +U). The calculations used a U–J parameter much smaller than the usual value for Cu oxides (reminding us of the low-correlation argument), yet it produced a fundamental gap much larger than previously obtained by PSIC. This suggested that it would be a good idea to revisit and expand our previous investigation applying further advanced methods to $CaCu_3Ti_4O_{12}$ to help sort out the matter and provide a robust interpretation. In this work, we discuss the electronic properties of CCTO based on results from several different DFT-based methods. We eventually propose an interpretation of experiments, as well as further experimental tests, based on one of them, the variational PSIC method[132] (VPSIC henceforth). Our conclusion in summary is that CCTO has a multifold interband absorption due to its unusual Cu-induced upper-valence and lower-conduction band structure, and that the fundamental transition peaks around 0.7-0.8 eV (1500 nm), while the absorption peaking at 1.8 eV (700 nm) is an O p valence band to Cu d conduction band transition, at variance with the previous interpretation.[131] More intense absorptions between 2.5 to 4 eV are due to transitions into the higher-lying Ti d conduction band. The fundamental gap is a Mott-like gap in the sense that the system has an odd electron count, the gap open between strongly localized and spin-polarized states, and would not exist in the absence of magnetic moments. We account for spin disordering in the paramagnetic (PM) phase in which most measurements are performed: the fundamental gap survives unscathed the breakdown of magnetic order, but the intensity of the transition across that gap is suppressed. As a test of the suggested picture, we point out features that should be observable in low- vs high-temperature optical and energy-loss spectroscopy experiments. Besides VPSIC, and GGA/LDA, we calculate the electronic structure using GGA+U, a hybrid functional, and many-body perturbation theory. Our theory-experiment comparison indicates that some advanced methods end up quite far from experiment, overestimating severely the gaps, whenever standard values are used for the adjustable parameters they depend on, a conclusion that has obvious methodological implications. Also, the corrections to local- or semilocal- functional eigenvalues provided by VPSIC are close to those of non-self-consistent one-shot GW, suggesting that the "beyond-local" correlation is described by VPSIC with similar accuracy.

6.2. Methods

As usual in the business of ab initio optical properties, we elect to interpret the eigenvalues and eigenvectors of Kohn-Sham equations as quasiparticle energies and states. This is justified by the Kohn-Sham equations being formally identical to Hedin-Lundqvist quasiparticle equations[126] if the self-energy Σ is identified with the exchange-correlation potential; for LDA, e.g., $\Sigma_{\mathrm{LDA}}(\mathbf{r},\mathbf{r}',E)\equiv\delta(\mathbf{r}-\mathbf{r}')\delta(E)$ $\mathrm{V}^{xc}_{\mathrm{LDA}}(\mathbf{r})$, and similarly for functionals containing some degree of non-locality and implicit energy dependence such as hybrids or PSIC.[56] It is obviously interesting, therefore, to compare results obtained by different exchange-correlation functionals. This is done in Sect.6.4, in particular 6.4.1; In the same spirit, we also discuss in Sect.6.4.3 "many-body" corrections to semilocal functionals, both empirical and based on $\mathrm{G}_0\mathrm{W}_0$ non-self-consistent many-body perturbation theory.[140] In recent years, methods going beyond the local or semi-local approximation have become more affordable, and we are in the position to evaluate their relative merits under the assumption stated above. The optical conductivity, extinction coefficient, and electron-energy-loss function are extracted from the dielectric function $\tilde{\varepsilon}(\omega)$ calculated within the random phase approximation from the joint density of states obtained with the variational version of pseudo self-interaction-corrected LDA (VPSIC).[57, 56, 132] We also calculate gaps and transitions with Ceperley-Alder LDA,[134] Perdew-Becke-Ernzerhof GGA,[135] the Dudarev GGA+U functional,[136] the Heyd-Scuseria-Ernzerhof (HSE) hybrid functional.[137] To avoid bias due to changes in volume, we use the cubic magnetic primitive cell (40 atoms) at the experimental lattice constant of 7.38 Å with internal coordinates optimized with GGA, imposing a threshold of 0.01 eV/Å on force components. CCTO is cubic, so that Ti-O octahedra and Cu-O plaquettes are all identical geometrically (see Fig.6.1); also, the positions of Ti, Cu and Ca are fixed by symmetry; those of the O's are determined by the Ti-O distance, 1.959 Å, and the Cu-O distance, 1.963 Å. VPSIC uses ultrasoft pseudopotentials and plane waves in a home-made custom code with cutoff 475 eV. All other methods are implemented in VASP[210] and use the PAW[213] method with cutoff 400 eV. We employ standard k-point meshes (4×4×4 for self-consistency and up to 12×12×12 for density-of-states or dielectric function calculations). In the optics calculations, the imaginary part ϵ_2 of the dielectric function is calculated directly, whereas the real part is obtained via the Kronig-Kramers relations (for standard relations, see e.g. Ref.[141]); we use up to 2000 bands in the summation over empty states (for the $\mathrm{G}_0\mathrm{W}_0$ calculations, see the discussion in Sec.6.4.3), which are amply sufficient to converge both the imaginary and real parts of the dielectric constant at the

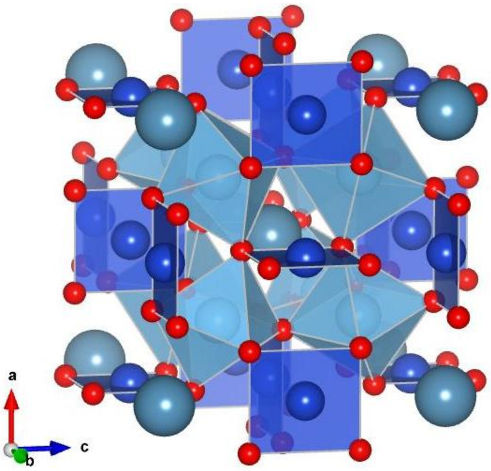

Figure 6.1.: Crystal structure of CCTO.

energies of interest (below about 10 eV). Some of the techniques employed involve adjustable parameters. The Dudarev GGA+U version depends on parameter U–J, applied to Cu d states. The HSE hybrid, in turn, is tuned via the fraction α of screened Hartree-Fock exchange and the screening cut-off wavevector μ. In the current VPSIC formulation, screening of the self-interaction by the environment is quantified by a constant which may be treated as a parameter. However, we keep it fixed, as in all past applications, at a value based on a Slater-transition-state concept explained in Ref.[57].

6.3. VPSIC results vs. experiment

This Section compares the VPSIC optical functions of CCTO with two distinct sets of experimental data. In Sec.6.4 we will examine and discuss the gaps provided by the other methods. We will be switching units several times to ease the comparison with experiment.

6.3.1. Band structure

CCTO is G-type antiferromagnetic (AF) on the Cu lattice with a Neél temperature of 25 K. Its band structure obtained by LDA and VPSIC is displayed in Fig.6.2.

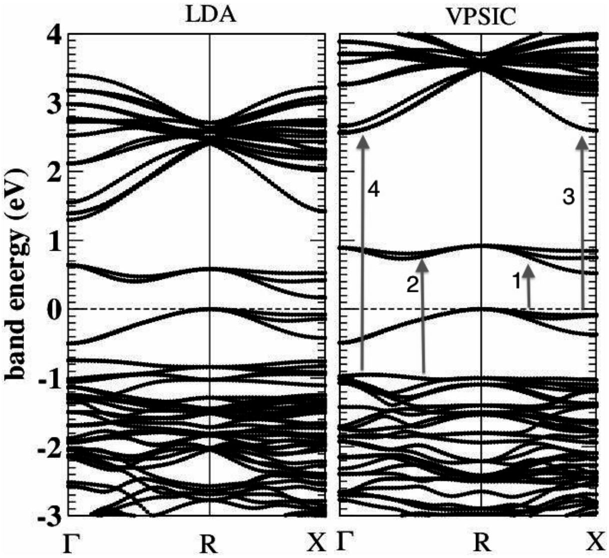

Figure 6.2.: LDA vs VPSIC bands of CCTO. Arrows indicate schematically the four transitions discussed in the text.

The LDA and VPSIC bands are rather similar in structure and energy separation. The near-gap bands connected by the transition marked ‘1’ in Fig.6.2 are dominated by O-hybridized Cu-like spin-polarized states. The top valence band and the bottom conduction band are fully spin-polarized, and as can be seen in the orbital- and site-projected density of states (DOS) as obtained by VPSIC in Fig.6.3, their projections on any given Cu site have opposite polarization. As usual, the removal of self-interaction tend to increase all the gaps. The largest increases are found for the transitions marked ‘3’ and ‘4’ in Fig.6.2 to the upper conduction band of predominantly Ti character, i.e. for the standard charge transfer gaps. The local orbital character of the near-gap spin-polarized states is completely determined by Cu *d* and ligand O’s in each plaquette (see Fig.6.4), in accordance with the DOS of 6.3. As far as optical absorption is concerned, the band structure in Fig.6.2 suggests that four distinct relevant absorptions are expected, marked ‘1’ to ‘4’. The first transition is between O-hybridized Cu-like bands, between 0.5 and 0.9 eV (2000-1000 nm, 4000-7000 cm^{-1}). A large joint DOS is expected due to extended parallel-band sectors especially around the X point; also, despite the similar character of the initial and final states, the matrix elements should not be suppressed, because this is an intersite transition (intrasite transitions are forbidden by the spin conservation selection rule). The second transition is between valence O p and low-conduction Cu d bands in the range 1.4-1.9 eV (800-650 nm, 11000-15000 cm^{-1}), which is not expected to be suppressed selection-rule-wise. The third absorption is Cu d upper-valence to Ti d-O p conduction at 2.6-3.0 eV (500-400 nm, 21000-24000 cm^{-1}), which is expected of average intensity; finally, an intense O p-Ti d transition should start at 3.4 eV (350 nm; 27500 cm^{-1}). The lower conduction band of Cu character is affected only weakly by self-interaction corrections, and accordingly the lower-energy O p–Cu d and Cu d–Cu d transitions '1' and '2' change moderately compared to LDA. This feature is key to our interpretation, and, as we will see in Sec.6.4, it is not shared by other methods. The small magnetic fundamental gap '1' may be labeled as Mott-like, since it depends on the interplay of spin polarization, Hund coupling, and on-site repulsion, and it is coherent with the textbook definition U–ct, i.e. it includes (thanks to self-interaction removal) the cost U of adding an electron in the empty d state as

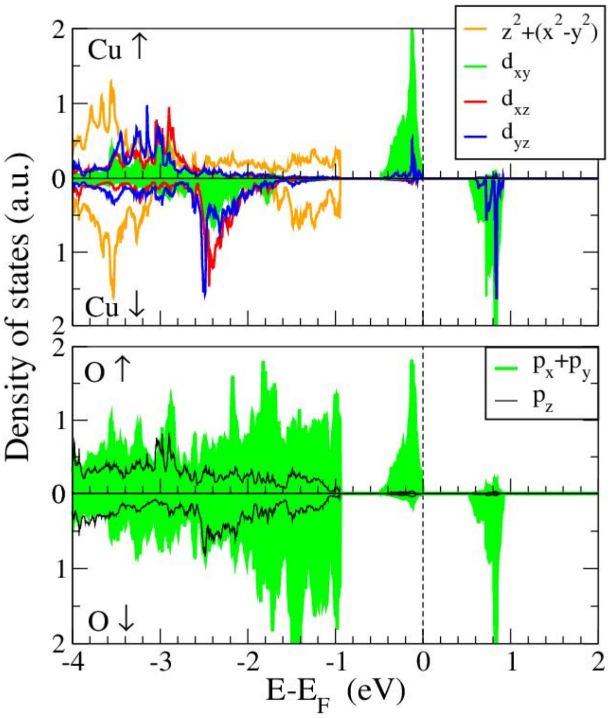

Figure 6.3.: Atom-projected DOS of CCTO from VPSIC in the near-gap region, projected on the Cu and O atoms of a plaquette in the xy plane.

well as the hopping t, which is included in the band width.[133] Since even LDA finds this gap (albeit barely), the on-site correlation acting on these states must not be especially strong. Further, the stronger O p-Cu d hybridization plays a role in reducing the gap in CCTO compared to e.g. in $YBa_2Cu_3O_6$, whose gap[128] is 1.2 eV.

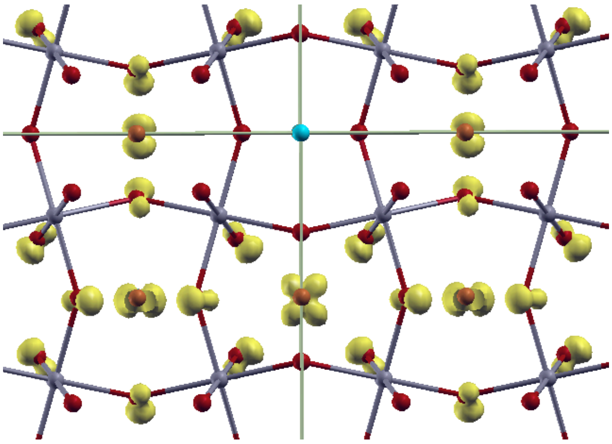

Figure 6.4.: Magnetization density in CCTO. All three kinds of Cu-O plaquettes are visible.

6.3.2. Paramagnetic vs antiferromagnetic phase

Before delving into the comparison, we need to discuss the role of spin disorder. The experiments we consider are done well above the Néel temperature T_N=25 K of the AF phase of CCTO, and therefore probe the paramagnetic (PM) phase. Since PM CCTO is insulating experimentally, it is most likely a collection of thermally disordered, randomly oriented Cu moments, rather than a zero-moment Pauli-type PM (in the latter phase, CCTO is found to be a metal). The fundamental transition, labeled '1' in Figs.6.2 and below, is between Cu-like spin-polarized states (see Fig.6.2 and Fig.6.3) and is spin-selective in the sense that spin-allowed transitions only occur with matrix elements involving same-spin sites of the Cu lattice. In the PM, we expect the intensity of transition '1' to be reduced, because spin mixtures will be involved. To expect a good match with experiment, this suppression should be assessed and accounted for. Our motivation here is not to sample in detail the PM configurations (which is outside our scope and well beyond “naive” sampling techniques); rather we need to show a) that a gap survives in the misaligned-spin, i.e. non-AF-ordered, system when moments are nonzero, and b) that the intensity of the transition between the spin-polarized states is suppressed. While seemingly trivial, point a) is worth making directly. Most many-body physicists scoff at the notion that any ab initio method can (as the PSIC does) obtain good gaps and magnetism in systems (CuO,[153, 154] $LaTiO_3$,[132] $LaNiO_3/LaAlO_3$ superlattices[205] etc.) where LDA or GGA fail, because these are usually studied under the assumption of magnetic order. Indeed, our result shows, albeit at the simplest possible level, that a disordered-moments PM does indeed have a gap (this was shown earlier[142] for MnO with essentially the same electronic-structure technique (and a much better spin-disorder sampling). Point b) is not unexpected: misaligned spins are in mixed up-down states (referred to a given quantization axis), so that projections of spin states on one another are no longer just unity or zero. Transitions connecting sites that were same-spin in the AF will be suppressed, and others between opposite-spin sites will gain nonzero amplitude. How these two effects play out quantitatively needs to be explored directly. To assess the degree of intensity suppression of absorption ‘1’ in the PM phase, we perform non-collinear-magnetization calculations whereby the six Cu moments in the primitive cell are oriented randomly, but directionally constrained to give a total magnetic moment of zero– that is, mimicking in effect one of the thermally accessible configurations of the disordered paramagnet. The non-collinear spins in the PM model are constrained by a penalty function: if that penalty is turned off, the AF ground state is recovered. Spin-orbit coupling is not included in these calculations. Since the low energy bands obtained with semi-local-functionals and self-interaction corrections are quite similar (see Fig.6.2), we use GGA to access the non-collinear and penalty-function features of VASP. As we are only interested in the effect on the lowest gap, we display the low energy portion of the GGA absorption for the PM (aligned to match the VPSIC gap) together with the VPSIC absorption. The key result, as can be seen from the bands in Fig.6.5, is that the gap remains nonzero in the disordered PM, and close to the AF value. This should help dispel the myth that the distruction of magnetic order will lead to metallicity in ab initio calculations. Indeed, it does not, as long as magnetic moments survive.[142] A related result relevant to our interpretation below is that, as we surmised, the fundamental absorption is indeed suppressed in the PM compared to the AF, whereas the rest of the spectrum is practically unchanged. This improves agreement with experiments done at high temperature, as we discuss in the next Section. We report only the low energy portion of the PM optical constants (up to about 1.5 eV), since spin disorder only affects the spin-polarized transition ‘1’. We note in passing that the metallic Pauli-PM phase (not shown) shows typically metallic optical features such as a Drude peak at low-frequency, which are not observed in any of the experiments.

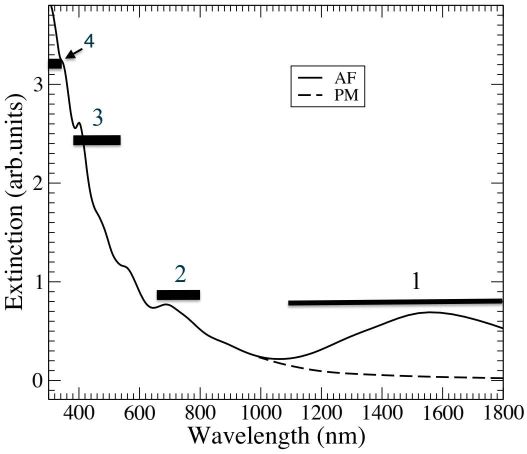

Figure 6.5.: GGA bands for the CCTO cell with non-collinear spins mimicking the disordered PM.

6.3.3. Comparison with experiments

Based on diffuse reflectance measurements, Ref.[131] suggests as lowest-energy transition an indirect-gap absorption peaking at 700 nm, and attributes it to transitions from the mainly Cu-like upper valence states to the mainly Cu-like first conduction band, i.e. to transition ‘1’ of our band structure in Figs.6.2 and 6.3. Higher-energy intense absorptions are attributed to O p-Ti d dipole transitions. [131] This interpretation is based on GGA+U calculations with U–J=6.5 eV, a rather low value for Cu oxides, which nevertheless pushes transition ‘1’ up to the needed 1.7-1.8 eV (see the discussion in Sec.6.4). To compare with this experiment

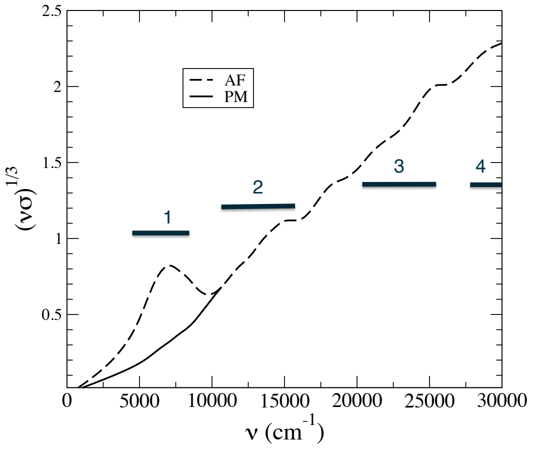

Figure 6.6.: Extinction coefficient for PM and AF CCTO calculated with VPSIC. Compare with Fig.7b (inset) of Ref.[131].

directly, we calculate the extinction coefficient (Fig.6.6) and conductivity (Fig.6.7 and 6.9; see the discussion below) from the dielectric function $\tilde{\varepsilon}(\omega)=\varepsilon_1+i\varepsilon_2$ (the strongest dependence is on the imaginary part ε_2). Based on these results, and in particular the extinction coefficient displayed in Fig.6.6 (to be compared e.g. with the inset of Fig.7b of Ref.[131]), we propose a different interpretation than that just outlined: the peak at 700 nm is the O *p*-Cu *d* labeled ‘2’ in Fig.6.2 and 6.6, which is also an indirect transition; the shoulder at 400-450 nm is the O *p*-Cu *d* labeled ‘3’; and finally the main peak at 300 nm is due to the main interband O *p*-Ti *d* transition, labeled ‘4’. The fundamental transition, which connects the upper valence and bottom conduction Cu-like states and is labeled ‘1’ in Figs.6.2 and 6.6, is instead at lower energy, peaking at about 1500 nm in the AF phase. However, in the PM the intensity of this absorption is suppressed. As no experimental data were reported[131] in this wavelength region, it is probable that no significant signal was detected. Account for spin disorder resolves the potential discrepancy. Conversely, our result suggests that similar experiments in the AF phase at low temperature (and pure, untwinned, magnetically ordered crystals) should reveal this low-energy transition, providing a direct experimental countercheck of our interpretation. We now come to wide-range dynamic conductivity measurements,[129] which also seem to suggest a multigap spectrum. Tauc extrapolation at low energy is difficult due to low intensity and the probable indirect

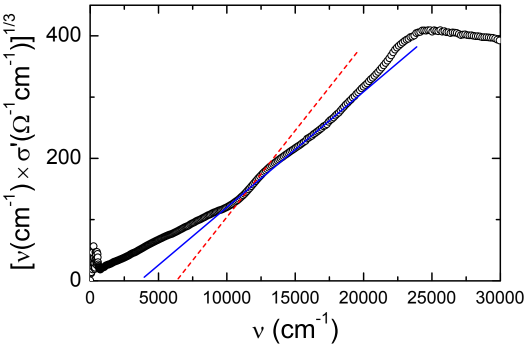

Figure 6.7.: Tauc relation for CCTO (exponent for indirect forbidden transitions) calculated with VPSIC. Compare with Fig.6.8.

character of the transition, but a very weak indirect transition starting at about 5000 cm^{-}1, can be inferred.[129, 130] Another more intense transition follows at about 1.5-1.7 eV and finally the intense allowed absorption peaks at 3 eV. These

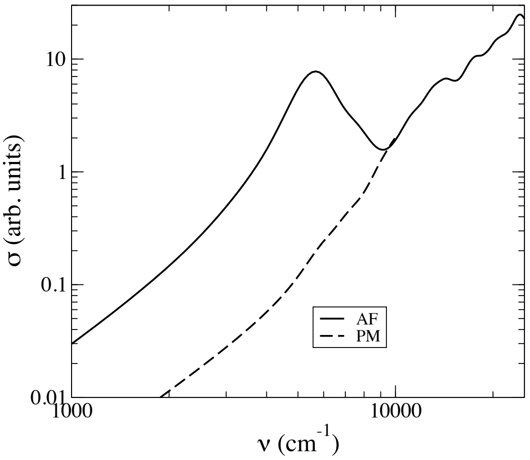

Figure 6.8.: Experimental Tauc relation[130] for CCTO, to be compared with Fig.6.7. Lines are possible fits for indirect forbidden transitions whose intercepts with the frequency axis identify the minimum gap. Figure by courtesy of P. Lunkenheimer.

features are reasonably well reproduced by our calculation for the PM in Fig.6.7, as can be seen comparing with the experimental data in Fig.6.8, where the Tauc fits suggest an onset (i.e. a minimum gap) at about 0.6-0.9 eV. This assignment is only tentative as there is no clear linear behavior over an extended frequency range. Comparing AF and PM results, it appears that the seemingly strongly forbidden character of the fundamental transition is mainly a token of spin disorder, rather than of interband matrix element suppression. Indeed, intrasite *d*-*d* transitions would be suppressed by Laporte's selection rule, but here they are effectively intersite, because of the spin structure of the material; the fundamental transition in the AF is in fact quite prominent (Fig.6.6 and Fig.6.7). A related result from Ref.[129] is that DC conductivity is Arrhenius-activated with a 0.2 eV characteristic energy. We attribute this simply to thermal carriers excitation across the fundamental gap. The latter is 0.6 eV in VPSIC, but we have estimated from a single GGA calculations including spin-orbit (not shown in the Figures) that the spin-orbit splitting of the upper valence and lower conduction bands (both having sizable Cu character) will reduce the gap to about 0.3 eV. In closing this Section, we point out that beside low-temperature optical absorption another possible countercheck on our suggestions is electron-energy-loss spectroscopy, again in the 0.5-1 eV range. As shown in Fig.6.10, the energy-loss function –Im$[1/\tilde{\varepsilon}(\omega)]$ has a marked peak at 0.9 eV in the AF (i.e. at low temperature) which is strongly suppressed in the PM (i.e. at high temperature) because of spin disorder. The sharp main plasmon at 13.5 eV (Fig.6.10, inset) is the same in the AF and PM.

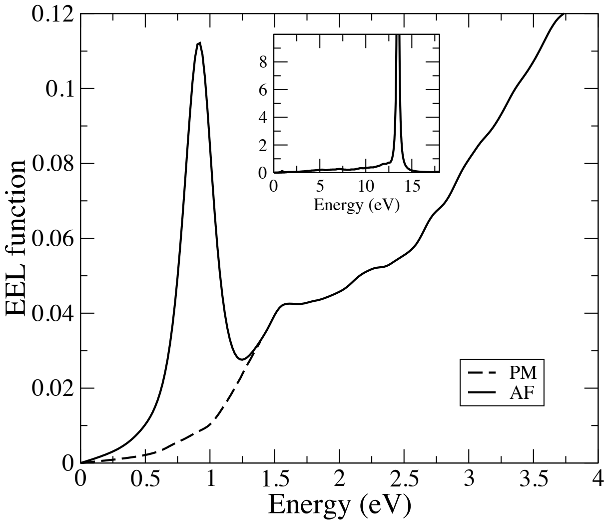

Figure 6.9.: Dynamical conductivity for CCTO calculated with VPSIC. Compare with Fig.7 of Ref.[129].

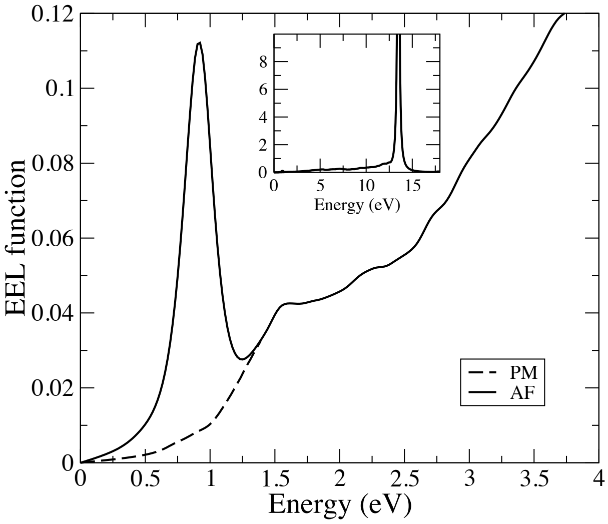

Figure 6.10.: Energy-loss function of AF and PM CCTO. The inset shows the main plasmon in the AF.

6.4. Results with other functionals

Having obtained a satisfactory interpretation of the electronic structure of CCTO using VPSIC, we examine and compare the main band gaps obtained by GGA+U and the HSE hybrid functional. As mentioned earlier, GGA+U in the version employed here depends on the U–J parameter; we apply to the Cu d shell a U–J ranging from 0 to 8 eV (a value of 8 or 9 eV is standard[128] for Cu oxides). The HSE hybrid depends on the fraction α of screened Hartree-Fock exchange and the screening cut-off wavevector μ: we consider α=0, 0.1, and 0.25, the latter being the proper HSE recipe (while varying α, we keep the standard μ=0.2 Å^{-1}); then we explore values of μ from 0.1 to 0.5 Å^{-1}, at the standard α=0.25 (large μ means strongly screened Fock exchange at all wavevectors, recovering GGA as $\mu\to\infty$). The HSE standard value has a theoretical foundation in the formulation of the functional, and has the merit of being system-independent. That said, we deem this exploration worthwile, as the α and μ parameters have been, on occasion, adjusted away from their standard value to cure various different issues in cuprates and titanates. Finally we discuss quasiparticle corrections from GGA-based G_0W_0 many-body perturbation theory; G_0W_0 has no adjustable parameter per se, but uses the GGA bands to evaluate the Green's function and screened interaction, whence the quasiparticle energies, and is not self-consistent.

6.4.1. Parameter dependence of main gaps in HSE and GGA+U

In this Section we show a selection of band gaps of AF CCTO as function of the relevant adjustable parameters of the various methods. The gaps we consider (with reference to the labeling of Fig.6.2) are the fundamental gap, i.e. the '1' transition; the main charge transfer gap, i.e. the '4' transition; the upper valence-upper conduction gap, i.e. the '3' transition; and the minimum gap between the Cu-like lower conduction band and the Ti-like upper conduction band, i.e. roughly the difference of the '4' and '1' transitions, labeled '$\mathrm{Cu_{dn}}$-Ti'. (As the values are taken at the Γ point, the values may seem occasionally inconsistent with the previous results, but deviations are tenths of an eV, i.e., as will be seen, an order of magnitude less than the discrepancy with experiment.) These gaps are shown for GGA+U as function of the U–J parameter in Fig.6.11, for HSE as function of the mixing parameter α in Fig.6.12 and of the screening parameter μ in Fig.6.13. By construction, plain GGA is recovered in each of the limits of vanishing U–J, α, and $1/\mu$. As expected, all valence-to-conduction gaps increase rapidly with U–J, α, and $1/\mu$. The '1' transition increases fastest in all cases, and the

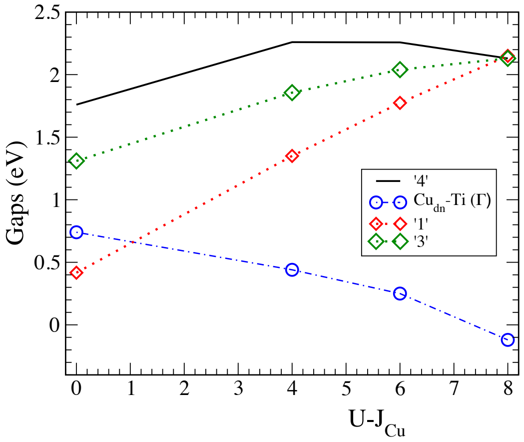

Figure 6.11.: (Color online) GGA+U gaps vs U–J.

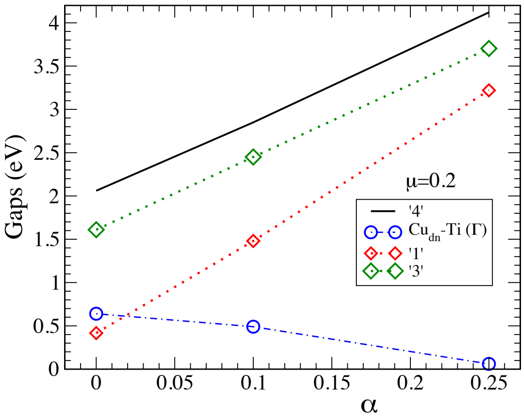

Figure 6.12.: (Color online) HSE gaps vs α, with μ fixed at 0.2 Å^{-1}.

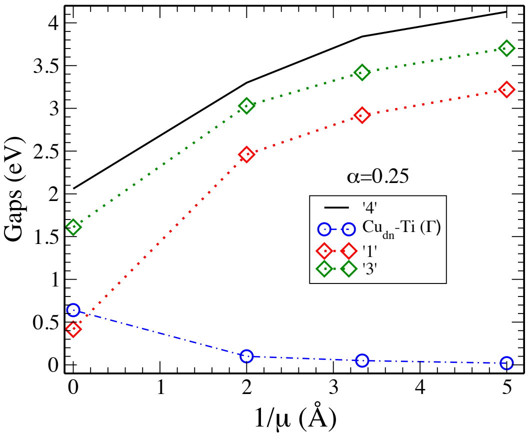

Figure 6.13.: HSE gaps vs $1/\mu$, with α fixed at 0.25

conduction-conduction gap diminishes. This means that, relative to the valence band, the Cu-like lower conduction bands are pushed up in energy more than the Ti-like upper conduction bands, opposite to what is observed in VPSIC. This effect is especially strong in GGA+U: the '1' transition ends up being larger that the '4' (which at standard U–J is 45% underestimated), i.e. the empty Cu band is pushed into the Ti band. This is due to the fact that the U correction acts efficiently on the Cu-like bands by enhancing both spin polarization and orbital polarization. The former widens the '1' gap; the latter cleans up the O p valence from Cu-like character, pushing it down and widening somewhat the apparent charge transfer gaps. We do not apply a U on Ti. That would only have minor, if any, effects: Ti orbitals are not spin-polarized, and U would only leverage orbital polarization, i.e. it would purge the valence and Cu-like states of what little Ti orbital content they have, thereby widening modestly, if at all, the relative gaps (at least for physically sensible values: of course one may always hope to get some effect for unphysically large U's). In conclusion, to obtain a '1' transition in the vicinity of 1 eV or less, U–J should be between 2 and 3, which is tiny by Cu-oxide standards. In HSE, all gaps increase linearly with α (Fig.6.12), with the '1' transition increasing faster than the others. As Fig.6.13 shows, all the gaps decrease as μ increases, i.e. when the Hartree-Fock exchange is gradually screened away. At standard α the HSE functional gives a fairly good '4' transition, 4.1 eV at Γ. The '1' transition is overestimated hugely at over 3 eV, whereas, depending on which experiments one believes and whatever uncertainties one may attach to them, that gap is in the range of 0.5-1.5 eV at most. To obtain such a value one should either use a small α in the vicinity of 0.05, or, probably better, a more or less standard value like 0.15 to 0.25 with a larger than usual μ (as large as 1.6 Å for α=0.25). One way of stating this is that, compared to the upper bands, the Cu *d* bands gets too large a "correlation" correction (in the commonly-used, if questionable, sense of "any correction needed beyond semilocal DFT") from standard HSE, and that the correction should be more "screened" than it is, consistently with the smaller-than-usual U–J mentioned above for GGA+U. An additional issue enhancing the sensitivity of Cu states to U-like corrections may have to do with the fact that the band structure of CCTO is dominated by long range hoppings.[143] Whatever the final answer, this overcorrection cannot be attributed (not straightforwardly, anyway) to self-interaction removal, which operates –although in different guises– in both HSE and VPSIC, and has moderate effects on the Cu states in the latter. It is worth reiterating that the parameters in common use in the literature are those at the high end of the range considered here. U–J up to 8 or 9 eV is quite usual in Cu oxides,[128] and α=0.25, μ=0.2 Å^{-1} is the standard HSE recipe. For those values, both GGA+U and HSE produce an electronic structure whereby the Cu-like conduction states are way too high in energy, and the gap is too large by a factor of at least 3. Used in their default setting, GGA+U and HSE would predict a fundamental gap '1' of 2.2 eV and 3.2 eV respectively, whereas experiments and VPSIC agree that CCTO has a gap of less than 1 eV. Besides, the multiple absorptions involved in the CCTO spectra are not reproduced, as they end up being squashed by the overcorrection into a single high-onset-energy transition.

6.4.2. Discussion

There are some general conclusion to be drawn from the results just discussed. At the very bottom, GGA+U, HSE, and VPSIC are all semiempirical methods, in that they depend on some sort of parameter. One recognizes, though, that these parameters intervene very differently in each method. By construction, GGA+U is the most directly affected by its internal parameters. These can be estimated to some degree on a non-empirical basis from atomic quantities[144] or from linear response,[145] but in all cases they are externally-determined system-dependent inputs (occasionally even dependent on internal parameters or external conditions[146] within the same system), and not self-consistent and internal, so that in the end they are simply regarded as adjustable by most practitioneers. Whether this is admissible or desirable is as much a philosophical as an operational question that depends on the specific objectives of an investigation. In the present case we found that the consolidated parameter recipe simply does not seem to function. One may (we don't) elaborate further about which atom and shell the correction should be applied to (e.g. would U's on Ti or O p make a difference: we argued above that they would not cure the problem), adding more parameters: this would probably bring us no nearer to a solution. As mentioned, HSE's standard recipe has a theoretical foundation in the formulation of the functional, and has the merit of being system-independent (beside the practicality of including screening at the functional formulation level, and not a posteriori as in other hybrids[147] based on, again, empirical estimates[149] of the screening). That said, the α and μ parameters have been adjusted away from their standard value to cure various different issues (structure, electronic properties, magnetism, etc.) in many occasions, among which cupric oxide CuO.[150] It is only fair to discuss in this context the parametric dependence built into VPSIC. For a detailed treatment we defer to the original work[57] and to a recent review,[56] which also discusses in detail the analogies and differences with GGA+U and hybrids. In short, the screening of atomic self-interaction corrections by the environment is described by a single parameter α_s=1/2, a value based on a Slater transition-state argument.[57] The dependence on α_s of relevant quantities in solids has been studied,[151] and the result is that α_s=1/2 is indeed the optimal value on average over a vast class of materials. We systematically use that value,[56] hence effectively we do not regard α_s as a parameter at all. In a case where a detailed comparison has been carried out,[152] VPSIC has been found to perform similarly to HSE; discrepancies (and controversy) did occur in other cases, however, especially on cupric oxide.[150, 153, 154] Since we are dealing with a titanate that is strongly characterized by cuprate-like electronic features,[156] it is appropriate to recall the solid success record of VPSIC on the electronic and structural properties of Cu oxides of various composition and dimensionality. It describes correctly the magnetic and insulating (anywhere from semiconducting to high-insulator) character of $YBa_2Cu_3O_6$,[128] monoclinic CuO,[153] $GeCuO_3$,[157] Ca-doped YCuO cuprate,[158] all of which are metals and non magnetic in GGA. This is further, strong circumstantial evidence supporting the use of VPSIC as reference for the other methods in CCTO, even if one were to gloss over the experimental evidence discussed above.

6.4.3. Quasiparticle corrections

It has long been customary to estimate quasiparticle energies as density-functional eigenvalues supplemented by "self-energy corrections".[148, 149] In many materials, these corrections are dominated by a "scissor operator", i.e. a k- and energy-independent relative shift of conduction and valence bands. A simple empirically-determined scissor correction[149] is $\Delta \simeq 9/\varepsilon_\infty$ eV. CCTO has a high-frequency dielectric constant $\varepsilon_\infty = \varepsilon_1(\omega=0) = 12.6$, so the correction is $\Delta \sim 0.7$ eV. The resulting total minimum gap is roughly 0.85 eV, essentially in the VPSIC (and experimental) ballpark. Thus, the VPSIC and empirical scissor give similar corrections to local functionals, despite being completely unrelated. Next we calculate the same sort of correction using G_0W_0 non-selfconsistent quasiparticles.[140] The latter calculation is rather difficult to converge in general, and particularly for this large system. We use a softer O potential enabling a cutoff of 280 eV, which does not seem to affect the eigenvalues much. (The use of the specialized potential PAW sets provided with VASP for GW calculations is prevented by their large energy cutoff; this should not be a serious problem, as the standard PAWs we use do contain high-energy projectors and should perform rather well in the low-energy range we deal with here.) To assess convergence in k and in the number of bands for the virtual-transitions summation we used 2×2×2 and 4×4×4 k-grids and between 256 and 4092 bands. For a typical bulk material the latter choice would be overkill, but our system has of order 130 occupied bands per spin channel, so this setting seems necessary. Note also that that energy convergence in GW is more critical than in the standard joint-DOS calculations in the previous Sections: in the latter, unoccupied bands are only used in the Kronig-Kramers relation, whereas in GW they enter the evaluation of all energy-dependent parts of the self-energy.

Table 6.1.: Corrections to (semi)local transition energies (in eV, rounded to tenths of eV, labeled as in Fig.6.2).

Transition	'1'	'2'	'3'	'4'
Δ(VPSIC–LDA)	0.5	0.7	1.1	1.4
Δ(G_0W_0–GGA)	0.7	1.0	1.1	1.4
Δ(empirical)		0.7		

In the area of optics, at the simplest level of approximation, it has long been customary to address "beyond-LDA" (or GGA) corrections to eigenvalues or gap energies. We adopt this view and obtain the corrections as the differences of eigenvalues within GW and GGA, and VPSIC and LDA respectively. This should keep bias at a minimum in the comparison of the different technical settings (potentials, chosen volume, DFT functionals, ...) and codes, besides hopefully providing some error cancellation. The corrections are reported in Table 6.1 for the X point. From the above partial convergence study in bands and k-points, we judge that they are converged to within 0.1 eV. Interestingly, the GW and empirical corrections agree well for the low energy gap; the GW and VPSIC corrections are also in decent overall agreement, and in particular they appear to depend on energy, i.e. higher bands are corrected more than the lower ones. In particular, the differences between Cu and O *p* upper valence, and Cu and Ti conduction states are the same in VPSIC and GW, i.e. the Cu *d* empty band remains well clear of the Ti empty bands in both cases. Also, the lowest-energy GW gaps have the same character and order as in VPSIC, the first gap being indirect between R and X and the second direct at X and less than 0.1 eV larger, i.e. the low-energy band topology appears similar in the two cases. Thus, overall, the corrections to local-functional eigenvalues provided by VPSIC are close to those of non-self-consistent one-shot GW, suggesting that much of the "beyond-local" correlation is indeed provided by VPSIC with similar accuracy, at least in this material.

6.5. Summary

We examined the electronic structure of $CaCu_3Ti_4O_{12}$ as obtained via several different density-functional based methods, and proposed a new interpretation of experiments to the effect that four distinct transitions contribute to the spectrum. The comparison of results from VPSIC calculations with experiment is satisfactory, especially after we account for the effects of spin disorder, which does not close the fundamental gap but suppresses the intensity of the fundamental transition. GGA+U and HSE at the standard values of their internal parameters overestimate drastically the fundamental gap, hence the conclusion that their corrections to the position of the flat Cu *d* bands should be more “screened” than they are. On the other hand, the corrections to local- or semilocal- functional eigenvalues provided by VPSIC are close to those of non-self-consistent one-shot GW, suggesting that the "beyond-local" correlation is described by VPSIC with similar accuracy.

7. Ga_2O_3

This Chapter provides our contribution to that field of research which deal with Transparent Conducting Oxides, labeled as TCOs. This class of materials exhibits both transparency and electronic conductivity at the same time. Due to this key feature, these materials have found widespread use in many technological applications, such as displays, low-emittance windows, electrochromics, photovoltaics and flexible electronics, where, they are exploited mostly as transparent contacts. In the last decade an increasing number of research groups have dedicated their studies on TCOs materials, suggesting both new materials and approaches. This interest is pushed mainly by an always increasing demand in various areas for electronic devices with enhanced performances, based on *green* materials and processing, and higher efficiency. Contrary to what we may believe, since the long history in the application of TCOs, a complete theoretical understanding is not still achieved nor a reliable way of prediction of the properties of new materials. This occurs especially in amorphous mixed metal oxide TCOs materials, where the basic transport physic has not been understood yet, although they are very promising from the experimental point of view.

Currently, just a few TCOs material dominate the scene in industry. Mostly, they are a small set of oxide materials such as SnO_2, In_2O_3, InSnO, and ZnO. For example, the Fluorine-doped tin oxides (SnO_2:F) is the most used in production of energy efficient windows, where the tin oxide coatings increases the efficiency in preventing radiative heat loss, yielding the thermal emittance from ~ 0.84, for uncoated glass, to $\sim$0.15. The Indium-Tin-Oxide (In_2O_3:Sn, mostly known as ITO) is present in the majority of flat panel display applications as transparent electrode. More recently, amorphous In-Zn-O has become a possible replacement.

Although, TCOs are predominantly n-type material, one of the current research challenge in TCOs field is that of the development of p-type materials with comparable conductivities to their n-type counterparts. In fact, those p-type materials observed exhibit stability problems and they are difficult to reproduce. The other open research area just begun is that of amorphous TCOs materials, that is experimentally well promising, but it is much harder to be accessed by the theory, since its well-known difficulties to approach non periodic materials.

We refer to the book “Handbook of Transparent Conductors“ for a complete review on TCOs materials [67].

7.1. Theoretical and experimental investigation of optical absorption anisotropy in $\beta - \mathrm{Ga_2O_3}$

In the following section, it is reproduced the paper (to be published) about the work developed in collaboration with Prof. Fornari experimental research group, at the University of Parma, about an investigation of optical absorption anisotropy in $\beta-\mathrm{Ga_2O_3}$. The entire theoretical part was developed by me with the support of my supervisor. Briefly, polarized optical absorption measurements were carried out on bulk $\beta-\mathrm{Ga_2O_3}$. The bandgap edge is seen to be a function of light polarization and crystal orientation, with the lowest onset occurring at polarization in the ac crystal plane around 4.5-4.6 eV; polarization along b unambiguously shifts the onset up by 0.2 eV. Theoretical analysis, performed using different advanced computation methods, clearly indicates that the shift of the b onset is due to a suppression of the transition matrix elements of the three top valence bands at Γ point.

7.1.1. Introduction

The semiconducting sesquioxides, and among them $\beta-\mathrm{Ga_2O_3}$, have been employed as transparent conducting oxide (TCO) electrodes in fabrication of solar cells, displays, electronic, and opto-electronic devices for several decades [[174, 175, 176]]. The interest was confined to such application as the conductivity of these metal-oxides was invariably n-type, and attempts to effectively dope p-type failed. The key requirements of TCO electrodes are indeed high electrical conductivity and good transparency, while crystallographic perfection is a minor issue. Furthermore, for a long period no high-quality substrates and epilayers were available, which in turn impeded the development of a truly full-oxide electronics. Recently, $\beta - \mathrm{Ga_2O_3}$ has attracted renewed attention, as large single crystals [[177, 178, 179]] and high-quality homo- and hetero-epitaxial layers became available [[180, 181]], which paved the way to novel application areas, namely: substrates for GaN-based LEDs [[183, 184]] and high-power transistors [[185, 186]]. As in many previous cases, this technological breakthrough triggered much research on the fundamental materials properties, which in turn produced improved materials. Some basic properties of the most stable β phase of $\mathrm{Ga_2O_3}$ are known with a good degree of confidence. Its crystallographic structure, for example, belongs to the monoclinic system (space group C2/m) with lattice constants a = 12.23 Å, b = 3.04 Å, c = 5.08 Å, and an angle γ=103.73° between a and c [[174, 175, 187]]. With regard to optical and electronic properties, first-principles calculations and Angular-Resolved Photo-Electron Spectroscopy (ARPES) [[188, 189, 190, 191]] concur that the minimum gap is between the Γ point of the conduction band and the (quasi) M point of the valence band. However, being the valence band top quite flat, the difference between the valence maxima at M and Γ is only a few meV. Thus, the effective near-edge optical behaviour is, essentially, that of a Γ direct-bandgap material, with anisotropic valence bands and largely isotropic conduction band. The rather scattered band gap values of bulk $\mathrm{Ga_2O_3}$ measured by optical absorption (from 4.5 to 4.9 eV), see for example [[179, 192, 193]], indicate that in many of the previous literature reports the effect of bandgap anisotropy and sample geometry was not critically considered. This is quite surprising given the pioneering work of Matsumoto et al. [[194]] in 1974, followed by a reappraisal in 1997 by Ueda et al. [[195]]. The principal motivation to the present work was indeed to clarify in what way the optical properties of bulk $\beta - \mathrm{Ga_2O_3}$ are affected by the valence band structure. Accurate optical absorption experiments were carried out, also on unexplored crystal orientations, and critically discussed in view of the results of ab initio computation. With respect to papers [[194, 195]], new experimental data and a physical interpretation of the optical anisotropy are provided.

7.1.2. Experimental and theoretical methods

The samples investigated in this work were (010) and (-201)-oriented wafers grown by Edge-defined Film Fed Growth at Tamura Corporation. They were nominally undoped (carrier concentrations 2.4 and 1.7 10^{17} cm^{-3} respectively) and 0.65 mm thick. Polarized absorption was measured at room temperature and normal incidence in the 800-200 nm range by means of a Varian 2390 spectrophotometer and a Glan-Taylor polarizer. As described further below, we oriented the electric field vector E parallel to the crystallographic axes a, b, and c. It must be noted that what is denoted for simplicity E||a is actually the direction orthogonal to the bc plane, which indeed is 13° away from a. We also performed measurements on Sn-doped samples ($1.0 - 3.2x10^{18}\, cm^{-3}$) and found that the absorption edges are comparable to those of the undoped counterparts, as long as the same geometry set-up is employed. Therefore, the following discussion will focus on the results obtained on undoped $\beta - \mathrm{Ga_2O_3}$.

To interpret and support the experimental results, ab initio calculations using several density-functional-related methods were performed. Specifically, hybrid (HSE) [[196]] and self-interaction corrected (VPSIC) [[132, 56]], GGA (generalized gradient) and LDA (local density) functionals, and many-body perturbation theory in the non-self-consistent G_0W_0 and self-consistent-Green's-function GW_0 [[197]] approximations were used. HSE and GW are the VASP-PAW implementations [[84, 210]]. The level of agreement with experimental data was generally good, always well within 10% and down to 2% on the absolute values of the gap. Confirming recent results on magnetic Mott insulators [[199]] the best performance in comparison with experiment is that of VPSIC. The technical ingredient were essentially standard [[200]].

7.1.3. Results and discussion

Figure 7.1 reports the spectra obtained for nominally undoped $\beta{-}Ga_2O_3$ at normal incidence on the (010) surface with polarizations E||c and E||a. Correspondingly, absorption edges at 4.54 and 4.57 eV were observed. The absorption anisotropy between E||c and E||a is thus only 0.03 eV. However, the picture changes drastically as we consider an orientation whereby E||b.

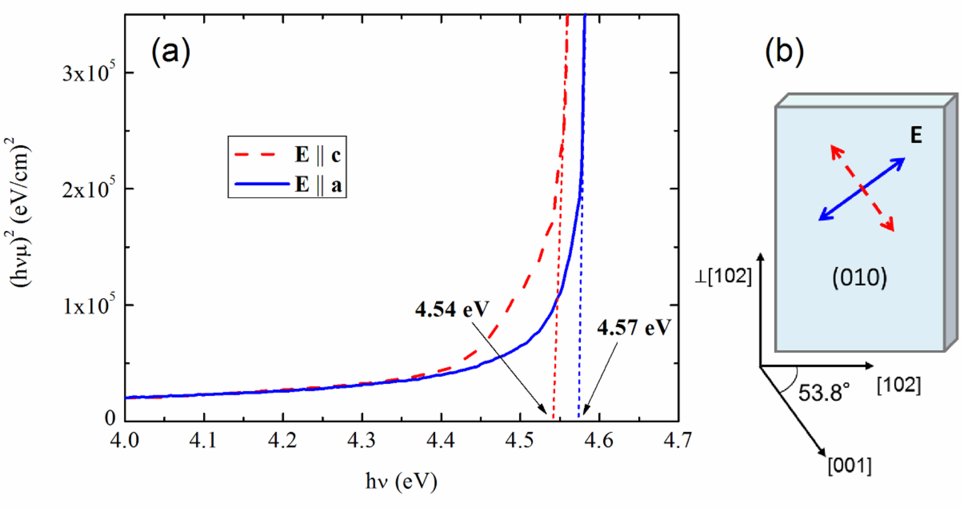

Figure 7.1.: Absorption spectra of a (010) sample at normal incidence for polarization E||c and E||a, respectively (a), and schematic of sample orientation, axes, and polarizations (b).

In Figure 7.2 we report spectra obtained on a (-201) oriented sample; in this crystal orientation, it is easy to probe the E||b configuration as well as E||[102] (clearly b⊥[102]). The E||[102] absorption edge at 4.52 eV is in line with those just reported for c and (quasi) a polarization, as expected from [102] being a combination of the a and c vectors. However, the onset of the absorption for E||b is at 4.72 eV, that means 0.2 eV higher in energy. This is a direct evidence for anisotropy and confirms the previous observations in [[194, 195]].

Summarizing the experimental results, the lowest absorption edge at 4.54 eV is for polarization E||c, followed by the close 4.57 eV onset when E||a, while E||b gives a clearly separated 4.72 eV. In Figure 3 we report the absorption coefficient μ predicted by VPSIC-GGA at the experimental volume and internal coordinates relaxed according to quantum forces. It is plotted in Tauc form with exponent 2 as the data in Figs. 7.1 and 7.2, so that it linearizes for a direct dipole-allowed gap (the direct gap at Γ is indeed almost identical to the indirect minimum gap, which is invisible in absorption on the intensity scale of the direct transition). The edge of the absorption is obtained by linear extrapolation of $(h\nu\mu)^2$ to zero absorption. μ is obtained in the standard way from the calculated imaginary part of the frequency-dependent dielectric tensor. The latter is almost diagonal, but

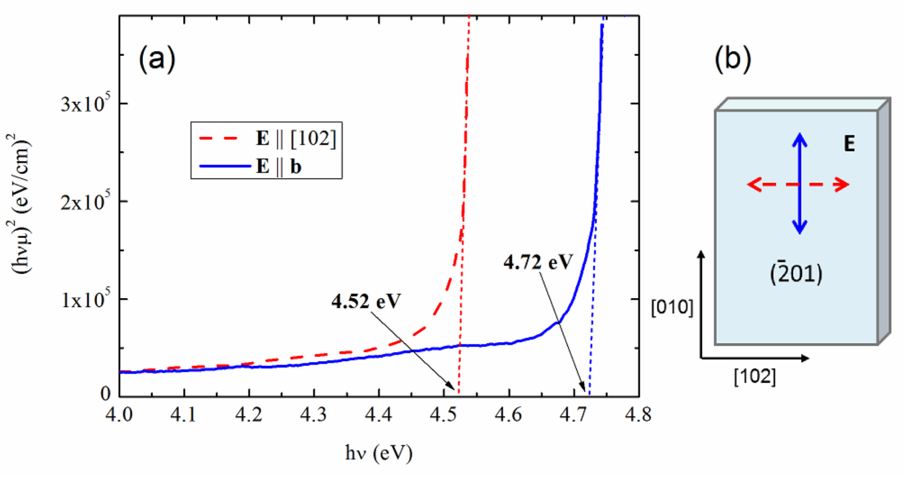

Figure 7.2.: Absorption spectra of a (-201) sample with polarization E||b and E||[102], respectively (a), and schematic of sample orientation, axes and polarization (b).

sizably anisotropic due to the low symmetry of the crystal.

Clearly, there are distinct absorption edges as function of polarization, and their energetic order is E||c < E||a < E||b, in agreement with experiments. For E||c the onset is at 4.65 eV compared to experimental 4.54 eV: 2% off is an excellent result for the standards of ab initio theory, which may miss gap values by as much as 100%. For E||a the onset is higher by just 0.1 eV, vs the 0.03 eV observed experimentally (see Fig.7.1), again a very satisfactory result, also considering the actual orientation for the a axis. For E||b, the onset is 0.5 eV higher than for E||c, again in satisfactory agreement with experimental data (Fig.7.2). Although the VPSIC theoretical results are able to reproduce well the experimental data, we have to note that experimental results are systematically a bit lower than theoretical predictions. This discrepancy could be related either to the earlier absorption onset typical of optically thick samples, which ultimately may lead to a slight underestimation of the bandgap edges, or to computation accuracy or to both factors. In Figure 7.4 we reported the direct gap obtained by all the computation methods employed vs the crystal cell volume. Some considerations have to be made when looking at the data presented here. First, theoretically predicting the crystal cell volumes has always some inherent uncertainty (in this case VPSIC provides the

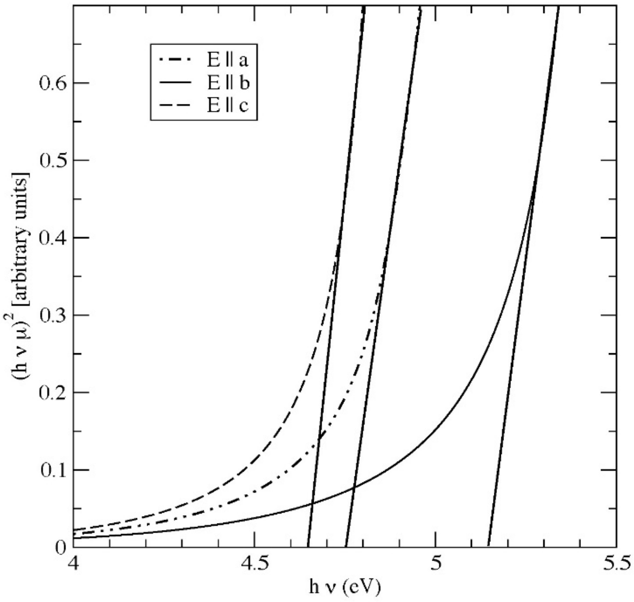

Figure 7.3.: Tauc plot of the absorption coefficient, showing the polarization-dependent onsets.

volume closest to experiment). Secondly, the dependence on microscopic structural details is modest (VPSIC eigenvalues in the experimental and GGA cells are almost identical). Finally, the pressure derivative of the gap extrapolated from the data is 3 meV/kbar, in line with previous reports [[201]]. The agreement with experiment is overall reasonable. Partially self-consistent GW0 is closest to experiment and VPSIC, which is in itself an interesting theoretical finding.

As a final point, it must be observed that the apparent upward shift of the onset for E||b stems from a suppression of the matrix elements for the transition from the top valence bands. The absorption is proportional to $|e \cdot P_{vc}|^2$, where e is the polarization and $P_{vc} = (< P_a >, < P_b >, < P_c >)$, where e.g. $< P_b >$ is the matrix element between valence and conduction states of the momentum component P_b along the b axis. A smaller $< P_b >$ implies weaker absorption for E||b. In Figure 5a we show the matrix elements along the three axes at the Γ point, along with relevant bands and wavefunctions. Clearly $< P_b >$ from the top three valence bands is essentially zero, and this causes the suppression of the absorption. The reason is that the initial and final wavefunctions sketched in Fig. 5b have the

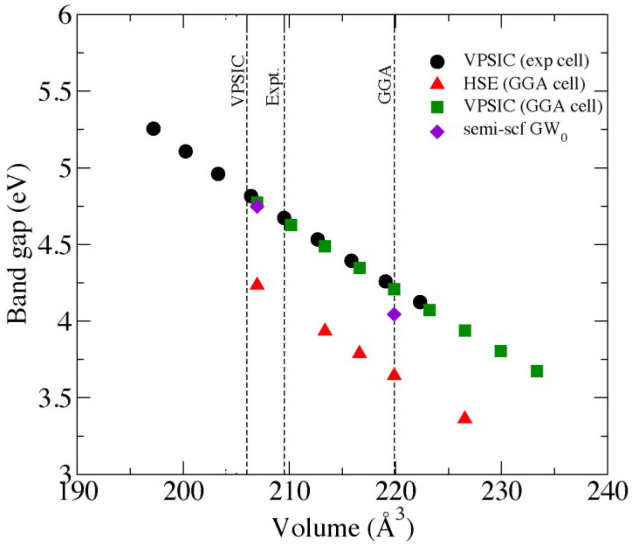

Figure 7.4.: Gap vs volume as obtained from hybrid and self-interaction corrected functionals, as well as from GW0 many-body perturbation theory. The line Exp marks the cell volume obtained from experimental lattice parameters [[174]].

same parity along b, and therefore the matrix-element integral is zero [[202]] (in addition, the valence states have a very small amplitude). The recovery of the matrix element at the fourth-from-top band below the valence top shows that the anisotropy shift is essentially the distance of that specific band from the valence top.

7.1.4. Conclusions

In conclusion, the theoretical analysis (especially as provided by the VPSIC method) of optical absorption results on (010)- and (-201)-oriented $\beta - Ga_2O_3$ samples oriented provides a physical interpretation of the absorption anisotropy phenomena. With respect to previous experimental reports, this work also included measurements with polarized light along unexplored crystal orientations. The lowest absorption onset was at about 4.55 eV in (010)-oriented wafers. In this case, whatever the polarization on the ac plane, only minor shifts of the bandgap were found. For (-201)-oriented samples, light polarization along b has the strongest effect as it

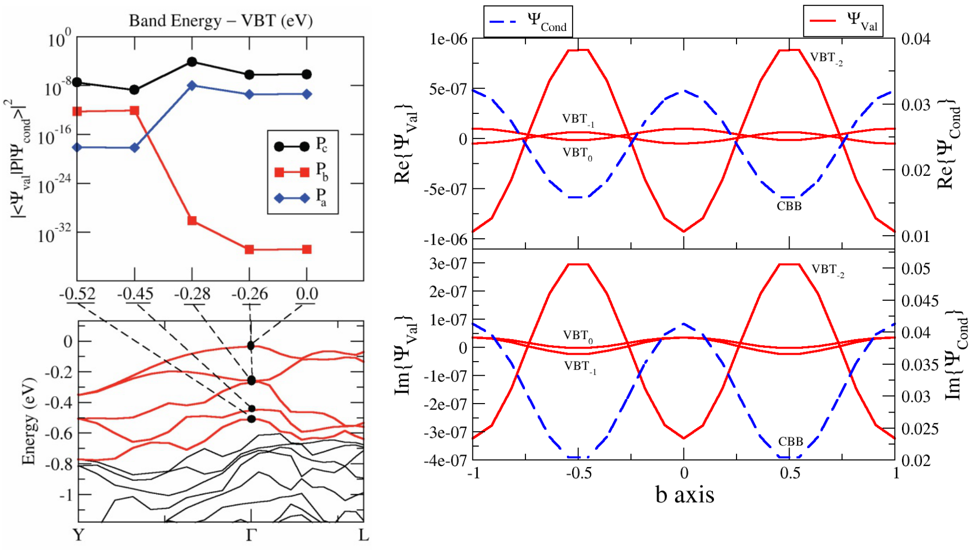

Figure 7.5.: (left) Matrix element (top) along the crystal axes vs energy from valence top, and bands near the valence top. Along b the matrix element is suppressed (note the log scale). The bands show that the anisotropy shift of the E||b onset is related to the distance of the top to fourth-from-top bands. (right) Along b the Γ-point wavefunction $\Psi(n, y; x = z = k = 0)$ of the three top valence bands are very small, and have the same parity as the conduction band (real part: top; imaginary part: bottom; note the different scales).

shifts the absorption edge towards higher energy by 0.2 eV. For this specific case, the theory indicates that the large shift is actually due to suppression of the transition matrix elements of the three top valence bands.

7.2. Structure and gap of low-x $(Ga_{1-x}In_x)_2O_3$ alloys

Here, it is reproduced the conference proceeding [167] where we study the electronic and local structural properties of pure and In-substituted β-Ga_2O_3 using density functional theory. Our main result is that the structural energetics of In in Ga_2O_3 causes most sites to be essentially inaccessible to In substitution, thus limiting the maximum In content to somewhere between 12 and 25 \% in this phase. We also find that the band gap variation with doping is essentially due to “chemical pressure", i.e. volume variations with doping. As second author of this paper, I have only supported the first investigator in the preparation of calculations and during the analysis of results.

7.2.1. Introduction

Ga_2O_3 is attracting interest recently as a material for high-power transport and ultraviolet optical absorbers, owing to its wider band gap and larger electric breakdown voltage compared to e.g. GaN. Combined with In_2O_3 (already widely used as transparent conducting oxide), Ga_2O_3 originates a new materials system which is tunably insulating, easily n-doped (not so easily p-doped), and potentially magnetic (as In_2O_3 can be made ferromagnetic [159] through magnetic doping, the same may well apply to Ga_2O_3). Further, the band-engineering and nanostructuration concepts from popular semiconductor systems such as, e.g., AlGaAs or InGaN may be exported to these materials, and thus to a whole new region of high absorption energies and breakdown voltages. This may enable the design of devices based on $Ga_2O_3/(Ga_{1-x}In_x)_2O_3$ such as high-power field effect transistors and far-UV photodetectors or emitters.

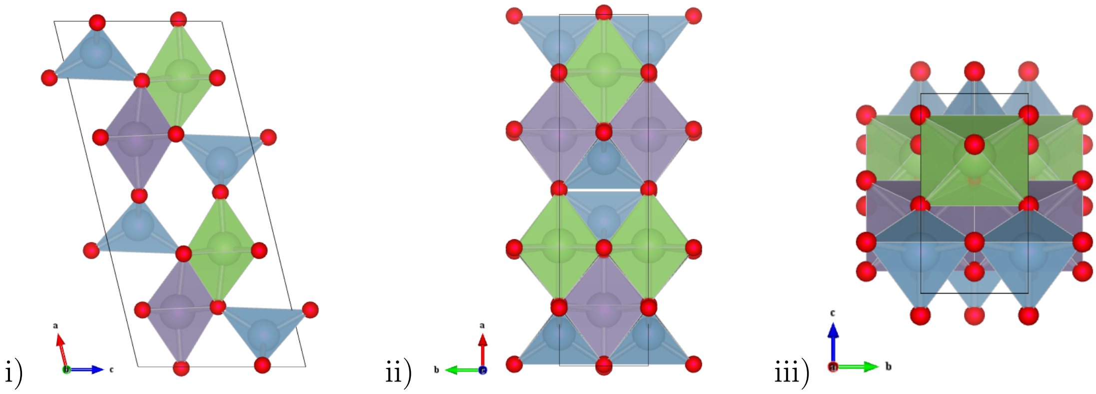

Figure 7.6.: Monoclinic β-Ga_2O_3 viewed along the b-axis (i), c-axis (ii) and a-axis (iii). The structure can be seen as a collection of zigzag double chains of edge-sharing GaO_6 units (violet and green Ga-octahedra) linked by single chains of vertex-sharing GaO_4 (blue Ga-tetrahedra).

7.2.2. Ga_2O_3

Gallium oxide, Ga_2O_3, exists in various polymorphs, the most stable being monoclinic β-Ga_2O_3 at ambient condition [164]. The monoclinic phase, shown in Figure 7.6, belongs to the C2/m space group. The unit cell contains 20 atoms, with two crystallographically nonequivalent Ga atoms in tetrahedral and octahedral like coordinations in the lattice. Geometry and volume optimizations as well as electronic structure calculations have been done using density-functional theory (DFT) in the generalized gradient approximation (GGA), and the Projector Augmented-Wave (PAW) method as implemented in the VASP code [210]. The bulk Brillouin zone is sampled on a 4×8×6 Monkhorst-Pack grid. The calculated lattice parameters compare well with experiment [166] (in parenthesis): a=12.46 Å (12.23), b=3.08 Å (3.04), c=5.88 Å (5.80), θ=103.65° (103.7).

The band structure of Ga_2O_3, similarly to other binary Ga compounds, has mainly O 2p character in the upper valence band and Ga s content in the bottom conduction band. The direct gap appears at the Γ point. GGA underestimates it at about 2 eV, as expected of semilocal functionals. Adding an empirical self-energy correction [173] involving the high-frequency dielectric constant, we obtain a gap of 4.2 eV, not far from the experimental range of 4.5-5 eV [160, 162].Surprisingly, the precise value of the gap is still uncertain even in recent work [162]. The reason for this is probably the significant anisotropy of the absorption, which we have analyzed (and will report elsewhere [172]) with hybrid-functional, pseudo self-interaction corrected, and GW_0 many-body perturbation-theory calculations (known to be free of the typical LDA/GGA gap errors). For the present purposes, we just note that these advanced methods confirm that a direct minimum gap at zone center between 4.2 eV (hybrids) and 4.7 eV (self-interaction-correction), and also confirm the pressure derivative of the gap to be 3 meV/kbar essentially as in GGA (see below).

7.2.3. Low-In-content alloying

Because unalloyed In and Ga oxides have different structures (bixbyite and monoclinic β, respectively) the high-In and low-In-content alloying limits will behave quite differently, and at intermediate concentrations the two phases are likely to mix in an complicated way. The experimental alloying of Ga_2O_3 with In_2O_3 indeed faces significant limitations [162], with β-Ga_2O_3-like and bixbyite-like X-ray spectra at low x and high x respectively, and a mixed-phase region at midrange x. In particular the β-Ga_2O_3-like phase persists only up to about 15% or so [162]. Thus, keeping in mind that the large-x end of the alloying spectrum will have to be treated differently, here we tackle the low-x end substituting In for Ga in β-Ga_2O_3 at nominal concentrations of 3, 6, 9, and 12 % (one to four In atoms per 80-atom or 32-cation supercell). Our results naturally suggest an interpretation for the observed behavior. We optimize (in volume, shape, and internal coordinates) supercells of Ga_2O_3 with In→Ga substitutions sampling some of the various possible octahedral and tetrahedral sites and combinations thereof as function of composition (i.e. In concentration). The supercells contain 1×2×2 unit cells (80 atoms), so we an approximate backfolding (4×4×2) of the bulk k-point grid. The calculations at 3% In (one "isolated" In atom per 80-atom cell) show that In only substitutes octahedral Ga: tetrahedral sites are ruled out by a huge excess energy cost of 1.1 eV. Therefore, half the cation sites are essentially inaccessible to In, and hence the amount of In that can actually be incorporated into Ga oxide is automatically halved – to put it differently, all available sites would be occupied already at 50% nominal In content. Even reaching this limit, though, is quite

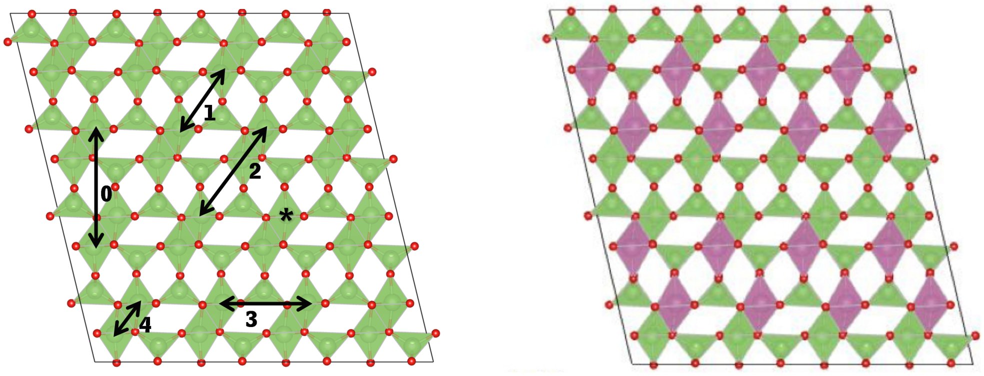

Figure 7.7.: Left: different pairings patterns of In in Ga$_2$O$_3$. Right: structure of the 12% sample.

unlikely. Indeed, In incorporation is not arbitrary in terms of configuration. At 6% In content, i.e two In atoms per supercell, one can estimate the energetics of pairing (or, rather, non-pairing) of In in Ga$_2$O$_3$. In Figure 7.7, left, we display the preferential couplings. The energy of configuration '0' is chosen as zero; the structures numbered '1' to '4' are in progressively unfavorable energetic order, with '1' at 16 meV, '2' at 50 meV, '3' at 100 meV, '4' at 125 meV. In the configuration labeled '*', In atoms occupy adjacent octahedra; this structure is 250 meV higher than the '0'-configuration. Clearly, In atoms tend to avoid one another, and it is likely that at the common growth temperatures of 850 K the typical configurations will be such as our '0' and '1' above. Inspecting the structure, this suggests that well below a half, and probably closer to a quarter, of the octahedral sites can be occupied by In with a reasonable energy cost; when these are filled, the formation of some mixed β/bixbyite phase may be preferable to substitution in the β phase. This brings the effective solubility in the original β-Ga$_2$O$_3$ structure down to between 12% and 25% as found in experiment [162]. Consistently with the above configurational restrictions on pairing, the admissible arrangements at 9% and especially 12% In content are few. For example, the structure used at 12% is in Figure 7.7, right. The resulting structures are probably a fairly decent model of the alloy, given the very limited configurational freedom of In already at these concentrations. (Cluster-expansion work is ongoing on miscibility at finite temperature and will be reported elsewhere.) We calculated the gap and the vol-

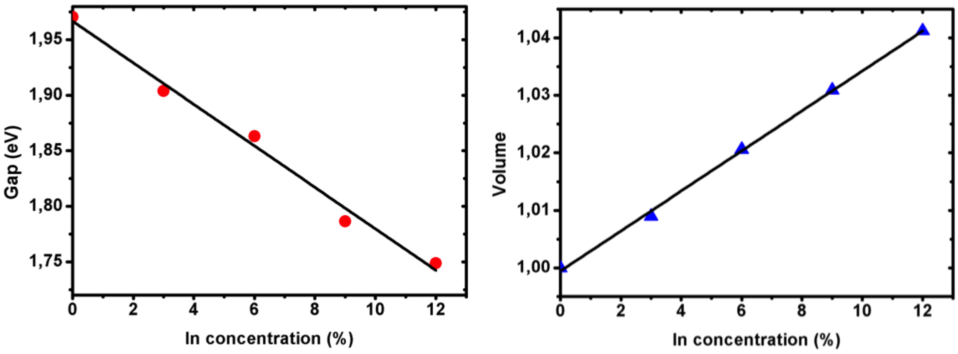

Figure 7.8.: Left: direct gap at zone center as function of In concentration. Right: normalized volume of In-doped Ga_2O_3 as function of concentration.

ume change with concentration of $(Ga_{1-x}In_x)_2O_3$ in the 80-atom supercell for the structures mentioned. The gap is in Figure 7.8, left, and the volume is in the same Figure, right. Although the gap is underestimated (a token of using GGA), its concentration change of 17 meV/% is quite similar to 20 meV/% experimentally [162]. Using the the volume change with x and the bulk modulus, we can evaluate the concentration derivative as a pressure derivative, obtaining 2.5 meV/kbar. This is similar to the Ga_2O_3 value of 3 meV/kbar [172, 161], which suggests that the gap is mainly affected by volume change, and marginally by other factors. In this light, the agreement with experiment therefore falls in line with expectations from previous work [171].

7.2.4. Conclusions

In summary, we have performed first-principles DFT-GGA calculations on the electronic and local structural properties of In-containing Ga_2O_3. The energetics of In in Ga_2O_3 limits the maximum In content to somewhere between 12 and 25 %. We also find that the gap variation with doping is essentially due to “chemical pressure", i.e. volume variations with doping.

7.3. Low In solubility and band offsets in the small-x β-$Ga_2O_3/(Ga_{1-x}In_x)_2O_3$ system

In the following, I reproduce our recent publication [55] where, based on first-principles calculations, we show that the maximum reachable concentration x in the $(Ga_{1-x}In_x)_2O_3$ alloy in the low-x regime (i.e. In solubility in β-Ga_2O_3) is around 10\%. We then calculate the band alignment at the (100) interface between β-Ga_2O_3 and $(Ga_{1-x}In_x)_2O_3$ at 12%, the nearest computationally treatable concentration. The alignment is strongly strain-dependent: it is of type-B staggered when the alloy is epitaxial on Ga_2O_3, and type-A straddling in a free-standing superlattice. Our results suggest a limited range of applicability of low-In-content GaInO alloys. As second author of this paper, I have only supported the first investigator in the preparation of calculations and during the analysis of results.

7.3.1. Introduction

The wide-band gap and large-breakdown-voltage insulator Ga_2O_3 is attracting interest for high-power transport, transparent electronics, and ultraviolet sensing applications. Combined with In_2O_3 (already widely used as transparent conducting oxide), Ga_2O_3 may originate a new $(Ga_{1-x}In_x)_2O_3$ materials system enabling the band-engineering and nanostructuration concepts from popular semiconductor systems (such as, e.g., arsenides and nitrides) in a previously impervious region of high absorption energies and breakdown voltages. In this Letter we provide two key pieces of information for this endeavor, namely the maximum concentration of indium in the alloy and the interface band offset, which are hitherto unknown to our knowledge. We first address the degree of miscibility of Ga_2O_3 and In_2O_3. The parent materials have different structures (monoclinic β and cubic bixbyite, respectively), so the low-In and high-In-content alloying limits will be different, with likely complicated phase mixing at intermediate concentrations [162, 163].

7.3.2. Solubility of In in Ga_2O_3

Here we consider the alloying of β-Ga_2O_3 with In, and show, based on ab initio calculations, that In can be incorporated into β-Ga_2O_3 at most at the 10% level at typical growth temperatures. This agrees with the most recent estimate [163] of around 10%. We then address the band offsets at the (100) interface of β-Ga_2O_3 to the $(Ga_{1-x}In_x)_2O_3$ alloy, both epitaxial on Ga_2O_3 and free-standing. Given that x is at most around 10%, we study the offset in the computationally-affordable case of 12% In. We find that the alignment is of type-B staggered when the alloy is epitaxial on Ga_2O_3, and type-A straddling in a free-standing superlattice. Alloying of monoclinic β-Ga_2O_3, the stable phase at ambient condition [164], is simulated by substituting Ga with In at various nominal concentrations and configurations. The interface is then simulated by a superlattice supercell. All optimizations (internal geometry, volume, etc.) and electronic structure calculations are done within density functional theory (DFT) in the generalized gradient approximation (GGA), and the projector-augmented wave (PAW) method as implemented in the VASP code [210]. The PAWs include occupied d states in the valence for both cations. For the alloy calculation we use an 80-atom (32-cation) supercell containing 1×4×1 20-atom conventional cells, and for the interface calculation a 160-atom (32-cation) 2×2×2 supercell. The k-point sampling is on a 2×4×2 grid. We work at the calculated lattice parameters a=12.46 Å, b=3.08 Å, c=5.88 Å, θ=103.65°, which compare well with experiment [166, 167]. We choose as dilute limit the concentration of 3% In, i.e. one “isolated" In atom per 80-atom cell. Besides being computational feasible, 3% is actually a quantitatively accurate dilute limit: the formation energy calculated in the standard way [168] is $E_f(1)$=0.24 eV/In, which yields a concentration of 2.7% at the typical growth temperature T_g=775÷800 K [162, 163]. The chemical-potential reservoir for In is the bixbyite phase of In_2O_3, which might occur in nanograins embedded in Ga_2O_3. Indium substitution at tetrahedral sites costs δE_t=1.1 eV more than at octahedral sites; thus the tetrahedral-site occupation probability is lower than that of octahedral sites by a factor $\exp(-\delta E_t/k_B T_g)\sim 0.5\text{-}1\times10^{-7}$. Therefore, the In concentration in Ga_2O_3 cannot exceed the value whereby the octahedral sites are all occupied, i.e. 50%. Because the Ga_2O_3 structure is made up of double rows of octahedra

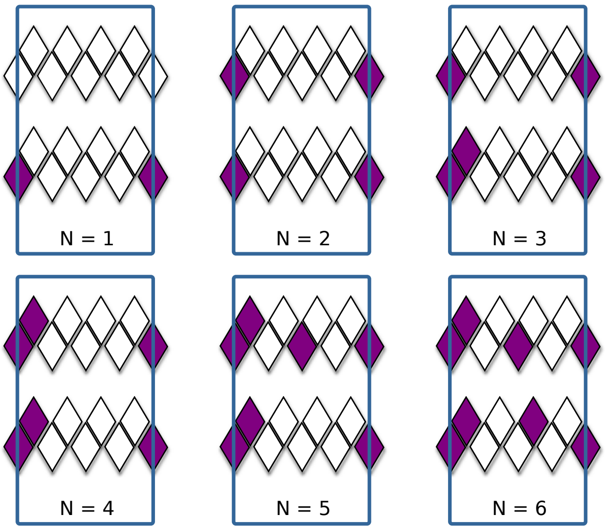

Figure 7.9.: Sketch of different configurations of In on the Ga_2O_3 simulation supercell. Occupied octahedra in the β structure double-rows are darkened.

sharing sides and connected by tetrahedra, there is limited configurational leeway for In placement in the system (see Fig.7.9; for a more realistic depiction see e.g. Ref.[167]). We evaluate the energetics of In substitution in various configurations (a sample is depicted in Fig.7.9) at concentrations between 6% and 25%, i.e. for 2 to 8 In atoms in the 80-atom, 32-cation 1×4×1 cell, and extrapolate numerically to 16 atoms per cell (tetrahedral sites are neglected). We find that two In's prefer to sit on different double-rows or, failing that (as inevitably is the case for growing x), on first-neighbor octahedra in adjacent subrows, which locally resemble the native In_2O_3 bixbyite structure. The formation energy per In decreases slightly for two and three In per cell, then increases steadily. For the configurations in Fig.7.9 we find that the excess formation energies over that of a single In are $\delta E_f(2)$=–0.044, $\delta E_f(3)$=–0.019, $\delta E_f(4)$=+0.021, $\delta E_f(5)$=+0.074, $\delta E_f(6)$=+0.144, $\delta E_f(7)$=+0.171, $\delta E_f(8)$=+0.180, in eV/In (the last two are not shown in the Figure). The cell is kept at the volume of the undoped material, which is strictly correct in the dilute limit [169]; at higher concentration we account for an enthalpic energy cost (see below). The concentration is evaluated as the thermal average of the In population in the supercell (M=32 cation sites)

$$x = \frac{\langle N \rangle}{M} = \frac{1}{M} \frac{\sum_{N=1}^{M} N \exp\left[-\beta_g F(N)\right]}{\sum_{N=1}^{M} \exp\left[-\beta_g F(N)\right]}, \tag{7.1}$$

where β_g=$1/k_B T_g$ and $F(N)$=$E_f(1)$+$\delta E_f(N)$–$T_g S$+δH is the free energy per In in the N-In substituted cell. E is the formation energy, S the formation vibrational entropy (we estimate it from the Debye temperature of the two bulk oxides, and find $T_g S \simeq 0.015$ eV), and $\delta H \simeq 0.09$ eV is the energy cost related to the internal pressure building up in the constrained cell. δH is estimated as the energy difference (per In) between the constrained and volume-relaxed cell; if cell-length changes are allowed along a given direction, as would occur in epitaxy, δH decreases by about one third. In any event, as we have seen, entropy and enthalpy provide only small corrections over the structural energy E_f discussed above. The thermal population average, Eq.7.1, gives a concentration of 9%, with an error bar of +2% and –1% estimated varying the δE's between 0.5 and 1.5 times those calculated. Again, this low solubility follows from tetrahedral sites being ruled out and from In occupying only about 3 out of 16 octahedral sites in the cell on (thermal) average.

7.3.3. Interfaces

Having established the small solubility of In in Ga_2O_3, we come to the band offsets. The correct way of calculating band offsets [170] is as the sum $\Delta E_b + \Delta V$ of the interface jump ΔV in electrostatic potential between the two regions being interfaced, and the difference ΔE_b of the band edge of interest in each of the two materials, taken separately each in their own internal potential. As mentioned, we use a 2×2×2 160-atom cell, depicted in Fig.7.10, upper panel, to describe the (100) interface: half of the supercell along the (100) axis is pure Ga_2O_3, and the other half is a Ga-In alloy. We pick the concentration of 12% as it is near the maximum achievable (as discussed previously), and because, given the energetics constraints, the configurational freedom of In is very limited, and there is no serious need for a detailed In configurations sampling, which would be computationally unfeasible. We choose the (100) interface for computational convenience; it remains to be assessed how much the offsets change with orientation. This super-unit cell repeats periodically the two layers, effectively producing a superlattice; we find that the thickness of the layers is sufficient to reproduce identifiable bulk regions on either side of interface, with flat, bulk-like average potential, as shown in Fig.7.10, lower panel. We study this superlattice in two strain states, epitaxial and free-standing; in the former case we fix the lattice constants in the b-c crystal plane and the monoclinic angle to those of Ga_2O_3, and relax the a lattice parameter; in the second case, we optimize all lattice parameters. The internal coordinates are optimized in all cases. As schematized in Fig.7.11, at the (100) interface between Ga oxide and the alloy at 12% In, we find an alignment of type-B staggered when the alloy is epitaxial on Ga_2O_3, and type-A straddling in a free-standing superlattice; the valence offsets from Ga_2O_3 to $(Ga_{1-x}In_x)_2O_3$ are –0.14 eV (Ga_2O_3-epitaxial) and 0.15 eV (free-standing), and the conduction offsets are –0.41 eV (epitaxial) and –0.05 eV (free-standing). This considerable difference is due almost entirely to strain-induced shifts of the valence band maximum (VBM) and conduction

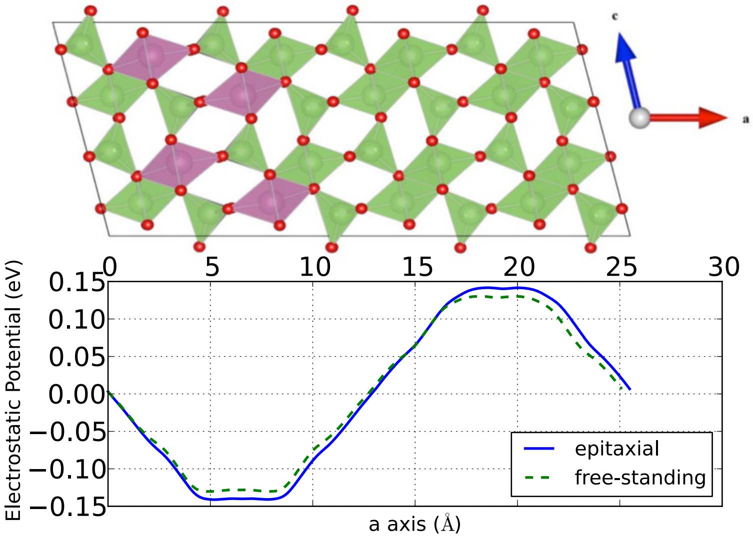

Figure 7.10.: Upper panel: simulation cell for the (100) superlattice (for definiteness we display the epitaxial geometry). Lower panel: the electrostatic potential of the superlattice, showing small but definite bulk regions on either side of the interface. The potential is aligned with the lower side of the cell.

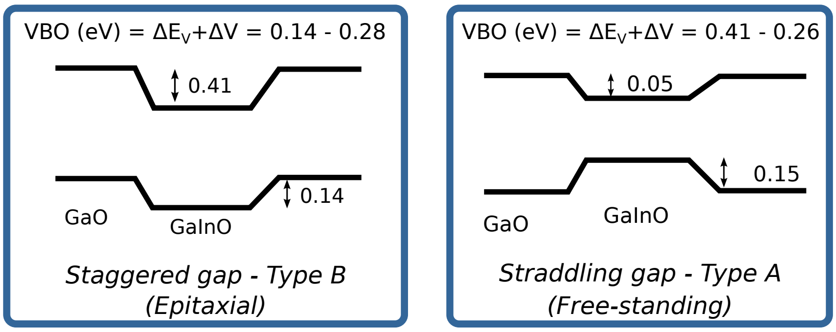

Figure 7.11.: Schematic of the staggered and straddling offset for, respectively, the epitaxial and free-standing superlattice configurations.

band minimum (CBM), whereas the electrostatic interface alignment is hardly insensitive to strain. This indicates that a marked dependence on the strain state, and hence on the growth quality, is to be expected. Importantly, given the limited In solubility, this is about as much of an offset as can be expected between Ga_2O_3 and $(Ga_{1-x}In_x)_2O_3$. There seems to be no measurement of the quantities just discussed, and we hope our prediction will stimulate work in this direction. We expect the above estimate to be rather accurate. Our interface is between materials differing only very slightly due to compositional changes, so that beyond-DFT corrections to the band edges will essentially cancel out; on the other hand, strain-induced band-edge shifts are known to be well described by standard functionals [171]. By the same token, in this case, the gap error also essentially cancels out, so the absolute value of the gap is immaterial to the offsets. For completeness, we mention that the GGA gap is about 2 eV, i.e., as expected, a 60% underestimate compared to experiment [162, 172]. Adding an empirical self-energy correction [173] involving the calculated high-frequency dielectric constant, we obtain a gap of 4.2 eV, not far from the most recent experimental and theoretical beyond-DFT estimates of 4.6 and 4.7 eV, respectively, to be discussed elsewhere [172]. As reported previously [167], the gap rates of change with composition and volume are also close to experiment [162].

7.3.4. Conclusions

In summary, we have performed first-principles calculations on the bulk and interface properties of the Ga_2O_3/ ($Ga_{1-x}In_x$) system. Importantly, we find that In is soluble in Ga_2O_3 only up to a maximum of about 10%. The band offset between Ga oxide and the alloy at 12% In is of type-B staggered when the alloy is epitaxial on Ga_2O_3, and type-A straddling in a free-standing superlattice. The valence offsets from Ga_2O_3 to $(Ga_{1-x}In_x)_2O_3$ are –0.14 eV (Ga_2O_3-epitaxial) and 0.15 eV (free-standing), and the conduction offsets are –0.41 eV (epitaxial) and –0.05 eV (free-standing).

8. A working progress project: XAS in pseudo-SIC taste

8.1. Brief introduction on XAS

In this section we present a brief introduction on the XAS, and on the XANES in particular, from both experimental (briefly) and theoretical point of view.

Wilhelm Conrad Röntgen (March 28, 1845 – February 10, 1923) discovered X-rays and in the same day he detected absorption of X-rays by matter (November 8, 1895). Some days later, he also realized that different materials display different degrees of transparency, as he realized from the famous image of his wife's hand wearing a ring.

Starting from this first and simple observations, the discovery of X-rays have had a big echo because of its applicability but also for their quick expansion throughout the world. Indeed, the transparency noticed by Röntgen found a practical application almost immediately in clinical Medicine: clinical X-rays transparency images made Radiology the most productive diagnostic method to date.

Soon X-rays were also tested in detail for scientific reasons, giving benefit to many and different branches of Science. In particular, we remind the development of a field of X-ray-based research on solid matter that started over half a century after Röntgen's discovery: X-ray Absorption Fine Spectroscopy (XAFS). XAFS is the modern development of X-ray Absorption Spectroscopy (XAS), a branch of X-ray-based Physics that began over ten years later than Röntgen's X-ray discovery, and a couple of years later than X-ray Diffraction (XRD), the first widespread form of application of X-rays for scientific purposes.

At the beginning, the XRD technique had an extraordinary success that overshadowed XAS that was poorly considered or even underestimated for a long time.

Indeed, solid-state research took off thanks to XRD ability to determine the lattice structure of ordered matter. Only during the second half of last century the XAS began to be used where the XRD could nothing, basically in studying amorphous materials, highly disordered systems and liquid solutions. A great contribution to the understanding and the spreading of this technique was given by the recent developed of powerful and brilliant X-ray sources like synchrotrons and storage rings, at one side, and the availability of powerful computers, and computational methods as well, that increase theoretical comprehension of the experimental results.

Nowadays XAFS is considered the best tool to study innovative materials and to assess their technological applications. Different research field are exploiting XAFS method, as solid-state Physics and Chemistry, to investigate new materials; Biology to characterize natural and synthetic biomolecules; and Earth's scientists, to characterize amorphous or even glassy materials. As a proof of that, it is the enormous number of requests for time reaching synchrotron laboratories from industrial and public costumers to have access to one of the X-ray absorption methods. We cite, for example, Mottana and Marcelli review [72] for a full review on XAS.

X-rays are absorbed by all matter through the photo-electric effect. An X-ray is absorbed by an atom when its energy is transferred to a core-level electron which is ejected from the atom. The X-ray absorbing atom is left in an excited state with an empty electronic level, namely a core hole. Any excess energy from the X-ray is given to the ejected photo-electron. With modern XAS technique a fine tuning of the incident photon energy is accessible and allow us to choose both the chemical species of absorbing atom and its core level where the electron is exited from. In Fig. 8.1 the X-ray absorption and different atomic level are schematically represented.

When an electron absorbs the incident X-ray we observe an edge in the resulting spectrum. The edges have different names depending on the core level of exited electron: K and L1 for 1s and 2s level, L2 and L3 for 2p levels, M1 to M5 for 3s to 3d levels, are the most common. The Fig. 8.2 shows the absorption K-edge of a Nickel atom (top) and three L-edges of Eu atom (bottom). As we can see, the structure of these spectra are quite detailed and extends over several hundreds

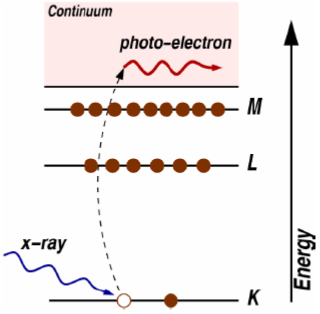

Figure 8.1.: A pictorial view of the absorbing mechanism of a X-ray by the 1s core electron and the relative jump to the continuum.

of eV. This means that different phenomena are involved in the excitation of the electron depending on the energy of incident X-ray. Indeed a separation in two regimes are commonly used: from the pre-edges (-10 eV before the main peak) to the near-edge ($+30 - 50$ eV far from the main peak) is the XANES (X-ray absorption near edge structure) regime; far from the main peak to about the next peak is the EXAFS (Extended X-ray absorption fine structure) regime.

The EXAFS spectrum is the result of the interference effect of the high energy photoelectron the interacts with scattering neighbour atoms. It has seen as a composition of sine waves of different amplitude representative of the different scattering paths undertaken by the photoelectron wave and mathematically described by EXAFS equation:

$$\chi(k) = \sum_j \frac{N_j f_j(k) e^{-2k^2\sigma_j^2}}{kR_j^2} \sin(2kR_j + \delta_j(k))$$

Therefore, starting from the knowledge of photo-electron scattering properties of the neighboring atom, namely the scattering amplitude $f(k)$ and the phase-shift $\delta(k)$, it is possible analyze EXAFS spectra by fitting the experimental data with this equation, providing quantitative information on: distance to neighboring atoms as average bond length R_j, coordination number and type of the neighboring atoms N_j, mean-square disorder of bond length σ_j^2.

From now on, we focus on XANES regime since it has been the object of our

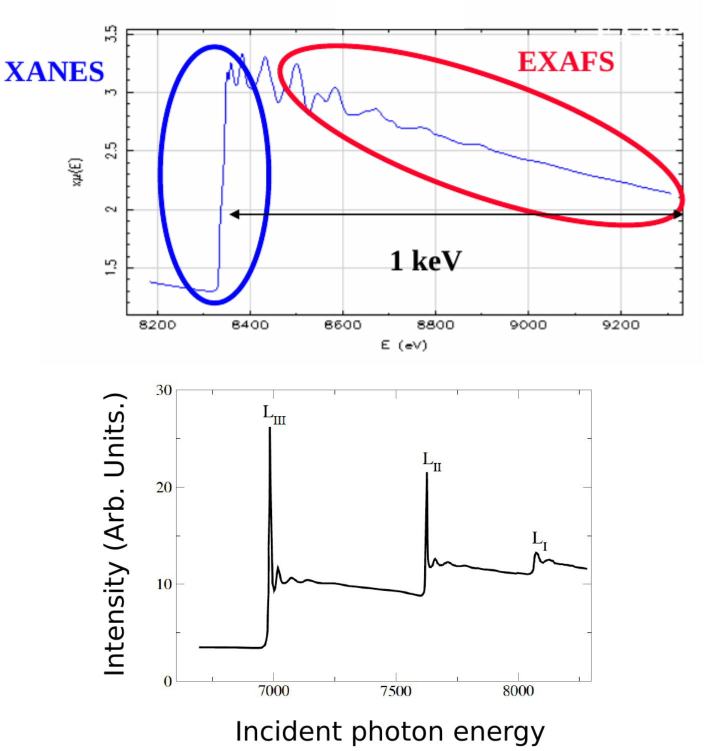

Figure 8.2.: (top) Experimental Ni K-edge spectrum in Ni bulk within a 1 keV wide energy range, where XANES and EXAFS regions of interest are highlighted. (bottom) Three different L-edges in Eu spectrum .

studies.

In the XANES regime we probe the first accessible empty states near the absorbing atom, or in other words we investigate its conduction band structure. Thus, this provides information on the chemistry of the specific atom we are considering, namely the average oxidation state, the local coordination environment and the electronic structure or empty density of states.

More precisely, XANES directly probes the angular momentum of the unoccupied electronic states, irrespective of their nature: bound or unbound, discrete or broad, atomic or molecular. The spectrum is the result of the electronic transition from an initial atomic state to a final not atomic-like state. This transition, as we will see better later, is mainly governed by dipole selection rules $\Delta l = \pm 1, \Delta j = \pm 1, \Delta s = 0$. Thus, in atomistic view, the primary transitions will be from s level to p level ($s \rightarrow p$) for K (1s core electron) and L_1 (2s core electron) edges; from p level to d level ($p \rightarrow d$) for L_2 ($2p_{1/2}$) and L_3 ($2p_{3/2}$) edges. But in a molecular or crystal view the final state is usually not atomic-like and may have mixing, namely a certain amount of hybridization with other orbitals. This is often the interesting part of the XANES, giving us information of the type of bonding formed by probed atom.

Usually the interpretation of XANES spectra is not straightforward and often requires sophisticated theoretical understanding. The XANES spectrum is theoretically accessible via the computation of the absorption cross section. This is given by the Fermi golden rule as a sum of probabilities per unit of time of making a transition from an initial state to an unoccupied final state through an interaction Hamiltonian [73]. Electronic transitions involved in X-ray absorption spectroscopy are mainly governed by the electric dipole operator, and secondly by a quadrupole component. The main difficulty of any absorption cross section calculation lies in the solution of the Schrödinger equation for the final and initial states. The choice of the method used to solve the Schrödinger equation depends on the localized or delocalized character of final states.

Probably the best way to describe the transition is to incorporate core-hole interactions in the two-particle Bethe-Salpeter (BS) equation, as proposed by Soininen and Shirley [74]. Among the other many-body approaches we remind the crystal field multiplet theory [75] which has been widely used with success but it need many adjustable parameters and is extremely time consuming.

However, in the case of K-edge XANES spectra, the core-hole is frozen at one atomic site and the many-particle approach can be reduced to a single particle calculation. Thus the initial state does not represent a big problem, being a simple atomic state. The main problem is how to describe and calculate the final state that includes the exited electron in the conduction bands, the atomic hole and the relaxation of the whole conduction bands structure yielded by the core hole attraction. First attempts to give an interpretation of XANES spectra were made with band structure calculations and local projected densities of empty states (commonly called LDOS) of system without a core hole in the final state. (see for instance Refs. [76]). The importance to include the effect of the core hole was observed by Schwartz and Buenker (1976) [77] that introduce the so called Z+1 method, in which they replace the excited atom by the next element in the Periodic Table to simulate the absence of a core electron. Another way to model the electronic excitation was introduced by Slater [78] (and further works [79]) where half an electronic occupation is promoted from a core state to an excited state. The excitation energy corresponds to the difference between the final and initial state eigenvalues, and includes relaxation effects up to second order. Alternatively one may calculate excitation energies as differences in total energy ΔSCF between the system in which a whole electron is promoted from a core state to an excited state and the system in the ground state. However, straightforward implementation of either the Slater transition state theory or the ΔSCF approach requires doing a DFT calculation for each individual excited state.

Density-functional theory DFT approaches [81, 82, 80] have been successfully applied to K-edges of weakly correlated materials. In a pseudopotential framework, by using supercell approaches, large systems (several hundreds of atoms) can be a priori treated. The charge density for such large cells is easy to calculate self-consistently by using pseudopotentials. In this approach, however, the final state for the XAS cross section is not directly accessible like in the LCAO frameworks [83] where the reconstruction of initial and final state is included in the method itself. Thus, the use of the projector augmented wave PAW [84] method gives a real benefit, because it allows to reconstruct the all-electron wave function and consequently to obtain XAS intensities unaffected by the presence of a pseudopotential. In addition a further problem steam from high number of empty states at many k-points in the Brillouin zone for which the diagonalization of the Hamiltonian has to be done. To tackle this problem a method based on the continued-fraction approach based on the recursion method of Haydock, Heine and Kelly [86, 85] within PAW formalism [80], permits to span XAS spectra up to the far edge region in a calculation time negligible comparing with the calculation time of the self-consistent charge density in large systems. This approach is presented in [80, 91] and we will report it in detail in next sections.

In ab-initio DFT methods, the core-hole interaction is included in a supercell approach by generating a pseudopotential with a core hole in the desired atomic core level and considering the absorbing atom as an impurity, then the relaxed structure is self-consistently calculated. Several methods have been used, strongly dependent on the system under investigation. The most simple one is that does not account for the core hole (None Core-Hole), especially in those compounds where its effect is supposed to be negligible, as in metals. The most common is that accounts for a full core hole in the probed atom (Full Core Hole), but the exited electron is usually removed from the system [81]. This method has been used in those condensed matter where the final state are not too much localized. In the case of small test molecules and clusters, the accounting for half core-hole (HCH) has provided good agreement with experiment [88]. In the XCH description, a full core-hole is generated into the probed atom, but this time the excited electron remains in the self-consistent calculation with the constrain to be in the first conduction band, or during the pseudopotential generation the core electron is located in the first empty atomic orbital. Prendergast and Galli [87] reproduced the XAS spectra of water in different phases, founding a good agreement between their calculated spectra using XCH and the experimental ones. They also compared XCH description with FCH and HCH reporting similar spectra trends in all approaches, but an increase of spectra quality with XCH method especially in the pre-edge region was noted and ascribed to the presence of localized exited electron at low energies.

However, in the presence of moderate or strong correlation DFT methods has two main shortcomings. The first is the unsatisfactory treatment of electron-electron interaction in the DFT functional. The second is the huge kinetic-energy cutoffs of norm-conserving pseudopotentials involved when transition metals and rare earths are studied and the need to simulate large supercells with reduced symmetry that increase much the computational time. A partial remedy for the lack of correlation effects is the use of the DFT+U approximation [89], that has shown to improve the agreement with experimental data in the pre-edge region of correlated 3d transition-metal compounds [90, 91]. For what concern the second problem, in [91] has been developed a modified version of Lanczos procedure suitable for ultrasoft pseudopotentials, since it is known they can be used use with low cutoffs, about 20-40 Ry, also for transition metals and rare-earth compounds, reducing significantly the computational time.

As we have already said in previous sections, since pseudo-SIC approach manage to describe correlated material in a very satisfactory agreement with experiment, we think that could produce accurate XAS spectra likewise.

8.2. XANES calculation in pseudopotential scheme

In the following we report the method to calculate the XAS cross section developed within PAW formalism by M. Taillefumier et al. [80] and its extension to the ultrasoft (US) pseudopotential scheme reported by C. Gougoussis et al. [91]. This extension is of crucial importance for the applicability of this procedure within the pSIC-DFT method, as it is based on US pseudopotentials.

(We will follow almost exactly the previous cited references.)

8.2.1. XAS cross section

In a monoelectronic approach, the X-ray absorption cross section $\sigma(\omega)$ can be written as

$$\sigma(\omega) = 4\pi^2\alpha\hbar\omega \sum_f |M_{i\to f}|^2 \delta(E_f - E_i - \hbar\omega), \tag{8.1}$$

where $\hbar\omega$ is the photon energy, α is the fine structure constant and $M_{i\to f}$ are the transition amplitudes between an initial core state $|\psi_i\rangle$ with energy E_i, localized on the absorbing atom site $\mathbf{R}_0$, and an all electron final state $|\psi_f\rangle$ with energy E_f

$$M_{i\to f} = \langle\psi_f|\mathcal{D}|\psi_i\rangle. \tag{8.2}$$

$\mathcal{D}$ is a transition operator coupling initial and final states. In the electric quadrupole approximation, $\mathcal{D}$ is given by $\epsilon\cdot\mathbf{r}\left(1+\frac{i}{2}\mathbf{k}\cdot\mathbf{r}\right)$, where ϵ and $\mathbf{k}$ are the polarization vector and the wave vector of the photon beam, respectively. Within the frozen core approximation, $|\psi_i\rangle$ is a core state that can be taken from an all electron ground state atomic calculation. In the impurity model, $|\psi_f\rangle$ is an excited empty state that is solution of the Schrodinger equation for a potential that includes a core-hole on the absorbing atom.

8.2.2. PAW formalism

In the following, the transition amplitude of Eq. 8.2 is formulated within the PAW formalism, as originally described by Blochl [84]. We only recall the main aspects of the method that are needed to give a simple expression for the $M_{i\to f}$ terms. Within the PAW formalism, the final state all electron wave functions $|\psi_f\rangle$ are related to the corresponding final pseudo wave functions $|\tilde{\psi}_f\rangle$ through a linear operator $\mathcal{T}$:

$$|\psi_f\rangle = \mathcal{T}|\tilde{\psi}_f\rangle. \tag{8.3}$$

$\mathcal{T}$ differs from identity by a sum of local atom-centered contributions, that act only within spherical core regions centered on each atomic site $\mathbf{R}$, called augmentation regions or $\Omega_{\mathbf{R}}$:

$$\mathcal{T} = \mathbf{1} + \sum_{\mathbf{R},n}\Big[|\phi_{\mathbf{R},n}\rangle - |\tilde{\phi}_{\mathbf{R},n}\rangle\Big]\langle\tilde{p}_{\mathbf{R},n}|. \tag{8.4}$$

Here $|\phi_{\mathbf{R},n}\rangle$ and $|\tilde{\phi}_{\mathbf{R},n}\rangle$ are the all electron and pseudo partial waves, respectively, which coincide outside $\Omega_{\mathbf{R}}$. The vectors $\langle p_{\tilde{\mathbf{R}},n}|$, called projector functions [84], are equal to zero outside $\Omega_{\mathbf{R}}$ and satisfy the condition $\langle p_{\tilde{\mathbf{R}},n}|\phi_{\mathbf{R}',n'}\rangle = \delta_{\mathbf{R}\mathbf{R}'}\delta_{nn'}$. The index n refers to the angular momentum quantum numbers (l,m) and to an additional number, used if there is more than one projector per angular momentum channel. The $|\phi_{\mathbf{R},n}\rangle$ form a complete basis for any physical non-core all electron wave function within Ω_R[1]. Therefore the $\big|\tilde{\phi}_{\mathbf{R},n}\big\rangle$ are also a complete basis for any physical pseudo wave function $\big|\tilde{\psi}_f\big\rangle$ within $\Omega_{\mathbf{R}}$, i.e. for $\big\langle r\big|\chi_{\mathbf{R}}\big\rangle$ any function centered on an atomic site $\mathbf{R}$ and equal to zero outside $\Omega_{\mathbf{R}}$,

$$\sum_n \big\langle\tilde{\psi}\big|\tilde{p}_{\mathbf{R},n}\big\rangle\big\langle\tilde{\phi}_{\mathbf{R},n}\big|\chi_{\mathbf{R}}\big\rangle = \big\langle\tilde{\psi}\big|\chi_{\mathbf{R}}\big\rangle. \tag{8.5}$$

Substituting Eq. 8.4 in Eq. 8.3 and then Eq. 8.3 in Eq. 8.2, the transition amplitude $M_{i\to f}$ becomes

$$M_{i\to f} = \big\langle\tilde{\psi}_f\big|\mathcal{D}\big|\psi_i\big\rangle + \sum_{\mathbf{R},n}\big\langle\tilde{\psi}_f\big|\tilde{p}_{\mathbf{R},n}\big\rangle\big\langle\phi_{\mathbf{R},n}\big|\mathcal{D}\big|\psi_i\big\rangle - \sum_{\mathbf{R},n}\big\langle\tilde{\psi}_f\big|\tilde{p}_{\mathbf{R},n}\big\rangle\big\langle\tilde{\phi}_{\mathbf{R},n}\big|\mathcal{D}\big|\psi_i\big\rangle. \tag{8.6}$$

In Eq. 8.6, the initial wave function $\big\langle\mathbf{r}\big|\psi_i\big\rangle$ is localized on the site of the absorbing atom, $\mathbf{R}_0$, then only the $\mathbf{R}_0$ term has to be considered in each sum. Furthermore it should be noticed that $\big\langle\mathbf{r}\big|\mathcal{D}\big|\psi_i\big\rangle$ is zero outside the $\Omega_{\mathbf{R}_o}$ region. Therefore we can make use of Eq.8.5 for the third term of Eq.8.6, which thus vanishes with the first term. The transition amplitude $M_{i\to f}$ is then reduced to one term. Now, introducing

$$\big|\tilde{\varphi}_{\mathbf{R}_0}\big\rangle = \sum_{\mathbf{R},n}\big|\tilde{p}_{\mathbf{R}_o,n}\big\rangle\big\langle\phi_{\mathbf{R}_0,n}\big|\mathcal{D}\big|\psi_i\big\rangle, \tag{8.7}$$

we obtain the following simple expression for the X-ray absorption cross section

$$\sigma(\omega) = 4\pi^2\alpha\hbar\omega\sum_f |\big\langle\tilde{\psi}_f\big|\tilde{\varphi}_{\mathbf{R}_0}\big\rangle|^2\delta(E_f - E_i - \hbar\omega). \tag{8.8}$$

Thus Eq.8.8 expresses the XAS cross section in terms of single-particle states obtained from a pseudopotential calculation. Note that in Eq.8.7 there is an infinite number of projectors. Practically only a few projectors are needed to achieve convergence.

The calculation of XANES spectra from Eq.8.8 has the problem of determining many empty states $\big|\tilde{\psi}_f\big\rangle$. Indeed, the addition of unoccupied bands significantly increases computing time and then limits the size of the supercells. In the following section 8.2.4, we show how the recursion method permits the cross section Eq.8.8

---

[1] The solutions of the radial Schrödinger equation for the isolated atom is a natural choice for the all electron partial waves.

to be rewritten as a continued fraction, so that only occupied bands have to be calculated.

8.2.3. Ultrasoft pseudopotential extension

Here we report the formulation of XAS cross section 8.8 for the ultrasoft pseudopotentials reported in [91].

In an ultrasoft scheme the norm of the pseudopartial waves is different from the norm of the corresponding all-electron partial waves. For this reason it is customary to define [212] the integrated augmentation charges $q_{\mathbf{R},nm}$ as

$$q_{\mathbf{R},nm} = \langle \phi_{\mathbf{R},n} | \phi_{\mathbf{R},m} \rangle - \langle \tilde{\phi}_{\mathbf{R},n} | \tilde{\phi}_{\mathbf{R},m} \rangle .$$

The S operator defined in the ultrasoft scheme25 is then

$$S = \mathbf{1} + \sum_{\mathbf{R},m,n} | \tilde{p}_{\mathbf{R},n} \rangle q_{\mathbf{R},nm} \langle \tilde{p}_{\mathbf{R},m} | = \mathbf{1} + \sum_{\mathbf{R}} Q_{\mathbf{R}} .$$

The pseudo-Hamiltonian $\tilde{H}$ and the pseudoeigenfunctions $|\tilde{\psi}_f\rangle$ satisfy the following equation:25

$$\tilde{H} | \tilde{\psi}_f \rangle = E_f S | \tilde{\psi}_f \rangle . \tag{8.9}$$

Multiplication of Eq. 8.9 by $S^{-1/2}$ leads to

$$S^{-1/2} \tilde{H} S^{1/2} | \tilde{\psi}_f \rangle = E_f S^{1/2} | \tilde{\psi}_f \rangle .$$

The following identity hold (for proof see Appendix of [91]):

$$\pi \sum_f | \tilde{\psi}_f \rangle \delta \left(E_f - x \right) \langle \tilde{\psi}_f | = \lim_{\gamma \to 0} \mathcal{J} \left[\tilde{G}(x) \right] , \tag{8.10}$$

where x is a real number and

$$\tilde{G}(x) = S^{-1/2} \frac{1}{x - S^{-1/2} \tilde{H} S^{-1/2} - i\gamma} S^{-1/2}$$

Using Eqs. 8.10and 8.8, the XAS cross section can finally be written in a suitable form for a standard Lanczos procedure

$$\sigma(\omega) = 4\pi\alpha\hbar\omega \lim_{\gamma\to 0} \mathcal{J}\left[\langle\tilde{\phi}_{\mathbf{R}_o}|\tilde{G}(\hbar\omega + E_i)|\tilde{\phi}_{\mathbf{R}_o}\rangle\right]. \tag{8.11}$$

where E_i is the energy of the initial state that in a pseudopotential scheme is determined up to an overall constant. In the case of a unit cell having multiple absorbing sites, which are equivalent under the point-group symmetry of the crystal, E_i is the same for all the absorbing atoms and the choice of E_i simply corresponds to a rigid shift in the overall spectrum. On the contrary, in the case of nonequivalent absorbing sites in the unit cell, the value of E_i depends on the absorbing site due to the core-level shift. In this case the choice of E_i is not arbitrary and careful determination of the core-level shift is needed. For simplicity in this work we consider only examples in which there are only equivalent absorbing sites in the unit cell. The determination of the core-level shift in the case of multiple nonequivalent absorbing sites will be given elsewhere. Thus in what follows we choose the energy E_i to be the Fermi level, in the metallic case, the highest occupied state, in the insulating case.

8.2.4. Lanczos recursion method

Here a recursion method to solve the XAS cross section 8.11 for US pseudopotential scheme is presented, following the [91].

Equation 8.11 can be calculated using the Lanczos recursion method [86, 85]. The quantity $\langle\tilde{\phi}_{\mathbf{R}_o}|\tilde{G}(E)|\tilde{\phi}_{\mathbf{R}_o}\rangle$ is evaluated using the continued fraction,

$$\langle\tilde{\phi}_{\mathbf{R}_o}|\tilde{G}(E)|\tilde{\phi}_{\mathbf{R}_o}\rangle = \frac{\langle\tilde{\phi}_{\mathbf{R}_o}|S^{-1}|\tilde{\phi}_{\mathbf{R}_o}\rangle}{a_0 - E - i\gamma - \frac{b_1^2}{a_1 - E - i\gamma - \frac{b_2^2}{\ddots}}}$$

where the real numbers a_i and b_i are computed recursively by defining the vectors $|u_i\rangle$ such that

$$|u_0\rangle = \frac{S^{-1/2}|\tilde{\phi}_{\mathbf{R}_o}\rangle}{\sqrt{\langle\tilde{\phi}_{\mathbf{R}_o}|S^{-1}|\tilde{\phi}_{\mathbf{R}_o}\rangle}},$$

$$S^{-1/2}\tilde{H}S^{-1/2}\big|u_i\big\rangle = a_i\big|u_i\big\rangle + b_{i+1}\big|u_{i+1}\big\rangle + b_i\big|u_{i-1}\big\rangle.$$

The a_i and b_i coefficients are defined as

$$a_i = \big\langle u_i\big|S^{-1/2}\tilde{H}S^{-1/2}\big|u_i\big\rangle,$$

$$b_i = \big\langle u_i\big|S^{-1/2}\tilde{H}S^{-1/2}\big|u_{i-1}\big\rangle.$$

This is essentially a standard Lanczos process where the initial vector is $\big|u_i\big\rangle$ and the Hamiltonian $\tilde{H}$ is replaced by $S^{-1/2}\tilde{H}S^{-1/2}$. However this is not the more efficient way to carry out the Lanczos chain since two multiplications by $S^{-1/2}$ are involved and the S matrix is of the same order as the Hamiltonian, namely, the dimension is given by the number of plane waves in the calculation the kinetic-energy cutoff. Thus any application of $S^{-1/2}$ costs as much as the application of $\tilde{H}$.

A more efficient way to implement the Lanczos process is obtained by defining the auxiliary vectors $\big|t_i\big\rangle$, namely,

$$\big|t_i\big\rangle = S^{1/2}\big|u_i\big\rangle.$$

Using this definition, the Lanczos process can now be directly carried out on the $\big|t_i\big\rangle$vectors as

$$\big|t_0\big\rangle = \frac{\big|\tilde{\phi}_{\mathbf{R}_o}\big\rangle}{\sqrt{\big\langle\tilde{\phi}_{\mathbf{R}_o}\big|S^{-1}\big|\tilde{\phi}_{\mathbf{R}_o}\big\rangle}},$$

$$\tilde{H}S^{-1}\big|t_i\big\rangle = a_i\big|t_i\big\rangle + b_{i+1}\big|t_{i+1}\big\rangle + b_i\big|t_{i-1}\big\rangle,$$

where the new Lanczos vectors $\big|t_i\big\rangle$ are no longer orthogonal but $\big\langle t_i\big|S^{-1}\big|t_j\big\rangle = \delta_{i,j}$. If during the Lanczos chain the vectors$\big|\tilde{t}_i\big\rangle = S^{-1}\big|t_i\big\rangle$ are stored then the a_i and b_i coefficients can be defined as

$$a_i = \big\langle\tilde{t}_i\big|\tilde{H}\big|\tilde{t}_i\big\rangle,$$

$$b_i = \big\langle\tilde{t}_i\big|\tilde{H}\big|\tilde{t}_{i-1}\big\rangle,$$

Now, each iteration needs only one multiplication by S^{-1}, one multiplication by

$\tilde{H}$, and four Lanczos vectors stored in memory, namely, $|t_{i-1}\rangle$, $|\tilde{t}_{i-1}\rangle$, $|t_i\rangle$ and $|\tilde{t}_i\rangle$. To achieve an efficient implementation of the Lanczos process, particular care needs to be taken in inverting the S matrix to calculate S^{-1}. Direct inversion of the S matrix is unfeasible being the order of the matrix given by the number of plane waves. Using the definition of S in terms of the N_p ultrasoft projectors, the calculation of S^{-1} can be performed very efficiently by simple products and inversions of matrices of the order of $N_p \times N_p$, as it was demonstrated in Appendix of [91].

8.3. Implementation within *pseudo*-SIC

The method presented in Ref. [91], and reported in the previous section 8.2, has been implemented in the tool XSPECTRA that belongs to the Quantum ESPRESSO (QE) software package [92, 69].

We decided to import the main procedures of XSPECTRA tool within our code (PWSIC) because the latter is an old fork of PW code of QE, so they share most of the basic architecture. In addition, we think that the SI correction play its rule only in the calculation of quantity $\langle\tilde{\phi}_{\mathbf{R}_o}|\tilde{G}(E)|\tilde{\phi}_{\mathbf{R}_o}\rangle$, performed by Lanczos routine where the pseudo-SIC Hamiltonian could be easily substituted to the LDA or GGA Hamiltonian used in the standard routine.

Since we need of both core and valence all-electron wavefunctions of the absorbing atom to calculate 8.3, the pseudopotential used by XSPECTRA are accordingly modified to contain that additional information. Our program PWSIC uses a modified version of original program of Vanderbilt [93] to calculate the US pseudopotentials, thus we edited it to produce all-electron wavefunctions as output as well.

Here, I will picture schematically main steps of the routine that performs the calculation of XAS cross section:

- For each k point of a complete grid:
    - calculation of projector $|\tilde{p}_{\mathbf{R}_o,n}\rangle$ needed by function $|\tilde{\varphi}_{\mathbf{R}_0}\rangle$, defined in (8.7);

  - calculation of function $|\tilde{\varphi}_{\mathbf{R}_0}\rangle$, using $1s$ core and valence orbitals of absorbing atom from pseudopotential, and normalization of $|\tilde{\varphi}_{\mathbf{R}_0}\rangle$;
  - perform the Lanczos method on $|\tilde{\varphi}_{\mathbf{R}_0}\rangle$, applying the pseudo-SIC Hamiltonian,
  - and production of Lanczos a_i and b_i coefficients, stored in a separated file for an eventual post-processing.

- Perform the plot of XAS spectrum from Lanczos coefficients, cutting the occupied state as explained in [94].

8.3.1. First test applications

Below, I will account for some calculations of K-edges XAS spectra for different systems, performed using the PWSIC method supplemented by the XAS routine. I have chosen the same systems which were used in [91, 90] to have as better comparison as possible for my results, proving then the validity the method. I performed some trials on systems with and without core-hole in the absorbing atom, with different sizes, to see the effect of core-hole; with different number of projector per l-channel; employing simple LDA approximation or pSIC procedure. The pseudopotential used are ultrasoft, corrected by SI with the procedure explain in Section 5.1.3, and containing only one $1s$ electron (depending on case); plane waves were expanded with a energy cutoff of 30-40 Ry depending on the system; reciprocal-space integrations were performed using a full Monkhorst-Pack k-point grid. The calculations presented account for only the electric dipole component (some quadrupole calculations has been performed but will not be showed), which has always been performed after a self-consistent calculation of charge density of the probed supercell (including or not the $1s$ core-hole). The zero of energy is determined from the self-consistent calculation: in the metallic case the Fermi level has been chosen while in the insulating case the highest occupied state.

SiO_2 α-quartz

I will consider here SiO_2 α-quartz, which have a hexagonal unit cell with lattice parameters $a = 4.9141$ Å and $c = 5.4060$ Å [95]. The XANES Si K-edge spectrum was calculated for a 2x2x2 (72 atoms) supercell with core-hole in one of Si atom. A 2x2x2 grid of k-points was used for charge density calculation, while a 3x3x3 grid was used for Lanczos recursion. Notice that only the c-axis parallel dipole component is shown. The top figure 8.3 shows the comparison of experimental spectrum with one calculated using QE in LDA approximation (taken from [91]) that represents our reference. The bottom figure 8.3 is divided into two panel. In the top panel, I show the spectra obtained using QE and PWSIC codes in LDA approximation, but both employ a US pseudopotential for Si and O atoms, with one Si modified to have the $1s$ core-hole. As we can see, the agreement is very good, except for an underestimation of the main peak in the PWSIC spectrum. The QE one is almost identical to that shown in the top of the Figure 8.3 and thus to the experimental one. This confirm that the pseudopotential that I have generated is valid and is not the cause of the underestimation of the main peak. As we will see for the diamond spectra, this feature is common and needs a deeper understanding.

The bottom panel contains two main information. The first is the effect of core-hole presence which is necessary for a good description of the main peak, shown by the difference of the black curve respect with the other two's. The second is the effect of the additional empty $4s, 4p$ orbitals contained in the pseudopotential of the absorber atom. The standard configuration of Si atom is [Ne]$3s^2\,3p^2$, but since we are interested in $1s \to p$ empty states transitions, we need to add more p states, $4p$ in this case ($4s$ is not necessary, but it was included as well). Actually, as expressed in Eq. 8.7, we would need an infinite number of projectors, but usually a good result is obtained with only two projectors. Observing the blue and red curves, it is easy to see a better agreement of the spectra of the latter in all the energy range, especially around 10 eV and after 25 eV. Of course, I used a pseudopotential with 2 projectors for p states to calculate the spectrum of the supercell with core-hole show in the top panel.

Diamond

Figure (8.4) (top) shows the result of the K-edge XANES calculation for a 2x2x2 (16 atoms) supercell of diamond with and without the $1s$ core-hole in one Carbon atom chosen as absorber, from a QE calculation with LDA approximation. For similar reason explained for SiO_2 case, I generated a C pseudopotential containing two p projectors. The grid of k-point for the charge density and for Lanczos recursive method was a 4x4x4. In the bottom part of Figure (8.4), I show the spectra obtained from the routine implemented in PWSIC with and without core-hole, using both LDA (top panel) and pSIC (bottom panel) methods, to be compared with the top part of the Figure (8.4). Very good agreement is observed, giving another proof of the good working of the routine. To be noted that, the application of pSIC method continues to reproduce the correct general shape of spectra, but we cannot show here its effect, as it could be guessed since pSIC and LDA band structure for diamond are much similar. Again, an underestimation of the main peak is observed for both methods used, as in previous SiO_2 case.

Copper

Here, I consider the K-edge XANES spectra of metal Cu bulk, which crystallizes in the fcc structure with lattice parameter 3.601 Å [96], at room temperature. In this case, I used a 3x3x3 supercell with 27 Cu atoms, in which one of them is the absorber containing a $1s$ core-hole and two p projectors. Since it is a metal, LSDA is sufficient to access the correct band structure. I used a 2x2x2 k-points grid for charge density, and a 3x3x3 grid for XAS calculation. The agreement between experimental (bottom, dotted line) and calculated (top) spectrum is well shown in the Figure 8.5. All A, B, C, D and E peaks are well localized. We remind that the calculated spectrum shown in the bottom of the Figure 8.5 come from a calculation where a more dense k-point grid was used [91].

La_2CuO_4

La_2CuO_4 is the parent compound of high-Tc superconductors. It is an antiferromagnetic correlated insulator considered as a challenge for density-functional theory. Experimentally, La_2CuO_4 is an insulator with a gap around 2 eV [97] and exhibits an antiferromagnetic order with a magnetic momentum on copper atoms around 0.5 μ_b. At low temperatures La_2CuO_4 present a weak orthorhombic distortion of the tetragonal structure. In our pSIC calculation we neglect the orthorhombic distortion and consider the tetragonal structure having $a = 5.357$ Å and $c = 13.143$ Å [98]. Our electronic structure calculation of the tetragonal cell with 28 atoms, without a core-hole, and a 4x4x4 k-points grid gives a gap around 1 eV and a magnetization of about 0.66 μ_B.

For the Cu K-edge XAS dipolar cross section calculation, I used the same pseudopotential used for pure metal copper, with a core-hole inside, and a grid of 4x4x4 k-points for Lanczos recursion. The result for c-axis parallel component of spectrum is pictured in Figure 8.6 (bottom) together with the experimental and GGA+U spectra (top) taken from [91]. The general agreement in very good, since all the three features are reproduced at the right energy.

NiO

Nickel oxide is a prototype of correlated material or Mott insulator, in which the elementary excitation is a charge transfer from O valence states to mainly Ni conduction states located above the valence top. The pSIC approach allows to access to a correct gap value and a magnetic moment, as reported in [56]. Whereas the XAS calculation with the implemented procedure is still an open problem, as I will explain below.

The NiO experimental crystal structure was probed. The paramagnetic-cell group space is $Fm\bar{3}m$ where Ni occupies the 4a position and O the 4b. The cubic lattice parameter is $a = 4.1788$ Å [99] and our antiferromagnetic fcc cell contains 16 atoms. I used a 4x4x4 k-points grid for both charge density and Lanczos calculation. Since the addition of the core-hole avoid the convergence of charge density calculation, we had access only to a spectrum that is not influenced by core-hole attraction. The problem need to be investigated deeper, but likely it can be solved considering a large supercell in which the core-hole replicas are more distant and their interaction could be lower. Nonetheless, Figure 8.7 shows a quite good agreement between experimental and pSIC spectra. In particular, peaks E, D and C are very well reproduced, whereas peak B is downshifted by around 2 eV. This peak is due to d states above the valence top. The problem comes from the fact that I obtain a reduced band gap, around 3 eV, due to a low accuracy of my charge density calculation. The interpretation of peak A is quite controversial (see

[90]) and we will not further discuss it here, but we say that since it much depend on the core-hole presence, we can not access to it yet.

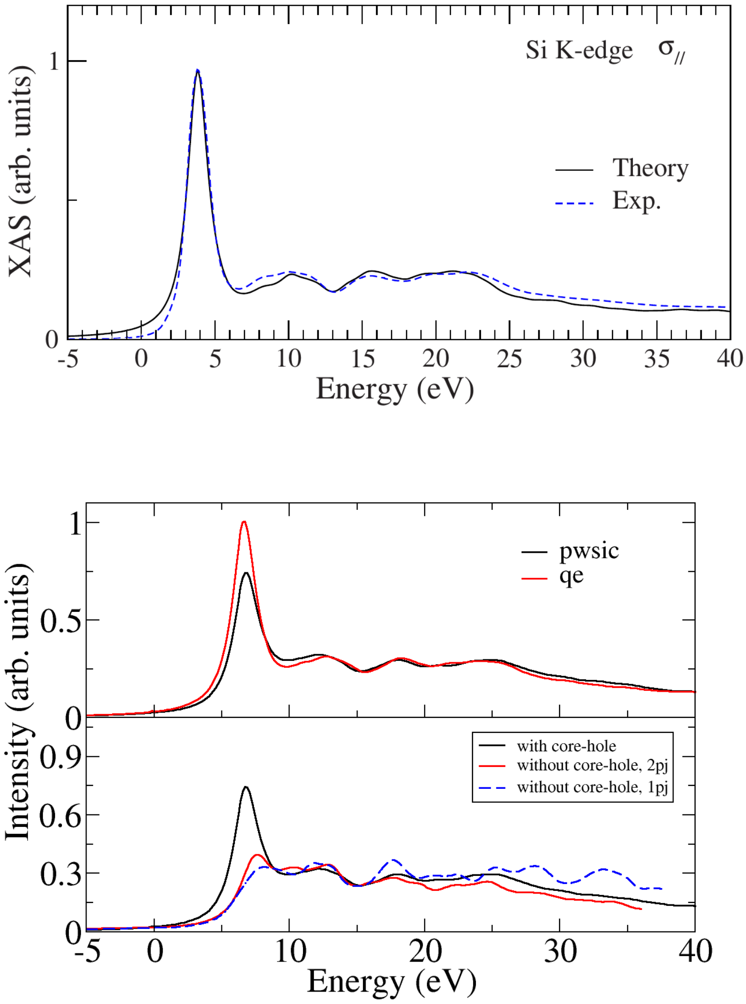

Figure 8.3.: (top) Experimental and calculated, using QE/XSPECTRA, Si K-edge XAS spectra of SiO_2 as they appear in Ref. [91]. (bottom) Comparison between QE/XSPECTRA and PWSIC calculated spectra (top panel) and the effect of core-hole and of the projectors in the spetrum calculation (bottom panel). In both figures, only the parallel to c-axis component of XAS cross section is shown.

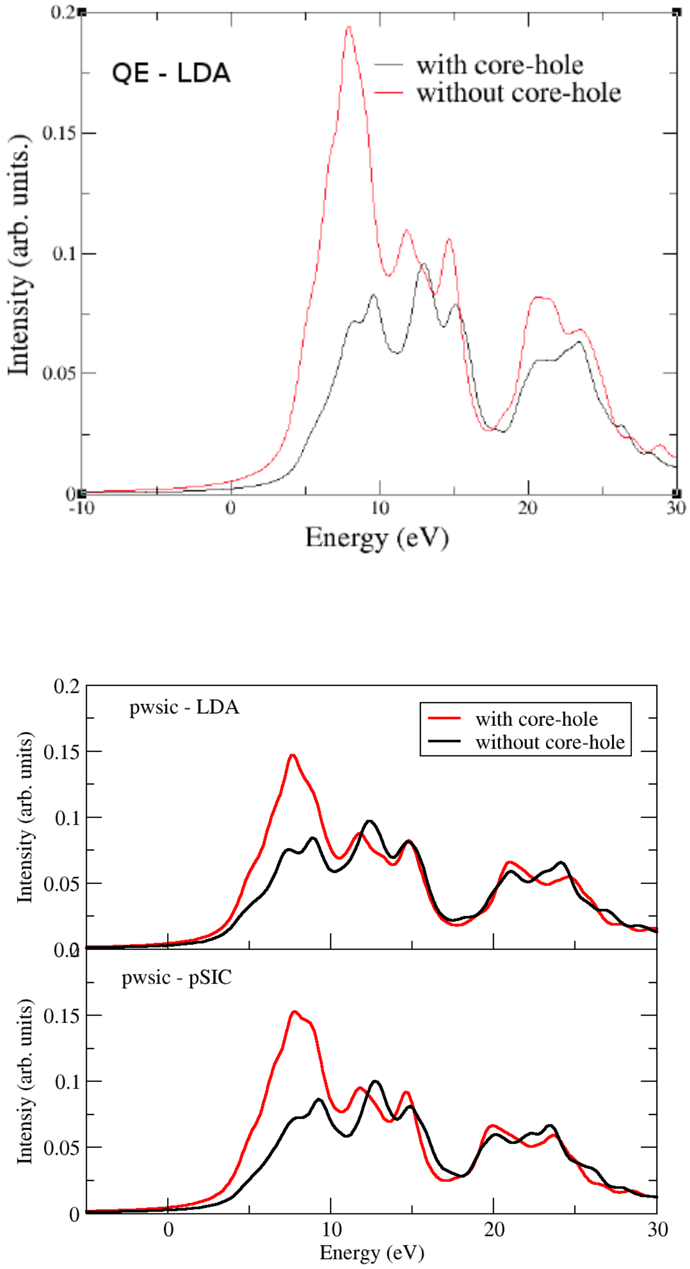

Figure 8.4.: (top) C K-edge XAS spectrum in Diamond calculated in LDA approximation using QE/XSPECTRA code. (bottom) Same spectra calculated with PWSIC code using LDA (top panel) and pSIC (bottom panel) approximations, including or not the presence of the core-hole.

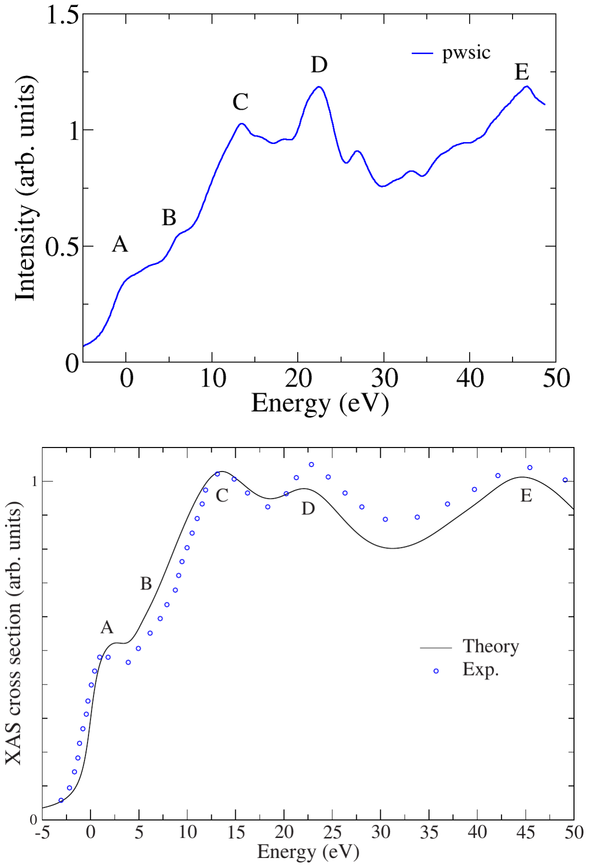

Figure 8.5.: (top) Calculated Cu K-edge XAS spectrum in bulk copper using PWSIC code. (bottom) Experimental and theoretical spectra as shown in Ref. [91] where LDA approximation and QE/XSPECTRA code were used.

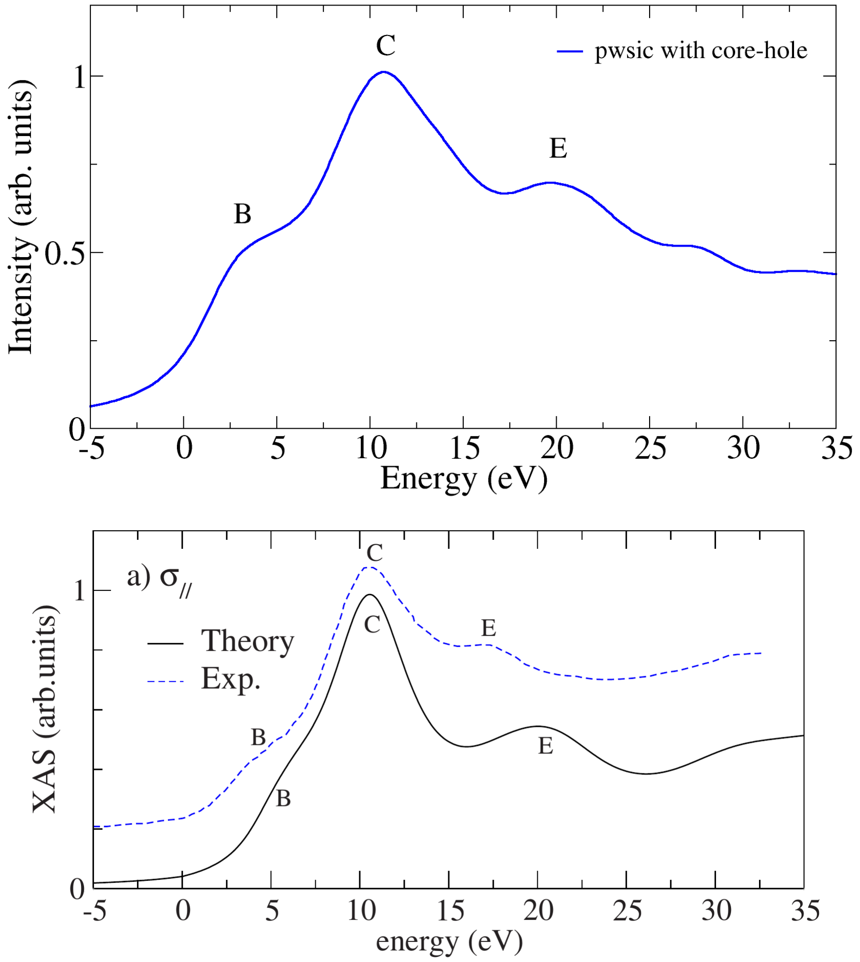

Figure 8.6.: (top) Cu K-edge XAS spectrum of La_2CuO_4 calculated with PWSIC in the presence of core-hole. (bottom) Experimental and theoretical spectra as shown in Ref. [91] where GGA+U approximation and QE/XSPECTRA code were used. In both figures, only the parallel to c-axis component of XAS cross section is shown.

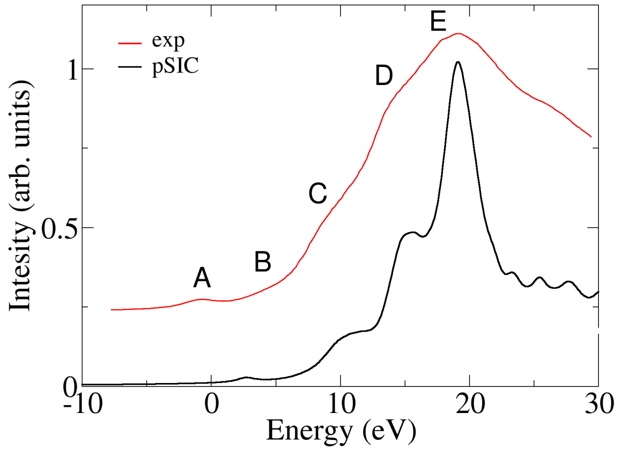

Figure 8.7.: Ni K-edge XAS spectrum of the correlated insulator NiO in its antiferromagnetic phase calculated in PWSIC code, compared with experimental spectrum from Ref. [100].

Conclusions

In this concluding section, I will summarize all main outcomes of various works developed during my PhD and presented in this thesis.

In chapter 2, a study of the $SrRuO_3/PbTiO_3/SrRuO_3$ multiferroic junction has been reported. A large ferro-electric polarization and two different potential profiles, due to asymmetric interfaces, have been assessed. Morover, both giant tunneling electro-resistance and the interface magneto-electric effect has been shown. The latter effect modulates, upon the inversion of polarization, the in-plane spin conductance and it could be exploitable in pratical applications. As it has been done for the well known $SrRuO_3/BaTiO_3/SrRuO_3$ MFTJ, to complete the study of our MFTJ, we plan to study the tunneling magneto-resistance, which we may expect to find as large as TER. Another interesting research line is that of magnetic doping of the FE layer or the interfaces. The latter doping, in particular, was started with the substitution of an interface Ti atom with a Vanadium to observe the influence on the TER and ME effects.

Around the same area is located our work, presented in chapter 3, on the possibility of doping the $PbTiO_3$ with Vanadium with the aim of adding magnetic properties to a ferroelectric material. In fact, we have found that V:PTO is a ferroelectric insulator with a stable ferromagnetic phase, thus a proper multiferroic compound.

In chapter 4, I have reported an on-going investigation about what we consider the first ferroelectric metal: the layered perovskite $Bi_5Ti_5O_{17}$ (Bi-5517). We have demonstrated the coexistence of metallicity, mainly localized in low-dimensional electron gas, and native bulk ferroelectric polarization. The crucial point of assessing a residual field in a finite slab of Bi-5517 is still under development. The slab separated by vacuum presented here was the first attempt to accomplish this target. Thought we have shown that we find the existance of survival polarization, we think that this effect could be a product of dangling bonds of one termination, that capture part of the free conduction electrons. To avoid this problem we have studied a Bi-5517 slab grown on top of the $Bi_2Zr_2O_{10}$ perovskite that is an insulator with a very similar structure of Bi-5517. Since in this system the polarization disappears because of conduction electrons, we have tried to dope the Bi-5517 with a single Ca atom, in place of a Bi atom, to reduce the amount of free charge. This system has shown a residual polarization, even though remaining metallic. We are convinced that this first investigation will open the way to significative both conceptual and applicative perspectives.

In chapter 6, we have presented an investigation of the electronic structure of $CaCu_3Ti_4O_{12}$ performed comparing different density functional based methods, proposing a new interpretation of the four optical transitions observed experimentally. This work represents another good proof to validate the reliability of pSIC approach, that along with the account for the effect of spin disorder, though approximate, is able to reproduce the experimental spectrum and explain the correct origin of its features.

In chapter 7, we have reported three different works about the promising TCO material Ga_2O_3. The first study (Section 7.1) has been developed in collaboration with the research group of Prof. Fornari at the University of Parma, with the aim of characterizing the gap of Ga_2O_3 in its β phase. The crucial aspect of this work has been the use of the routine that calculate the dielectric function, implemented in our code PWSIC. Thank to the accuracy in band structure calculation of pSIC method, the calculated spectra has turned out to be in very good agreement with the experimental ones, confirming the anisotropy of optical absorptions.

Motivated by the previous study, we develop a further investigation on the doping of Ga_2O_3 with In, reported in sections 7.2 and 7.3. We perform ab-initio DFT-GGA calculations of the electronic and local structural properties depending on In concentration. Next, we have found the maximum In solubility in $\beta-Ga_2O_3$ around 10%, that is the first theoretical assessment and close to recent experimental value. In addition, we study the band alignment of interface between β-Ga_2O_3 and $(Ga_{1-x}In_x)_2O_3$ at 12%, in different growth conditions. This should be the first theoretical investigation in this type of interfaces that are considered promising in the searching of new TCO materials for electronic applications. Indeed, we are currently perfoming an *opposite* study focused on the doping of In_2O_3 with Ga, obtaining interesting results.

Finally, in chapter 8, I have showed the first test applications of the routine for XAS cross section calculation that exploits the pSIC approach. Observing the calculated spectra compared with both experimental and calculated by QE code, we have the evidence that the porting of routine is properly working and the correction to the band structure provided by pSIC method allows to reproduce the main aspects of experimental spectrum. Although the routine porting is not completed and the role of core-hole deserves further investigations, we think that the capability to reproduce XAS spectra exploiting the pSIC method may surely open the way to a deeper knowleadge of experimental spectra coming from a wide range of materials, expecially strong correleted ones, difficult to be accessed with standard DFT functional, in a more accurated form respect to LDA+U method, and limiting the computational cost respect with GW method. Materials such as transition metal oxides, CuO for example, and doped cuprates, known for their superconductive properties, are all well described by pSIC method, hence they represent first candidates to be probed by XAS routine. Secondly, we could devote our attention to give a theoretical support to XAS spectra of some complex molecules, frequently studied by chemists by using experimental XAS. Problably too ambitious, the investigation, using calculated XAS, of two-dimensional electron gas at the interface between oxides, whereas accessed by experimental XAS.

Acknowledgments

I would like to express my infinite gratitude to Prof. Vincenzo Fiorentini, who gave me the great opportunity to start my PhD in his research group. He has given to me a substantial support providing many of the ideas developed during last three years and reviewed in this thesis. Last but not the least, he has also provided a research grant (IOM-CNR, UOS Cagliari) for my PhD school. I just hope I have repayed with my humble work, at least partially.

My gratitude also goes to Alessio Filippetti and Pietro Delugas for usefull discussions about the pSIC method and the code which implement it.

I acknowledge my gratitude to Jorge Iniguez for reviewing of this thesis and usefull suggestions.

I would like to thank my "always smiling" colleague Maria Barbara Maccioni, who developed most of the work about In-doping of Ga_2O_3, which I collaborated on. I also thank her to help me with administrative issues.

I acknowledge my gratitude also to the coordinator Prof. Paolo Ruggerone for his careful management of the PhD school.

Finally, thank to all my colleagues for sharing a lot of fun during last three years.

References

[1] J. Valasek, Physical Review 15, 537 (1920), and J. Valasek, Physical Review 17 (4), 475 (1921).

[2] A. F. Devonshire, Phil. Mag. 40, 1040 (1949); ibid 42, 1065 (1951); Adv. Phys. 3, 85 (1954).

[3] E. Fatuzzo and W.M. Mertz, Ferroelectricity (North-Holland, Amsterdam, 1967).

[4] M.E. Lines and A.M. Glass, Principles and Applications of Ferroelectrics and Related Materials, (Oxford University Press, Oxford, 1977).

[5] P. Chandra, P.B. Littlewood, *A Landau Primer for Ferroelectrics*, Physics of Ferroelectrics pp 69-116, Volume 105, Springer Berlin Heidelberg (2007).

[6] K.F. Wang, J.-M. Liu and Z.F. Ren, Advances in Physics Vol. 58, No. 4, 321–448 (2009).

[7] D.I. Khomskii, J. Magn. Magn. Mater., 306 p. 1 (2006).

[8] R.E. Cohen, Nature 358, p. 136. (1992).

[9] G. Trinquier and J.R. Hoffmann, J. Phys. Chem. 88, p. 6696 (1984).

[10] G.W. Waston, S.C. Parker, and G. Kresse, Phys. Rev. **B** 59 8481 (1999). R. Seshadri and N.A. Hill, Chem. Mater. 13, p. 2892 (2001).

[11] F. Ricci, A. Filippetti, and V. Fiorentini, Phys. Rev. B **88**, 235416 (2013).

[12] F. Ricci and V. Fiorentini, J. Phys.: Conf. Ser. 470, 012013 (2013).

[13] K.F. Wang, J.-M. Liu, and Z.F. Ren, Advances in Physics Vol. {**58**}, No. 4, 321-448 (2009).

[14] R. Resta, Rev. Mod. Phys. 66 (1994) 899–915.

[15] Resta, R., Ferroelectrics 136, 51 R. 13 (1992).

[16] R. Resta, Europhysics News 28 (1997).

[17] King-Smith R.D., and D. Vanderbilt, Phys. Rev. B 47 1651 (1993).

[18] Kleemann, W., F. J. Schafer, and M. D. Fontana, Phys. Rev. B **30** 1148 (1984).

[19] Berry, M.V., 1984, Proc. R. Soc. London, Ser. A 392, 45.

[20] Berry, M. V., 1989, in Geometric Phases in Physics, edited by A. Shapere and F. Wilczek (World Scientific, Singapore), p. 7.

[21] Dal Corso, A., R. Resta, and S. Baroni, 1993b, Phys. Rev. B 47, 16252.

[22] Resta, R., M. Posternak, and A. Baldereschi, 1993a, Phys. Rev. Lett. 70, 1010. Resta, R., M. Posternak, and A. Baldereschi, 1993b, Mat. Res. Soc. Symp. Proc. 291, 647.

[23] $BaTiO_3$: R. Wahl, D. Vogtenhuber, and G. Kresse, Phys. Rev. B **78**, 104116 (2008). $BiFeO_3$: J. B. Neaton, C. Ederer, U. V. Waghmare, N. A. Spaldin, K. M. Rabe, Phys. Rev. B **71** 014113 (2005). $PbTiO_3$: K. N. Ishida, S. Kasai, K. T. Anaka, Y. S. Akabe, F. Ishii and T. Oguchi, Jpn. J. Appl. Phys. Vol. 40, pp. 5806–5808 (2001).

[24] Stengel, M. & Spaldin, Nature 443, 679–682 (2006).

[25] J.M. Rondinelli, M. Stengel,N. A. Spaldin, Nature Nanotechnology 3, 46 - 50 (2008).

[26] Zhang, S., Phys. Rev. Lett. 83, 640–643 (1999).

[27] Duan, C.-G., Velev, J. P., Sabirianov, R. F., Zhu, Z., Chu, J., Jaswal, S. S. & Tsymbal, E. Y., Phys. Rev. Lett. 101, 137201 (2008).

[28] Niranjan, M. K., Velev, J. P., Duan, C.-G., Jaswal, S. S. & Tsymbal, E. Y., Phys. Rev. B 78, 104405 (2008).

[29] Yamauchi, K., Sanyal, B. & Picozzi, S., Appl. Phys. Lett. 91, 062506 (2007)

[30] J. P. Velev, S. S. Jaswal, and E. Y. Tsymbal, Phil. Trans. R. Soc. A {**369**}, 3069-3097 (2011).

[31] M. Ye. Zhuravlev, R. F. Sabirianov, S. S. Jaswal, and E. Y. Tsymbal, Phys. Rev. Lett. **94**, 246802 (2005).

[32] E.Y. Tsymbal, A. Gruverman, V. Garcia, M. Bibes, and A. Barthélémy, *Ferroelectric and multiferroic tunnel junctions*, MRS Bulletin, Volume 37, February 2012.

[33] B.D. Josephson, Rev. Mod. Phys. 46, 251 (1974).

[34] G. Binnig, H. Rohrer, Rev. Mod. Phys. 59, 615 (1987).

[35] R.H. Fowler, L. Nordheim, Proc. R. Soc. London 119, 173 (1928).

[36] C. Chappert, A. Fert, F.N. Van Dau, Nat. Mater. 6, 813 (2007).

[37] E.Y. Tsymbal, I. Žutić, Eds. Handbook of Spin Transport and Magnetism, (Taylor & Francis, NY, 2011).

[38] P.M. Tedrow, R. Meservey, Phys. Rev. Lett. 26, 192 (1971).

[39] M. Jullière, Phys. Lett. A 54, 225 (1975).

[40] J.S. Moodera, L.R. Kinder, T.M. Wong, R. Meservey, Phys. Rev. Lett. 74, 3273 (1995).

[41] T. Miyazaki, N.J. Tezuka, J. Magn. Mag. Mater. 139, L231 (1995).

[42] E.Y. Tsymbal, O.N. Mryasov, P.R. LeClair, J. Phys.: Condens. Matter 15, R109 (2003); E.Y. Tsymbal, K.D. Belashchenko, J. Velev, S.S. Jaswal, M. van Schilfgaarde, I.I. Oleynik, D.A. Stewart, Prog. Mater. Science. 52, 401 (2007). Schilfgaarde, I.I. Oleynik, D.A. Stewart, Prog. Mater. Science. 52, 401 (2007).

[43] D. Wang, C. Nordman, J. Daughton, Z. Qian, J. Fink, IEEE Trans. Magn. 40, 2269 (2004).

[44] D.J. Monsma, S.S.S. Parkin, Appl. Phys. Lett. 77, 720 (2000).

[45] E.Y. Tsymbal, H. Kohlstedt, Science 313, 181 (2006).

[46] M.Y. Zhuravlev, S.S. Jaswal, E.Y. Tsymbal, R.F. Sabirianov, Appl. Phys. Lett. 87, 222114 (2005).

[47] M.Y. Zhuravlev, S. Maekawa, E.Y. Tsymbal, Phys. Rev. B 81, 104419 (2010).

[48] J.P. Velev, C.-G. Duan, J.D. Burton, A. Smogunov, M.K. Niranjan, E. Tosatti, S.S. Jaswal, E.Y. Tsymbal, Nano Lett. 9, 427 (2009).

[49] M.K. Niranjan, J.D. Burton, J.P. Velev, S.S. Jaswal, E.Y. Tsymbal, Appl. Phys. Lett. 95, 052501 (2009).

[50] V. Garcia, M. Bibes, L. Bocher, S. Valencia, F. Kronast, S. Enouz-Vedrenne, A. Gloter, D. Imhoff, C. Deranlot, N.D. Mathur, S. Fusil, K. Bouzehouane, A. Barthélémy, Science 327, 1106 (2010).

[51] P. E. Blöchl, Phys. Rev. B {\bf 50}, 17953 (1994); G. Kresse and D. Joubert, Phys. Rev. B {**59**}, 1758 (1999).

[52] G. Kresse and J. Furthmüller, Phys. Rev. B {**54**}, 11169 (1996).

[53] See e.g. R. W. Godby and P. Garcia-Gonzalez, in {*A Primer in Density Functional Theory*}, Springer Lecture Notes in Physics, C. Fiolhais, F. Nogueira, M. Marques eds. (Springer, Berlin 2003), Ch. 5, p.185.

[54] H. K. Chandra, K. Gupta, A. K. Nandy, and P. Mahadevan, Phys. Rev. B {**87**}, 214110 (2013).

[55] M. B. Maccioni, F. Ricci, V. Fiorentini Appl. Phys. Express 8, 021102 (2015).

[56] A. Filippetti and V. Fiorentini, Eur. Phys. J. B **71**, 139 (2009).

[57] A. Filippetti and N. A. Spaldin, Phys. Rev. B {\bf 67}, 125109 (2003).

[58] J.F. Janak, Phys. Rev. B 18, 7165 (1978).

[59] J.P. Perdew, A. Zunger, Phys. Rev. B 23, 5048 (1981).

[60] D. Vogel, P. Kr üger, J. Pollmann, Phys. Rev. B 54, 5495 (1996).

[61] L. Kleinman and D. M. Bylander, Phys. Rev. Lett. 48 (20), 1425 (1982).

[62] D. Vanderbilt, Phys. Rev. B 41, R7892 (1990).

[63] G. Zwicker, K. Jacobi, Solid State Comm. 54, 701 (1985).

[64] G. Grosso and G. Pastori Parravicini, Solid State Physics (Academic Press, 2000).

[65] N. W. Ashcroft and N. D. Mermin, Solid State Physics (Saunders College Publishing, New York, 1976), p. 340.

[66] C. B. Duke, Tunneling in Solids (Academic, New York, 1969).

[67] Editors: Ginley, David, Hosono, Hideo, Paine, David C., *Handbook of Transparent Conductors, Springer (2011)*

[68] H. A. Kramers, Nature 117, 775 (1926). R. de L. Kronig, J. Opt. Soc. Am. 15, 547 (1926).

[69] P. Giannozzi et al., http://www.quantum-espresso.org

[70] H. Kageshima and K. Shiraishi, Phys. Rev. B **56**, 23 (1997).

[71] B. Adolph, J. Furthmüller, and F. Bechstedt, Phys. Rev. B **63**, 125108 (2001).

[72] A. Mottana and A. Marcelli, not published yet, http://arxiv.org/abs/1312.5295 (2013).

[73] Ch. Brouder, J. Phys.:Condens. Matter 2, 701 (1990).

[74] J. A. Soininen and E. L. Shirley, Phys. Rev. B **64**, 165112:1 (2001).

[75] R. D. Cowan, The Theory of Atomic Structure and Spectra (University of California Press, Berkeley, 1981).

[76] S. Köstlmeier and C. Elsässer, Phys. Rev. B **60**, 14 025 (1999). M. A. Gülgün, W. Y. Ching, Y.-N. Xu, and M. Rühle, Philos. Mag. B 79, 921 (1999).

[77] W.H.E. Schwarz, R.J. Buenker: Chem. Phys. **13**, 153 (1976).

[78] J. C. Slater, Adv. Quantum Chem. 6, 1 (1972). J. C. Slater and K. H. Johnsson, Phys. Rev. B **5**, 844 (1972).

[79] K. Ogasawara, I. Tanaka, and H. Adachi, Adv. Quantum Chem. 29, 41 (1997); I. Tanaka and H. Adachi, Phys. Rev. B **54**, 4604 (1996)

[80] M. Taillefumier, D. Cabaret, A.-M. Flank, and F. Mauri, Phys. Rev. B **66**, 195107 (2002).

[81] B. Hetényi, F. De Angelis, P. Giannozzi, and R. Car, J. Chem. Phys. 120, 8632 (2004).

[82] C. J. Pickard and M. C. Payne, in Electron Microscopy and Analysis (1997), edited by J. M. Rodenburg, Vol. 153, pp. 179- 182, Proceedings of the Institute of Physics Electron Microscopy and Analysis Group Conference, University of Cambridge IOP, Bristol, (1997). P. Rez, J. R. Alvarez, and C. J. Pickard, Ultramicroscopy 78, 175 (1999). S. P. Gao, C. J. Pickard, M. C. Payne, J. Zhu, and J. Yuan, Phys. Rev. B 77, 115122 (2008).

[83] S.-D. Mo and W. Y. Ching, Phys. Rev. B 62, 7901 (2000).

[84] P. E. Blöchl, Phys. Rev. B 50, 17953 (1994).

[85] R. Haydock, V. Heine, and M. J. Kelly, J. Phys. C 5, 2845 (1972). R. Haydock, V. Heine, and M. J. Kelly, J. Phys. C 8, 2591 (1975).

[86] C. Lanczos, J. Res. Natl. Bur. Stand. 49, 33 (1952). C. Lanczos, J. Res. Natl. Bur. Stand. 45, 255 (1950).

[87] D. Prendergast and G. Galli, PRL **96**, 215502 (2006).

[88] I. Tanaka, H. Araki, M. Yoshiya, T. Mizoguchi, K. Ogasawara, and H. Adachi, Phys. Rev. B **60**, 4944 (1999). T. Mizoguchi, I. Tanaka, F. Oba, K. Ogasawara, and H. Adachi, Phys. Rev. B **61**, 2180 (2000). K. Ogasawara, I. Tanaka, and H. Adachi, Adv. Quantum Chem. 29, 41 (1997). I. Tanaka and H. Adachi, Phys. Rev. B **54**, 4604 (1996).

[89] V. I. Anisimov, J. Zaanen, and O. K. Andersen, Phys. Rev. B **44**, 943 (1991); V. I. Anisimov, F. Aryasetiawan, and A. I. Liecht-enstein, J. Phys.: Condens. Matter 9, 767 (1997). M. Cococcioni and S. de Gironcoli, Phys. Rev. B 71, 035105 (2005).

[90] C. Gougoussis, M. Calandra, A. Seitsonen, Ch. Brouder, A. Shukla, and F. Mauri, Phys. Rev. B 79, 045118 (2009).

[91] C. Gougoussis, M. Calandra, A. Seitsonen, and F. Mauri, Phys. Rev. B 80, 075102 (2009).

[92] The XSPECTRA package by C. Gougoussis, M. Calandra, A. Seit- sonen, and F. Mauri is available under the GNU license in the current CVS version of the Quantum ESPRESSO code.

[93] Official Vanderbilt Ultra-Soft Pseudopotential Site, http://www.physics.rutgers.edu/~dhv/uspp/ .

[94] Ch. Brouder, M. Alouani, and K. H. Bennemann, Phys. Rev. B **54**, 7334 (1996).

[95] G. A. Lager, J. D. Jorgensen, and F. J. Rotella, J. Appl. Phys. 53, 6751 (1982).

[96] H. M. Otte, J. Appl. Phys. 32, 1536 (1961).

[97] J. M. Ginder, M. G. Roe, Y. Song, R. P. McCall, J. R. Gaines, E. Ehrenfreund, and A. J. Epstein, Phys. Rev. B 37, 7506 (1988).

[98] M. Reehuis, C. Ulrich, K. Prokes, A. Gozar, and G. Blumberg, Seiki Komiya, Yoichi Ando, P. Pattison, and B. Keimer, Phys. Rev. B 73, 144513 (2006).

[99] S. P. Srivastava, R. C. Srivastava, I. D. Singh, S. D. Pandey, and P. L. Gupta, J. Phys, Soc. Jpn. 43, 885 (1977).

[100] R. V. Vedrinskii, V. L. Kraizman, A. A. Novakovich, Sh. M. Elyafi, S. Bocharov, Th. Kirchner, and G. Dräger, Phys. Status Solidi B 226, 203 (2001).

[101] E. Y. Tsymbal, A. Gruverman, V. Garcia, M. Bibes and A. Barthélémy, MRS Bulletin **37**, 138 (2012).

[102] K. F. Wang, J.-M. Liu, and Z. F. Ren, Adv. Phys. **58**, 321 2009.

[103] J. Junquera and P. Ghosez, Nature **422**, 506 (2003).

[104] V. Garcia, S. Fusil, K. Bouzehouane, S. Enouz-Vedrenne, N.D. Mathur, A. Barthélémy, M. Bibes, Nature **460**, 81 (2009).

[105] A. Gruverman, D. Wu, H. Lu, Y. Wang, H.W. Jang, C.M. Folkman, M.Y. Zhuravlev, D. Felker, M. Rzchowski, C.-B. Eom, E.Y. Tsymbal, Nano Lett. 9, 3539 (2009).

[106] J. P. Velev *et al.*, Nano Lett. **9**, 427 (2009).

[107] M. Y. Zhuravlev, S. Maekawa and E. Y. Tsymbal, Phys. Rev. B **81**, 104419 (2010).

[108] C.-G. Duan, S. S. Jaswal, and E. Y. Tsymbal, Phys. Rev. Lett. **97**, 047201 (2006).

[109] N.M. Caffrey, T. Archer, I. Rungger and S. Sanvito, Phys. Rev. Lett. **109**, 226803 (2012).

[110] M. K. Niranjan, J. D. Burton, J. P. Velev, C.-G. Duan, S. S. Jaswal, and E. Y. Tsymbal, Appl. Phys. Lett. **95**, 052501 (2009).

[111] G. Kresse and J. Furthmüller, Phys. Rev. B **54**, 11169 (1996); G. Kresse and D. Joubert, *ibid.* **59**, 1758 (1999).

[112] M. Peressi, N. Binggeli, and A. Baldereschi, J. Phys. D: Appl. Phys. **31**, 1273 (1998).

[113] F. Bernardini and V. Fiorentini, Phys. Rev. B **57**, R9427 (1998).

[114] W. Guo, D. Jin, W. Wei, and H. J. Marisa, J. Appl. Phys. **102**, 084104 (2008); Ø. Dahl, J. K. Grepstad, and T. Tybella, *ibid.*, **103**, 114112 (2008).

[115] A. Chanthbouala, A. Crassous, V. Garcia, K. Bouzehouane, S. Fusil, X. Moya, J. Allibe, B. Dlubak, J. Grollier, S. Xavier, C. Deranlot, A. Moshar, R. Proksch, N. D. Mathur, M. Bibes, and A Barthélémy, Nature Nanotech. **7**, 101 (2011).

[116] J. P. Velev, C.-G. Duan, J. D. Burton, Alexander Smogunov, M. K. Niranjan E.Tosatti, S. S. Jaswal, and E. Y. Tsymbal, Nano Lett. **9**, 427 (2009).

[117] K. D. Belashchenko *et al.*, Phys. Rev. B **69**, 174408 (2004).

[118] G. K. H. Madsen and D. J. Singh, Comput. Phys. Commun. **175**, 67 (2006).

[119] J. M. Rondinelli, M. Stengel and N. Spaldin, Nat. Nanotech. **3**, 46 (2008).

[120] Y. Umeno, J. M. Albina, B. Meyer, and C. Elsässer, Phys. Rev. B **80**, 205122 (2009)

[121] P. Ghosez and J. Junquera, Chap. 134 of *Handbook of theoretical and computational nanotechnology*, M. Rieth and W. Schommers eds. (American Scientific Publishers, Valencia, USA, 2006).

[122] S. J. Callori, J. Gabel, D. Su, J. Sinsheimer, M. V. Fernandez-Serra, and M. Dawber Phys. Rev. Lett. **109**, 067601 (2012).

[123] C. C. Homes, T. Vogt, S. M. Shapiro, S. Wakimoto, and A. P. Ramirez, Science **293**, 673 (2001). For a recent review see P. Lunkenheimer, S. Krohns, S. Riegg, S. G. Ebbinghaus, A. Reller, and A. Loidl, Eur. Phys. J. Special Topics **180**, 61 (2010).

[124] L. He, J. B. Neaton, M. H. Cohen, D. Vanderbilt, and C. C. Homes, Phys. Rev. B **65**, 214112 (2002).

[125] T. Arima, Y. Tokura, and J. B. Torrance, Phys. Rev. B **48** 17006 (1993).

[126] L. Hedin and S. Lundqvist, Solid. St. Phys. **23**, 1 (1970).

[127] P. Alippi, V. Fiorentini, and A. Filippetti, ECS Trans. **3**, 291 (2006).

[128] A. Filippetti, G. M. Lopez, M. Mantega, and V. Fiorentini, Phys. Rev. B **78**, 233103 (2008); G. M. Lopez, A. Filippetti, M. Mantega, and V. Fiorentini, Phys. Rev. B **82**, 195122 (2010).

[129] Ch. Kant, T. Rudolf, F. Mayr, S. Krohns, P. Lunkenheimer, S. G. Ebbinghaus, and A. Loidl, Phys. Rev. B **77**, 045131 (2008).

[130] P. Lunkenheimer, private communication.

[131] J. H. Clark, M. S. Dyer, R. G. Palgrave, C. P. Ireland, J. R. Darwent, J. B. Claridge, and M. J. Rosseinsky, J. Am. Chem. Soc. **133**, 1016 (2011).

[132] A. Filippetti, C. D. Pemmaraju, S. Sanvito, P. Delugas, D. Puggioni, and V. Fiorentini, Phys. Rev. B **84**, 195127 (2011).

[133] The 'Mott' label is used here in the restricted sense of an odd-electron-count insulators, possibly undergoing (e.g.) magnetic disorder transitions, and to describe which one must describe reasonably electron interactions across energy scales from direct interaction, of order 1-10 eV, to exchange (Hund, super, double) of order 0.1-1 eV, and structural distortions, of order 0.01-0.1 eV. Within first-principles approaches, only many-body perturbation-theory, hybrid–density-functional, and self-interaction-corrected density-functional methods seem able to reach this level of accuracy (of course, dynamical mean field theory does also, although it generally uses empirical inputs in the self-energy and, especially, about structure); all of these methods remove self interaction from local density functionals–hence our interest in them in the present context.

[134] D. M. Ceperley and B. J. Alder, Phys. Rev. Lett. **45**, 566 (1980)

[135] J. P. Perdew, K. Burke, and M Ernzerhof, Phys. Rev. Lett. **77**, 3865 (1996).

[136] S. L. Dudarev, G. A. Botton, S. Y. Savrasov, C. J. Humphreys, and A. P. Sutton, Phys. Rev. B **57**, 1505 (1998).

[137] J. Heyd, G. E. Scuseria, and M. Ernzerhof, J. Chem. Phys. **118**, 8207 (2003).

[138] G. Kresse and J. Furthmüller, Comput. Mater. Sci. **6**, 15 (1996); Phys. Rev. B **54**, 11169 (1996).

[139] P.E. Blöchl, Phys. Rev. B **50**, 17953 (1994); G. Kresse and D. Joubert, Phys. Rev. B **59**, 1758 (1999). The datasets employed are listed as [name, valence electrons, (partial core radius, outer core radius, core radius for projectors, core radius of augmentation charge), ℓ of local potential, valence configuration]: [Cu, 11, (2.0, 2.3, 2.34, 1.77), 3, $d^{10}s^1$], [O, 6, (1.2, 1.52, 1.55, 1.33), 2, s^2p^4], [Ti, 10, (2.2, 2.5, 2.56, 1.95), 1, $p^6s^2d^2$], [Ca, 10, (2.0, 2.3, 2.36, 1.99), 1, $s^2p^6s^2$].

[140] M. Shishkin and G. Kresse, Phys. Rev. B **74**, 035101 (2006); *ibid.***75**, 235102 (2007).

[141] G. Grosso and G. Pastori Parravicini, *Solid state physics* (Academic Press, London 2000).

[142] I. D. Hughes, M. Däne, A. Ernst, W. Hergert, M. Lüders, J. B. Staunton, Z. Szotek, and W. M. Temmerman, New J. Phys. **10** 063010 (2008) have reported gap conservation in paramagnetic MnO using disordered-local-moments self-interaction-corrected density functional theory.

[143] M. D. Johannes, W. E. Pickett, and R. Weht, Mat. Res. Soc. Symp. Proc. **718**, 25 (2002).

[144] V. I. Anisimov, F. Aryasetiawan, and A. I. Lichtenstein, J. Phys.: Condens. Matter **9** 767 (1997).

[145] M. Cococcioni and S. de Gironcoli, Phys. Rev. B **71**, 035105 (2005).

[146] H. Hsu, K. Umemoto, M. Cococcioni, and R. M. Wentzcovitch, Phys. Rev. B **79**, 125124 (2009).

[147] A. Alkauskas and A. Pasquarello, Physica B **401-402**, 546 (2007).

[148] F. Gygi and A. Baldereschi, Phys. Rev. Lett. **62**, 2160 (1989)

[149] V. Fiorentini and A. Baldereschi, Phys. Rev. B **51**, 17196 (1995).

[150] X. Rocquefelte, M.-H. Whangbo, A. Villesuzanne, S. Jobic, F. Tran, K. Schwarz, and P. Blaha, J. Phys.: Condens. Matter **22**, 045502 (2010).

[151] C. D. Pemmaraju, T. Archer, D. Sánchez-Portal, and S. Sanvito, Phys. Rev. B **75**, 045101 (2007)

[152] T. Archer, C. D. Pemmaraju, S. Sanvito, C. Franchini, J. He, A. Filippetti, P. Delugas, D. Puggioni, V. Fiorentini, R. Tiwari and P. Majumdar, Phys. Rev. B **84**, 115114 (2011).

[153] A. Filippetti and V. Fiorentini, Phys. Rev. Lett. **95**, 086405 (2005).

[154] G. Peralta, D. Puggioni, A. Filippetti, and V. Fiorentini, Phys. Rev. B **80**, 140408(R) (2009); X.-Q. Chen, C. L. Fu, C. Franchini, and R. Podloucky, Phys. Rev. B **80**, 094527 (2009)

[155] D. Puggioni, A. Filippetti, and V. Fiorentini, Phys. Rev. B **86**, 195132 (2012).

[156] P. Alippi and V. Fiorentini, Eur. Phys. J. B **85**, 82 (2012).

[157] A. Filippetti and V. Fiorentini, Phys. Rev. Lett. **98**, 196403 (2007).

[158] A. Filippetti and V. Fiorentini, Phys. Rev. B **77**, 235124 (2008).

[159] Alippi P, Cesaria M, and Fiorentini V 2014 *Phys. Rev. B* **89** 134423.

[160] Tippins H H 1965 *Phys. Rev. B* **140** 316

[161] He H et al 2006 *Phys. Rev. B* **74** 195123.

[162] F. Zhang, K. Saito, T. Tanaka, M. Nishio, and Q. Guo, Solid State Comm. **186**, 28 (2014).

[163] M. Baldini, D. Gogova, K. Irmscher, M. Schmidbauer, G. Wagner, and R. Fornari, Cryst. Res. Technol. **49**, 552 (2014)

[164] D. F. Edwards, *Handbook of Optical Constants of Solids* (Academic Press, New York 1998), p. 753, vol. III.

[165] G. Kresse and J. Furthmuller Phys. Rev. B **54**, 11169 (1996).

[166] S. Geller, J. Chem. Phys. **33**, 676 (1960).

[167] M. B. Maccioni, F. Ricci, and V. Fiorentini, J. Phys.: Conf. Ser. 566, 012016 (2014).

[168] D. B. Laks, C. G. Van de Walle, G. F. Neumark, P. E. Blöchl, and S. T. Pantelides, Phys. Rev. B **45**, 10965 (1992).

[169] The formation energy of a diluted defect is calculated at the equilibrium volume of the perfect crystal. See M. Finnis, *Interatomic Forces in Condensed Matter* (Oxford UP, Oxford, 2004), pp. 156-157.

[170] See e.g. M. Peressi, N. Binggeli, and A. Baldereschi, J. Phys. D: Appl. Phys. **31**, 1273 (1998). For cases with interface monopoles (absent in the present superlattice orientation) see F. Bernardini and V. Fiorentini, Phys. Rev. B **57**, R9427 (1998).

[171] V. Fiorentini, Phys. Rev. B **46**, 2086 (1992).

[172] F. Ricci, F. Boschi, A. Baraldi, M. Higashiwaki, A. Kuramata, A. Filippetti, V. Fiorentini, and R. Fornari, to be published.

[173] V. Fiorentini and A. Baldereschi, J. Phys.: Condens. Matter **4**, 5967 (1992); Phys. Rev. B **51**, 17196 (1995).

[174] J. A. Kohn, G. Katz, J. D. Broder, Am. Mineral. 42, 398 (1957).

[175] S. Geller, J. Chem. Phys. 33, 676 (1960).

[176] M. R. Lorenz, J.F. Woods, R. J. Gambino, J. Phys. Chem. Solids 28, 403 (1967).

[177] Y. Tomm, P. Reiche, D. Klimm, T. Fukuda, J. Cryst. Growth 220, 510 (2000).

[178] H. Aida, K. Nishigu, H.Takeda, N. Aota, K. Sunakawa, Y. Yaguchi, Jpn. J. Appl. Phys. 47, 8506 (2008).

[179] Z. Galazka, R. Uecker, K. Irmscher, M. Albrecht, D. Klimm, M. Pietsch, M. Brützam, R. Bertram, S. Ganschow, R. Fornari, Cryst. Res. Technol. 45, 1229 (2010).

[180] T. Oshima, N. Arai, N. Suzuki, S. Ohira, S. Fujita, Thin Sol. Films 516, 5768 (2008).

[181] M. Tsai, O. Bierwagen, M. White, J. S. Speck, J. Vac. Sci. Technol. 28, 354 (2010).

[182] G. Wagner, M. Baldini, D. Gogova, M. Schmidbauer, R. Schewski, M. Albrecht, Z. Galazka, D. Klimm, R. Fornari, Phys. Stat. Sol. A 211, 27 (2014).

[183] S. Ohira, N. Suzuki, H. Minami, K. Takahashi, T. Araki, Y. Nanishi, Phys. Stat. Sol. C 4, 2306 (2007).

[184] K. Kachel, M. Korytov, D. Gogova, Z. Galazka, M. Albrecht, R. Zwierz, D. Siche, S. Golka, A. Kwasniewski, M. Schmidbauer, R. Fornari, Cryst. Eng. Commun. 14, 8536 (2012).

[185] K. Sasaki, M. Higashiwaki, A. Kuramata, T. Masui, S. Yamakoshi, J. Cryst. Growth 378, 591 (2013).

[186] M. Higashiwaki, K. Sasaki, A. Kuramata, T. Masui, S Yamakoshi, Phys. Stat. Sol. A 211, 21 (2014).

[187] J. Åhman, G. Svensson, J. Albertsson, Acta Crystallogr. C 52, 1336 (1996).

[188] K. Yamaguchi, Solid State Commun. 131, 739 (2004).

[189] M. Mohamed, C. Janowitz, I. Unger, R. Manzke, Z. Galazka, R. Uecker, R. Fornari, J. R. Weber, J. B. Varley and C. G. Van de Walle, Appl. Phys. Lett. 97, 211903 (2010).

[190] C. Janowitz, V. Scherer, M. Mohamed, A. Krapf, H. Dwelk, R. Manzke, Z. Galazka, R. Uecker, K. Irmscher, R. Fornari, M. Michling, D. Schmeißer, J. R. Weber, J.B. Varley, C.G. Van De Walle, New J. Phys. 13, 085014 (2011).chi, H.Takeda, N. Aota, K. Sunakawa, Y. Yaguchi, Jpn. J. Appl. Phys. 47, 8506 (2008).

[191] H. He, R. Orlando, M. A. Blanco, R. Pandey, E. Amzallag, I. Baraille, M. Rérat, Phys. Rev. B 74, 195123 (2006).

[192] T. Raja, V. Razdan, B. Arnold, D. Thomson, N. Prasad, R. Rai, N. Singh, in Proc. Materials Science and Technology Conference 2013, Montreal, Quebec, Canada, 27-31 October 2013, Curran Associates, Inc.(New York, 2014), Vol. 4, pp. 2782-2787.

[193] J. Zhang B. Li, C. Xia, G. Pei, Q. Deng, Z. Yang, W. Xu, H. Shi, F. Wu, Y. Wu, J. Xu, J. Phys. Chem. Solids 67, 2448 (2006).

[194] T. Matsumoto, M. Aoki, A. Kinoshita, T. Aono, Jpn. J. Appl. Phys. 13, 1578 (1974).

[195] N. Ueda, H. Hosono, R. Waseda, H. Kawazoe, Appl. Phys. Lett. 70, 3561 (1997).

[196] J. Heyd, G. E. Scuseria, M. Ernzerhof, J. Chem. Phys. 118, 8207 (2003).

[197] M. Shishkin and G. Kresse, Phys. Rev. B 74, 035101 (2006).

[198] G. Kresse and D. Joubert, Phys. Rev. B 59, 1758 (1999).

[199] F. Ricci, P. Alippi, A. Filippetti, V. Fiorentini, Phys. Rev. 90, 045132 (2014).

[200] The VPSIC code uses plane-waves and ultrasoft potentials with cutoff 408 eV; standard PAW from VASP are used; the k-point grids are 4x4x4 for self-consistency and 5x15x7 for dielectric function calculations; the number of bands in the joint-density of states is 300, and in the GW calculations it is 520. In GW0, the Green's function is iterated four times to obtain self-consistency.

[201] F. Zhang, K. Saito, T. Tanaka, M. Nishio, Q. Guo, Solid State Commun. 186, 28 (2014).

[202] G. F. Bassani and G. B. Pastori Parravicini, Electronic states and optical transitions in solids (Pergamon Press, New York, 1975).

[203] P. W. Anderson and E. I. Blount, Phys. Rev. Lett. **14**, 217 (1965).

[204] A. F. Santander-Syro *et al.*, Nature 469, **189** (2011); W. Meevasana *et al.*, Nature Mater. **10**, 114 (2011); H. W. Jang *et al.*, Nature **331**, 886 (2011); G. Herranz *et al.*, Sci. Rep. **2**, 758 (2012).

[205] D. Puggioni and J. M. Rondinelli, Nature Comm. **5**, 3432 (2013).

[206] F. Lichtenberg, D. Widmer, J.G. Bednorz, T. Williams, and A. Relier, Z. Phys. B **82**, 211 (1991); F. Lichtenberg, T. Williams, A. Relier, D. Widmer, and J. G. Bednorz, Z. Phys. B **84**, 369 (1991); T. Williams, H. Schmalle and A. Reller, J. Sol. St. Chem. **93**, 534 (1991);

[207] F. Lichtenberg, A. Herrnberger, K. Wiedenmann, J. Mannhart, Prog. Solid State Chem. **29**, 1 (2001); F. Lichtenberg, A. Herrnberger, and K. Wiedenmann, Prog. Solid State Chem. **36**, 253 (2008).

[208] J. López-Pérez and J. Íñiguez, Phys. Rev. B **84**, 075121 (2011); M. Scarrozza *et al.*, Phys. Rev. Lett. **109**, 217202 (2012); Eur. Phys. J. B **86**, 128 (2013).

[209] T. Williams, H. Schmalle, A. Reller, F. Lichtenberg, D. Widmer, and G. Bednorz, J. Sol. St. Chem. **93**, 534 (1991).

[210] G. Kresse and J. Hafner, Phys. Rev. B 47, 558 (1993); G. Kresse and J. Furthmüller, Comput. Mater. Sci. **6**, 15 (1996); Phys. Rev. B **54**, 11169 (1996); J. P. Perdew, K. Burke, and M. Ernzerhof, Phys. Rev. Lett. **77**, 3865 (1996).

[211] P. Delugas *et al.*, Phys. Rev. Lett **106**, 166807 (2011); A. Filippetti *et al.*, Phys. Rev. B **86**, 195301 (2012); C. Cancellieri *et al.*, Phys. Rev. B **89**, 121412(R) (2014); P. Delugas *et al.*, Phys. Rev. B **88**, 045310 (2013); P.

Delugas *et al.*, Phys. Rev. B **88**, 115304 (2013); D. Puggioni *et al.*, Phys. Rev. B **86**, 195132 (2012).

[212] D. Vanderbilt, Phys. Rev. B **41**, 7892 (1990). Ultrasoft potentials are known [213] to be a limiting case of the projector augmented waves.

[213] P. E. Blöchl, Phys. Rev. B **50**, 17953 (1994); G. Kresse, and D. Joubert, Phys. Rev. B **59**, 1758 (1999). We treat as valence the states Ti $3s$, $3p$, $3d$, $4s$; La $5s$, $5p$, $5d$, $6s$; Bi $5d$, $6s$, $6p$; O $2s$, $2p$.

[214] P. B. Allen, in *Quantum Theory of Real Materials*, J.R. Chelikowsky and S.G. Louie eds. (Kluwer, Boston 1996), pp. 219; G. Madsen and D. Singh, Comput. Phys. Comm. **175**, 67 (2006).

[215] R. D. King-Smith and D. Vanderbilt, Phys. Rev. B **47**, 1651 (1993); D. Vanderbilt and R.D. King-Smith, Phys. Rev. B **48** 4442 (1993); R. Resta, Rev. Mod. Phys. **66** 899 (1994).

[216] J. B. Neaton, C. Ederer, U. V. Waghmare, N. A. Spaldin, and K. M. Rabe, Phys. Rev. B **71**, 014113 (2005); J. C. Wojdel and J. Iniguez, Phys. Rev. Lett. **103**, 267205 (2009); M. Goffinet, P. Hermet, D. I. Bilc, and Ph. Ghosez, Phys. Rev. B **79**, 014403 (2009).

[217] These atoms always return to anti-ferroelectrically compensated positions despite all attempts to produce a coherent movement leading to polarized distortions.

[218] $P_{\rm cond}$ is the difference in Berry phase at the end-points of the 'λ-path" between CS $Immm$ and non-CS $Pm2_1n$ modulo a quantum $\Delta\mathbf{P}$=$2e\mathbf{R}$/V. Along that path the number of occupied bands at a given $k_\perp$ need not necessarily be constant; discontinuities of $\phi^{(\lambda)}(k_\perp)$ vs λ could conceivably occur, and remain to be investigated. However, *a posteriori* such occurrence is unlikely, especially given the large $\Delta\mathbf{P}$.

[219] F. Bernardini and V. Fiorentini, Phys. Rev. B **58**, 15292 (1998).